AN INVESTIGATION OF THE UNDERWATER ACOUSTIC COMMUNICATIONS CHANNEL

by

Ian Roman Radziejewski

B.A.Sc., Simon Fraser University, 1988

A THESIS SUBMITTED IN PARTIAL FULFILLMENT OF THE REQUIREMENTS

FOR THE DEGREE OF

MASTER OF APPLIED SCIENCE (ENGINEERING SCIENCE)

in the School

of

Engineering Science

© Ian Roman Radziejewski 1990
Simon Fraser University
August 1990

APPROVAL

NAME: Ian Roman Radziejewski

DEGREE: Master of Applied Science (Engineering Science)

TITLE OF THESIS: An Investigation of the Underwater Acoustic Com-
                               munications Channel

EXAMINING COMMITTEE:

_____

Dr. John S. Bird
Senior Supervisor

_____

Dr. Vladimir Cuperman

_____

Dr. Shawn Stapleton

_____

Dr. Peter Fox
Simrad Mesotech Ltd
External Examiner

DATE APPROVED: _22 August 1990_____

PARTIAL COPYRIGHT LICENSE

I hereby grant to Simon Fraser University the right to lend my thesis, project or extended essay (the title of which is shown below) to users of the Simon Fraser University Library, and to make partial or single copies only for such users or in response to a request from the library of any other university, or other educational institution, on its own behalf or for one of its users. I further agree that permission for multiple copying of this work for scholarly purposes may be granted by me or the Dean of Graduate Studies. It is understood that copying or publication of this work for financial gain shall not be allowed without my written permission.

Title of Thesis/Project/Extended Essay

"An Investigation Of The Underwater Acoustic Communications Channel"

_____

_____

_____

Author:_____

  (signature)

  Ian Roman Radziejewski

  (name)

  August 23, 1990

  (date)

ABSTRACT

This thesis presents results of research on the characteristics of the undersea communications channel. A computer based model of the underwater channel was developed and used to study channel behaviour under varying conditions. The model demonstrates the variability of the multipath energy and shows that it is highly dependent upon the channel geometry. It is also shown that coherent diversity combination with a receiver array can significantly reduce multipath interference.

A custom designed undersea testbed was used to collect data on the transmission characteristics of both the acoustic channel and the underwater transducers. The testbed synchronously samples the received signals and recovers the complex baseband information. The effects of channel impairments on communications systems are considered. Initial findings indicate that the transducer mountings and projector characteristics play an important role in determining the channel performance.

For mum

ACKNOWLEDGEMENTS

Table of Contents

List of Tables

List of Figures

1 Introduction

1.1 Background and Motivation for Research

It has long been recognized that the acoustic channel is the only feasible means of underwater communications over any appreciable distance [1]. The severe attenuation of electromagnetic energy propagating through water forces us to use acoustic methods. Yet the acoustic channel has proven to be difficult to work with [2].

There are many problems inherent to underwater acoustic communications. The attenuation of sound in water increases rapidly with the signal's frequency thereby limiting either the range or the bandwidth of the channel. The underwater environment is also very reverberant, resulting in considerable multipath interference. There are numerous published papers dealing with these topics. Many of them analyze one or more aspects of the problem and then propose specific solutions [3]. Some go as far as building actual communications systems and measuring their performance; see for example references [4] or [5]. Frequently

the performance fails to meet the original expectations, or is quite unpredictable.

In all cases the underwater communication systems could be classified as low to moderate data rate systems. The throughputs commonly range anywhere from less than one bit per second [6] up to 1200 bps [7]. Higher rates are sometimes achieved by operating in close to ideal conditions such as very deep water where multipath propagation is greatly reduced.

One exception is a system recently developed by Woods Hole Oceanographic Institute [8]. They were able to achieve a 10 kbps data rate (uncoded) over a range of 750 m in a shallow harbour. However, the system requires an tremendous amount of computing power for signal processing and channel equalization. In fact, the receiver uses a network of transputers to achieve the necessary computation speed.

Yet some theoretical studies predict data rates several orders of magnitude higher. For example, Hardy and Collins [9] calculated that the short range (600 m) channel they studied had a channel capacity of over 700 kbps and that a data rate of greater than 100 kbps should be realistically achievable.

Ideally one would like to attain such a high data rate. However, more modest improvements would still be valuable. For example, Shevenell [10] describes a method for transmitting video images over a 9600 bps link. Clearly the ability to transmit realtime video images over an acoustic link would be a boon to the undersea industry. The most obvious application is guidance and image retrieval for an autonomous vehicle.

This thesis describes the results of our initial probing of the underwater channel to identify potential problem areas. Instead of focusing on one particular problem, the aim of the research is to gain some insight into the fundamental nature of the channel. The intention of this back-to-basics-approach is to be able to characterize and predict the channel's effect upon a transmitted signal.

2

1.2 Research Methodology

The first component of the research was the development of a computer model of the underwater channel. The model was developed as a tool to study the channel response under different conditions and to observe how the response changes as the conditions are varied. The model was implemented in Fortran, based upon an image model of acoustic propagation underwater. The program calculates the channel impulse response, given a set of parameters which characterize the channel.

The second component was an experimental characterization of the channel using an underwater testbed. Rather than implementing a complete communications system, the idea is to be able to generate and receive coherent signals and analyze the resulting effects of the channel. In the context of this research, the channel includes not only the transmission medium, but also the acoustic transducers and associated circuitry.

The initial research work described here used a carrier frequency of 24 kHz. There are some advantages to working at this relatively low frequency. First, the attenuation coefficient is only 3 dB per km [11] - low enough to allow communication with an autonomous underwater vehicle (AUV) over a considerable range. This frequency band is therefore important for the long range telemetry of control and status information. For example, the 10 kbps system developed at Woods Hole uses the 15-35 kHz band.

A second advantage is that a lower carrier frequency and smaller signal bandwidth permits a lower sampling rate, thus simplifying the receive and transmit electronics. The main disadvantage is that the lower available bandwidth reduces the maximum data rate that can be achieved over a given channel.

1.3 Outline of Thesis

This thesis is divided into seven chapters. After this introduction, section 2 discusses the model of the underwater acoustic channel. The theoretical basis for the model and details of its implementation are presented first, followed by a description of the operation of the program. Results of the modelling are described and analyzed. The use of receiver arrays (spatial diversity) is then explored, and further model predictions are presented.

In section 3 an analysis of the acoustic transducers is given. Also discussed are the transmit and receive amplifiers and their noise properties.

Section 4 briefly describes the underwater testbed, including its architecture, system design and software. The acoustic and electronic noise levels are calculated to determine the expected signal to noise ratios. The process of bandpass sampling used for recovering the complex baseband signal is also covered.

Section 5 details the experimental work. After describing the test environments, examples of direct and multipath returns are presented. Plots of the corresponding complex baseband signals are then shown and compared with the time domain plots. Some anomalies revealed by the baseband data are then discussed.

The experimental data is analyzed in section 6. Various elements of the acoustic channel are considered in order to explain the observed behaviour. Additional experimental data is presented to support the analysis.

Chapter 7 discusses conclusions drawn from the research. Finally, directions for future work are suggested.

2 Modelling the Underwater Acoustic Channel

2.1 Acoustic Propagation in Water

The propagation of sound in water is governed by the well known wave equation [12], which can be expressed in Cartesian co-ordinates as

$$\frac{\partial^2 p}{\partial t^2} = c^2 \left(\frac{\partial^2 p}{\partial x^2} + \frac{\partial^2 p}{\partial y^2} + \frac{\partial^2 p}{\partial z^2} \right) \tag{2.1}$$

where p is pressure, and c is the velocity of sound in the medium. To exactly determine the sound intensity at any point it is necessary to solve 2.1 with the appropriate initial and boundary conditions. In practise, obtaining the solution is not usually straightforward. For example, the boundaries formed by the surface and bottom are not well defined planes, as

5

is often assumed in deriving solutions. Furthermore, the water is not a homogeneous medium; its properties are affected by factors such as solar heating and the presence of plant and animal life.

As with the study of optics, a viable alternative is the use of ray tracing methods. Though certainly less rigorous than wave acoustics, ray acoustics allows the determination of sound propagation patterns with relatively simple calculations.

As a starting point we assume that the sound radiates from a compact source as spherical pressure waves. Strictly speaking, the medium must be homogeneous in order to support spherical waves. There are ray tracing methods for dealing with sound speed variation, and they are discussed in section 6.2. However, we shall assume a homogeneous medium for the present time.

In a lossless medium the amplitude of the pressure waves decrease inversely with the distance from the source, so the sound intensity, or energy, obeys the inverse square law. However, water is not a lossless medium for sound; apart from the spherical spreading loss there is additional energy lost due to absorption by the water. This loss increases linearly with range, and is usually specified by the absorption coefficient α.

The magnitude of α depends upon the composition of the water; for example, sea water is more lossy than fresh water. In addition, α increases with the frequency of the sound, and is approximately proportional to the square of the frequency [13]. This loss severely limits the potential bandwidth or range of acoustic transmission.

The primary boundaries of the transmission medium are the surface and the bottom. Rays which are incident upon either boundary are reflected at an angle equal to the angle of incidence. Of course neither the surface nor the bottom are perfectly flat or horizontal.

The surface is disturbed constantly by waves, or by floating objects such as ships. There is also some acoustic energy lost through reflection because part of the sound passes through the boundary. It is useful to combine these effects and assume that the acoustic ray loses a constant amount of energy after every surface reflection. This constant is simply

6

called the surface reflection loss and is usually expressed in dB. One expression [14] estimates the surface loss α_s as a function of the wave height H (in metres) and the frequency f (in kHz)

$$\alpha_s = 10\log[1 - 0.139(fH)^{3/2}] \qquad (2.2)$$

However, this equation is only useful for small grazing angles and loss values less than about 3 dB. Other expressions for different surface conditions are given in [15]. An important property of the surface is that it is a pressure release boundary; a sound ray reflected from the surface will undergo a phase shift of 180°.

Although the bottom is not subject to disturbances such as wave motion, its reflection coefficient is not easily predicted. The composition of the bottom material varies widely at different locations. A smooth rock bottom may have a reflection loss close to 0 dB, while soft mud may reduce the reflected signal by 20 dB or more. Unlike the surface, the bottom will not invert the phase of a reflected signal.

The study of acoustic propagation involves many more issues than have been mentioned here; for a more detailed discussion refer to Urick [16] or Bergmann [17]. Nevertheless, a simple propagation model such as described above can be very useful in studying the behaviour of the acoustic channel.

2.2 Model Development

The first component of the research for this thesis was the development of a model to study the propagation characteristics of the underwater channel. This section gives a brief description of some of the features of the computer program, followed by the mathematical details of the model implementation.

The computer model was implemented on a Sun workstation and is comprised of over 4000 lines of Fortran code. The program is completely menu driven; model results are displayed in graphical form and can be sent to the workstation's graphics screen or to a printer. Figure 2-1 shows the main menu from the model.

```
URL's Underwater Model
======================

Today's menu:
   1] Change model parameters
   2] Plot channel impulse response
   3] Plot 2D response as a function of 1 parameter
   4] Plot 3D response as a function of 2 parameters
   5] Define receiver array
   6] Plot received waveform
   7] Save state of model
   8] Load model
   9] Quit

Enter your selection (1-9) :
```

Figure 2-1 - Main Menu for the Underwater Model

2.2.1 Model Parameters

The first option allows the user to set up the model parameters. The values can be entered from the keyboard or retrieved from a previously saved parameter file; figure 2-2 shows the parameter list. Most of the parameters were discussed in section 2.1. The significance of the symbol rate is explained in section 2.2.3.

8

The only option requiring explanation is "Max. number images". This setting determines how many source images the model will use. Twenty images are more than adequate to determine all the significant multipath signals. The signal amplitude becomes negligible after a only a few reflections because of the spherical spreading ($1/r^2$), absorption loss α, and the boundary reflection losses. Reducing the number of images has the advantage of decreasing the required computation time.

```
Model parameters
=================

Water depth              (  m      )  :   0.
Propagation speed        (  m/s    )  :   0.
Transmitter depth        (  m      )  :   0.
Receiver depth           (  m      )  :   0.
Horizontal distance      (  m      )  :   0.
Surface reflection loss  (  dB     )  :   0.
Bottom reflection loss   (  dB     )  :   0.
Absorption loss          (  dB/km  )  :   0.
Carrier frequency        (  Hz     )  :   0.
Symbol rate              (  Hz     )  :   0.
Max. number images       (         )  :   0.
```

Figure 2-2 - Parameter List for the Underwater Model

2.2.2 Calculating the Multipath Structure

The paths of reflected rays can be calculated with the aid of an image model, as illustrated in figure 2-3. Starting with water of a given depth, the bottom and surface boundary images are placed alternately above and below the "real" boundaries. Next the source is

placed at a given depth and its mirror images are placed between the image boundaries, exactly as with an optical mirror image. The first four source images are labelled A, B, C and D in figure 2-3.
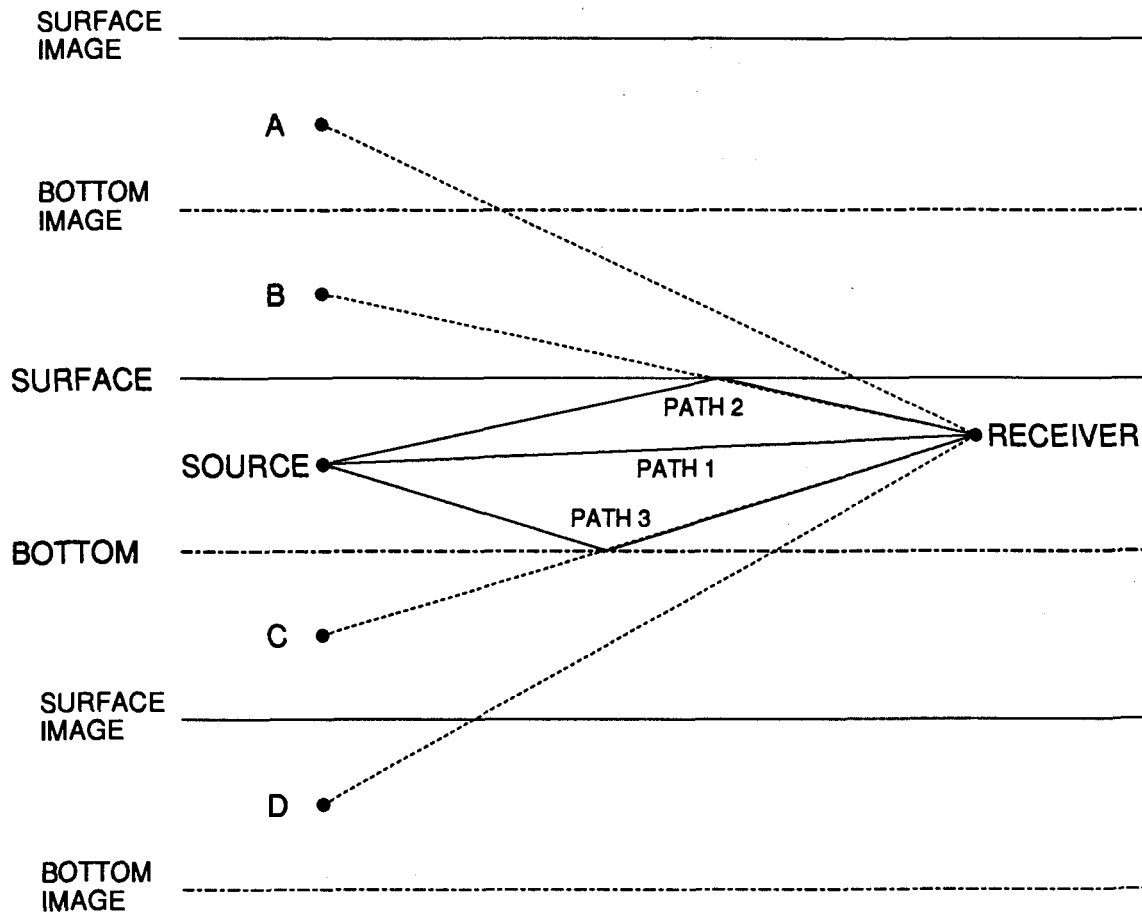
Figure 2-3 - Sound Ray Image Model

The length of a reflected ray path is the distance from the source image to the receiver. For example, the path from B to the receiver corresponds the first surface bounce labelled as PATH 2. The path from C represents the first bottom bounce, labelled as PATH 3, and so on.

10

2.2.3 Calculating the Channel Impulse Response

The first type of data generated by the model is a plot of the channel's complex impulse response. The plot is not exactly the channel impulse response, but rather the demodulated output resulting from a single gated carrier pulse. The pulse length is one period of the symbol frequency.

The first step in calculating the impulse response is determining the path lengths of all the direct and reflected signals, as described in the previous section. Next the propagation times t_p to the receiver are calculated with the simple equation

$$t_p = \frac{l}{c} \tag{2.3}$$

where l is the path length in m and c is the sound speed in m/s. The signal attenuation in dB is then determined by the following equation

$$loss = 20\log l + n_s\alpha_s + n_b\alpha_b + l\alpha \tag{2.4}$$

where n_s and n_b are the number of surface and bottom bounces, α_s and α_b are the surface and bottom reflection losses in dB, and α is the absorption loss in dB/m. The magnitude of the attenuation A is then just

$$A = 10^{-\frac{loss}{20}} * (-1)^{n_s} \tag{2.5}$$

The sign of the signal is inverted when there is an odd number of surface reflections. After finding the magnitude and propagation delay for each signal, the complex components of the baseband signal are determined. All of the propagation delays are normalized so that the first signal arrives at time zero. The new delay time d is then just

$$d \ = \ t_p - t_0 \tag{2.6}$$

where t_0 is the propagation delay of the first signal to arrive at the receiver. The phase angle ϕ of a received signal is then calculated as

$$\phi \ = \ 2\pi f_c d \tag{2.7}$$

where f_c is the carrier frequency. In the model, the demodulation involves not only the frequency down conversion but also an integrate and dump process. Specifically, the I and Q channel signals are passed through an integrator which is reset to zero after every symbol period. In general, except for the first arrival, a signal will not arrive exactly at the start of a symbol period. The signal energy is therefore split into two consecutive symbol periods.

The next step in calculating the baseband signal is determining which symbol period the signal is received in. The equation for the symbol number S is

$$S \ = \ 1 + \left\lfloor \frac{d}{T} \right\rfloor \tag{2.8}$$

where T is the length of the symbol period. The first signal will arrive in symbol period 1. The program must next calculate the delay between the start of the symbol period and the time the signal arrives. This delay d_T is simply d modulo T, which is

$$d_T = d - (S-1)*T \tag{2.9}$$

The I and Q components of the baseband signal can then be calculated by the following equations

$$rI_1 = A\frac{(T-d_T)}{T}\cos\phi \tag{2.10}$$

$$rQ_1 = -A\frac{(T-d_T)}{T}\sin\phi \tag{2.11}$$

$$rI_2 = A\frac{d_T}{T}\cos\phi \tag{2.12}$$

$$rQ_2 = -A\frac{d_T}{T}\sin\phi \tag{2.13}$$

where rI_1 and rQ_1 are the Inphase and Quadrature components of the signal received during symbol period S. Similarly, rI_2 and rQ_2 are the Inphase and Quadrature components of the signal received during symbol period S+1.

The I and Q components are calculated for the direct and reflected signals and the results are placed in an array of complex numbers, indexed by the symbol number S. When two or more signals are present in one symbol period the I components are added together and the Q components are added together. Thus signals may add constructively or destructively, depending upon their relative phase.

2.2.4 Calculating A Measure of the Channel Response

The next feature of the model is the ability to plot the channel response as a function of one or two of the parameters. In order to generate the plot, it is necessary to devise a scalar measure of the channel response. One measure used in the model is the ratio of the energy in the direct signal to the total energy in all the multipath returns.

The program first calculates the energy in the direct arrival, assuming no reflections. Then the energy in the reflected signals is calculated, assuming no interference with the direct arrival. The energy E is calculated as the sum of the squares of the inphase and quadrature signal components

$$E \quad = \quad rI^2 + rQ^2 \tag{2.14}$$

This measure describes the amount of reverberant energy in the channel as a result of one transmitted symbol. This reverberant energy competes with the direct signals in the form of multipath arrivals. The amount of reverberant energy will vary as the channel parameters change and as the multipath arrivals interfere constructively and destructively with each other.

Note that this measure does not account for interference of the direct signal arrival with its own reverberation. This process would alter the results when the transducers are close enough to boundaries for the reflected signals to be received during the direct arrival. This occurs when the difference in path length between the direct and reflected signal is less than one symbol period. However, the model can also calculate a second measure: the ratio of energy in the first received symbol to the sum of the energy in all subsequent symbol periods. The energy in the first symbol includes the effects of any interference between the direct and multipath arrivals.

14

2.2.5 Modelling a Receiver Array

Another feature of the program is the ability to model the effect of using an array of receive elements. The user can define an arbitrary set of elements at any position relative to an origin at the receiver location. Each element can also have a gain factor in order to shade the array response for different beam patterns. Finally, a steering angle θ can be defined so that the signals arriving at the various elements are delayed and phase compensated to add coherently when a signal arrives at the steering angle. The geometry of an array with 3 hydrophones, labelled A to C, is diagramed below in figure 2-4.
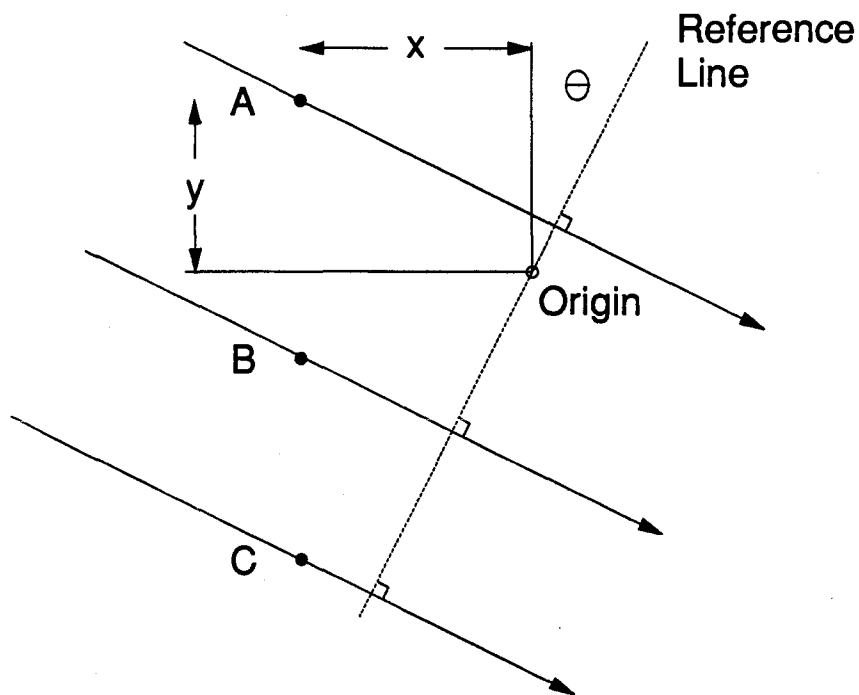
Figure 2-4 - Geometry of the Receiver Array

The program calculates the channel response from an array simply by adding the individual responses of each receiver element, or hydrophone. The only complication is the need to time delay and phase shift the received signals. Each signal must be delayed or

advanced in time to a reference line passing through the origin at the steering angle θ, as shown in figure 2-4. For example, take hydrophone A from figure 2-4. The signal must first be delayed in time by τ

$$\tau \quad = \quad \frac{\sqrt{x^2 + y^2} \sin\left(\theta + arctan\frac{x}{y}\right)}{c} \tag{2.15}$$

where x and y are the coordinate locations of the hydrophone and c is the sound speed. Next the received signals must be phase shifted

$$rI \quad = \quad rI \cos(2\pi f_c \tau) - rQ \sin(2\pi f_c \tau) \tag{2.16}$$

$$rQ \quad = \quad rI \sin(2\pi f_c \tau) + rQ \cos(2\pi f_c \tau) \tag{2.17}$$

Finally the signals from all the hydrophones are summed to produce the output.

2.3 Model Results

2.3.1 Acoustic Channel Impulse Response

Figure 2-5 is an example of the modelled acoustic channel impulse response. It is plotted as a three dimensional graph, with the inphase and quadrature components as the x and y axes and time as the vertical z axis. Each time unit on the vertical axis represents one symbol period.
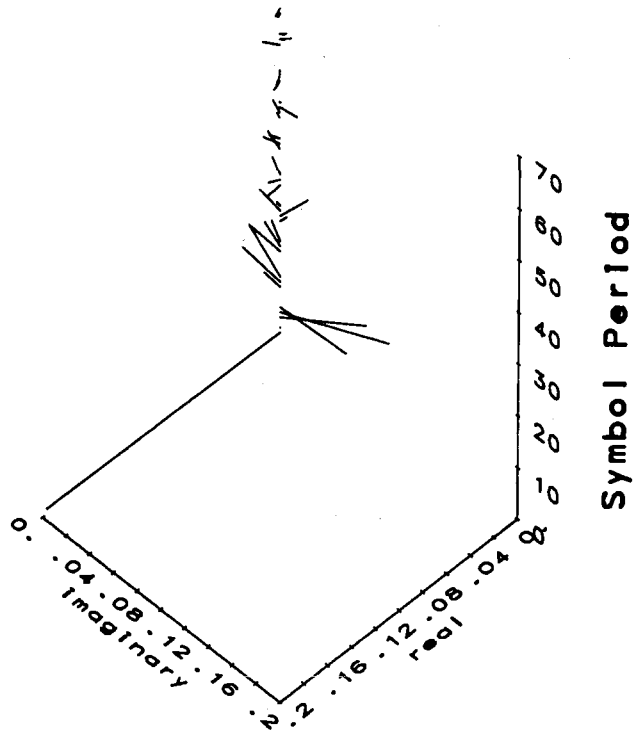
16

Parameter	Value	Parameter	Value
Water depth	10 m	Propagation speed	1500 m/s
Transmitter depth	5 m	Receiver depth	4 m
Horizontal distance	5 m	Surface reflection loss	0 dB
Bottom reflection loss	0 dB	Absorption loss	0 dB/km
Carrier frequency	24000 Hz	Symbol rate	1000 Hz

Figure 2-5 - Complex Response of Underwater Channel

17

In figure 2-5 the direct arrival is purely real, meaning that no multipath signal arrived within the first symbol period. The transmitter and receiver are relatively far from the boundaries, so the path lengths of the reflected signals are significantly longer than the direct arrival.

The first reflected signals arrive a few symbol periods after the direct signal. They have varying phase angles because they arrived at different points within a symbol period. When they do not arrive exactly at the start of a symbol period then the signal appears in two consecutive symbol times. The magnitudes of the multipath arrivals tend to decrease with time because they suffer more loss due to spreading.

The next figure demonstrates the effect of raising the receiver to a depth of 0.5 m, while keeping all other parameters fixed. The baseband signal received in the first symbol period is no longer purely real. The path length of the surface reflection is now closer to the direct path length, so the direct arrival has mixed with the first surface bounce. Part of the first surface reflection is also present in the second symbol period. The entire structure of the response was altered because the distances and phase angles of all arrivals changed.

The first two response plots were somewhat unrealistic in that they assumed zero reflection losses at both the surface and the bottom. The absorption loss was also set to 0 dB/km, although its effect over short distances at 24 kHz is negligible. Figure 2-7 plots the response when the effects of reflection and absorption losses are included. The other parameters are the same as figure 2-5. The magnitudes of the multipath returns are all reduced dramatically because of the reflection losses.

2.3.2 Channel Response as a Function of One Parameter

Figure 2-8 is a plot of the direct/reflected energy as a function of horizontal distance between the transmitter and receiver. The y axis is scaled logarithmically in order to show better detail at the larger distances.
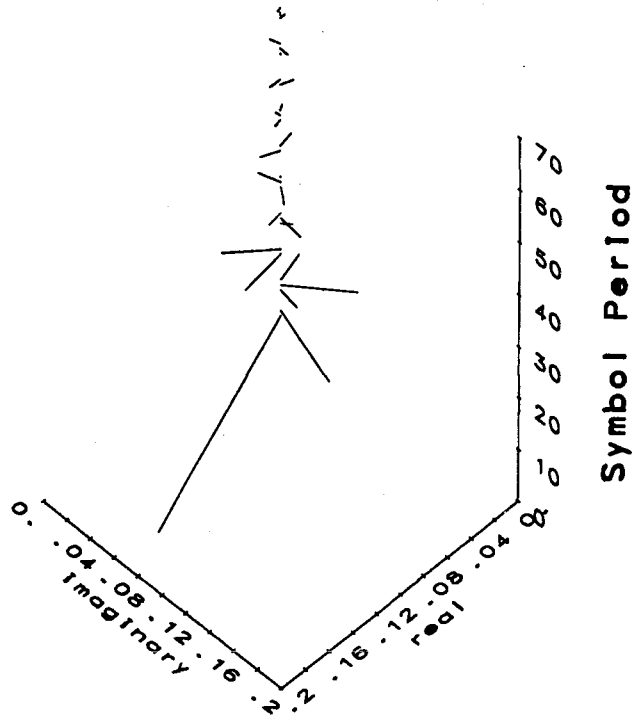
18

Parameter	Value	Parameter	Value
Water depth	10 m	Propagation speed	1500 m/s
Transmitter depth	5 m	Receiver depth	0.5 m
Horizontal distance	5 m	Surface reflection loss	0 dB
Bottom reflection loss	0 dB	Absorption loss	0 dB/km
Carrier frequency	24000 Hz	Symbol rate	1000 Hz

Figure 2-6 - Complex Response with Receiver Near the Surface
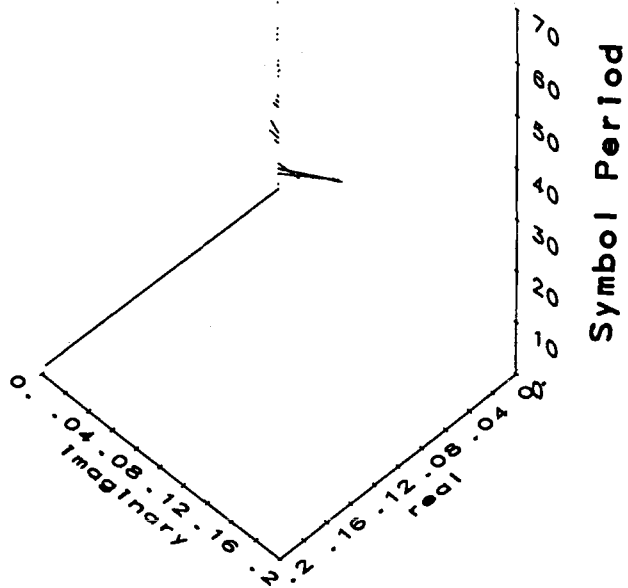
19

Parameter	Value	Parameter	Value
Water depth	10 m	Propagation speed	1500 m/s
Transmitter depth	5 m	Receiver depth	5 m
Horizontal distance	5 m	Surface reflection loss	3 dB
Bottom reflection loss	10 dB	Absorption loss	3 dB/km
Carrier frequency	24000 Hz	Symbol rate	1000 Hz

Figure 2-7 - Complex Response With Non-Zero Loss Coefficients
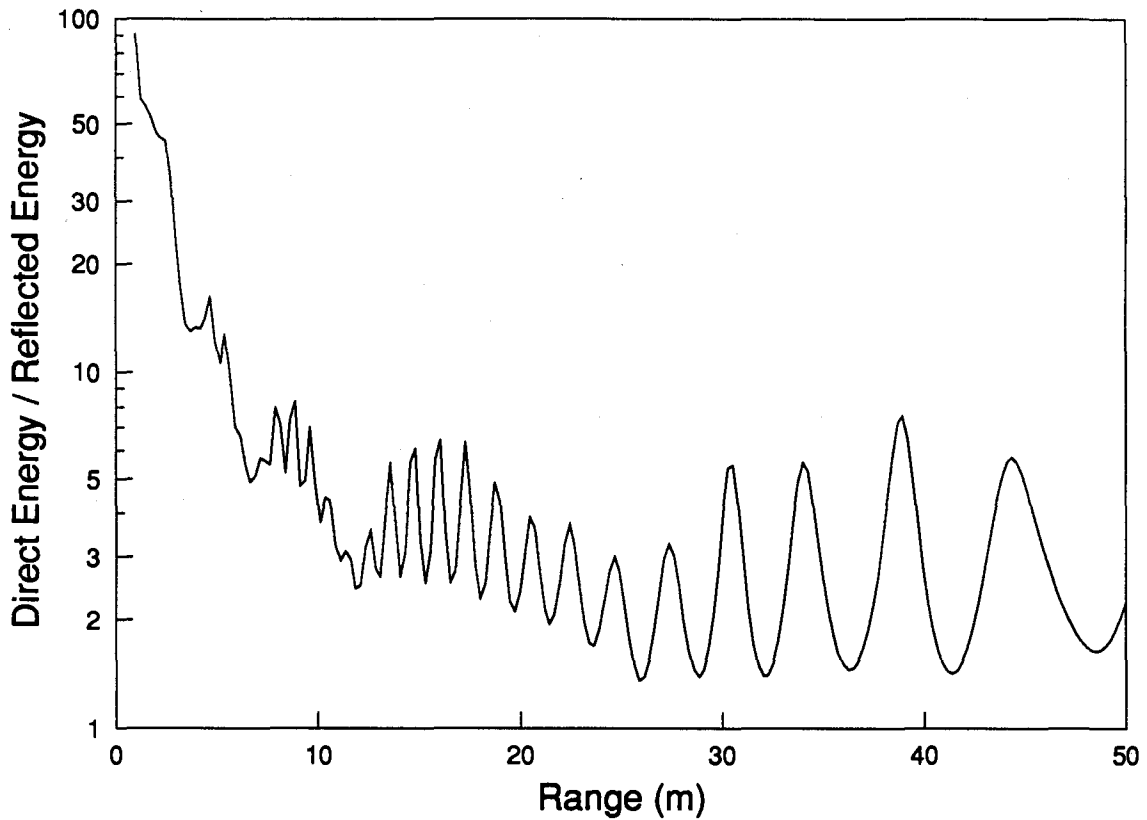
Parameter	Value	Parameter	Value
Water depth	10 m	Propagation speed	1500 m/s
Transmitter depth	5 m	Receiver depth	5 m
Horizontal distance	variable	Surface reflection loss	3 dB
Bottom reflection loss	10 dB	Absorption loss	3 dB/km
Carrier frequency	24000 Hz	Symbol rate	1000 Hz

Figure 2-8 - Direct/Reflected Energy versus Distance

The graph shows that the ratio of direct to reflected energy falls off very rapidly over the first few metres. The ratio is very high at short distances because the direct signal must travel only a short distance to the receiver, while the reflected signals must travel almost vertically to the surface or the bottom and then back again before reaching the receiver.

When the horizontal distance becomes comparable with the depth then the path lengths of the reflected signals are comparable to the direct distance. As the distance increases further the difference between the direct and reflected path lengths decreases asymptotically towards zero. In other words, the multipath signals suffer the same loss due to spreading as does the direct signal. However, the multipath signals still lose more energy because of reflection losses.

There is also loss because of interference between the multipath arrivals. The large variations in the direct/reflected energy at the greater distances are due to the changing interference structure. As the distance changes the phase angles of the signals arriving at the receiver also change. At certain distances some signals will add constructively and others interfere destructively. Since the acoustic wavelength at 24 kHz is 6.25 cm, only a small change in distance is required to significantly change the interference pattern. This effect is demonstrated more dramatically in figure 2-9, which plots the response as a function of receiver depth.

There is a large and rapid variation in the direct/reflected energy between the depths of about 4 m and 6 m. The effect is caused by alternately constructive and destructive interference between the first surface and bottom reflections. With the transmitter at a depth of 5 m and 10 m deep water, a receiver depth of 5 m will cause the first two reflections to arrive at the receiver at the same time. The reflected energy will be at a minimum when the surface and bottom bounce arrive at exactly the same time, but with opposite phase. The graph illustrates this effect with a peak at a depth of just over 5 m.

Figure 2-9 does not show the full detail of the interference because the depth variation is too rapid. Figure 2-10 is an expanded view of the depth range 4.5 m to 5.5 m. This figure plots 500 data points while figure 2-9 shows only 200 points.

The first detail to notice is that there are in fact many more peaks and troughs to the response than shown in the previous graph. The distance between two successive peaks is
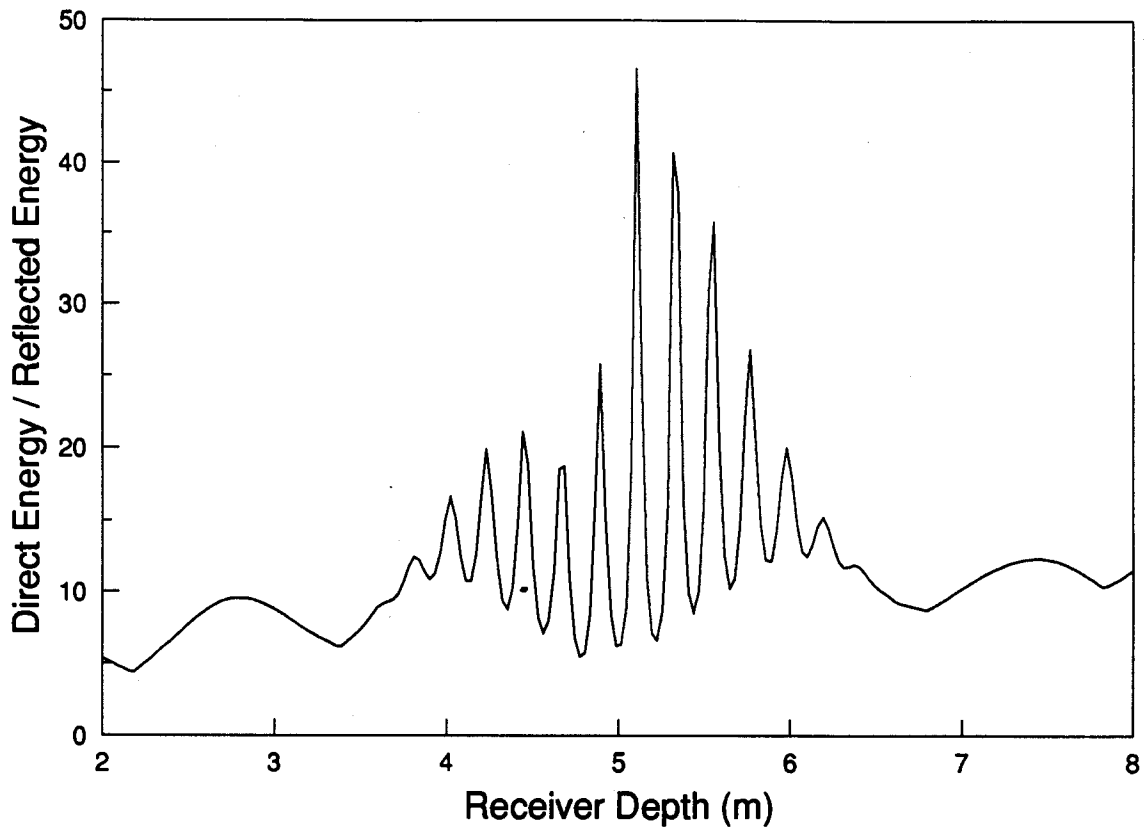
22

Figure 2-9 - Direct/Reflected Energy versus Receiver Depth

Parameter	Value	Parameter	Value
Water depth	10 m	Propagation speed	1500 m/s
Transmitter depth	5 m	Receiver depth	variable
Horizontal distance	5 m	Surface reflection loss	3 dB
Bottom reflection loss	10 dB	Absorption loss	3 dB/km
Carrier frequency	24000 Hz	Symbol rate	1000 Hz

about 3.6 cm, which is on the order of half of a wavelength. This result makes sense because a change in depth of roughly one half wavelength will cause a relative change of a full wavelength between the surface and bottom reflection.

This rapid variation in signal strength is a major source of difficulty with underwater acoustic communications. As the signal frequency increases the wavelength decreases and the variations occur more rapidly. It can, at times, become essentially impossible to predict the received signal amplitude. With this model it is at least possible to predict what circumstances might lead to the best or worst channel response.
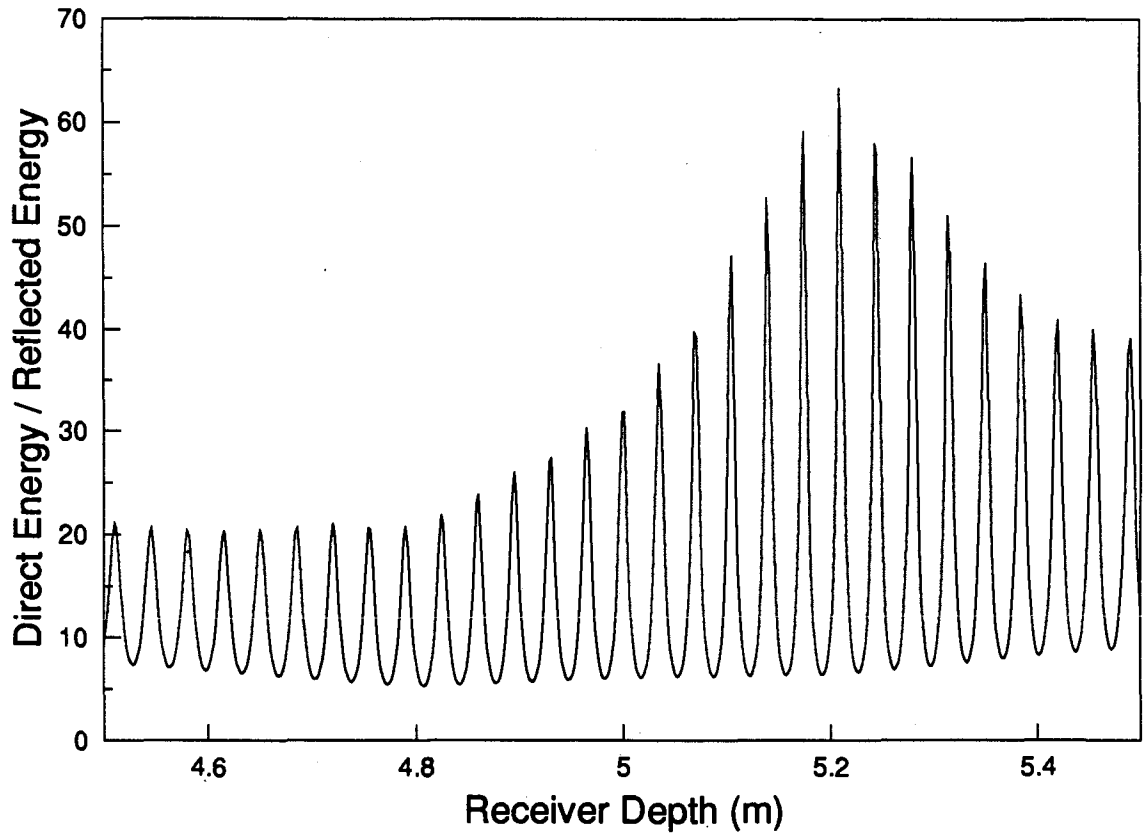
Parameter	Value	Parameter	Value
Water depth	10 m	Propagation speed	1500 m/s
Transmitter depth	5 m	Receiver depth	variable
Horizontal distance	5 m	Surface reflection loss	3 dB
Bottom reflection loss	10 dB	Absorption loss	3 dB/km
Carrier frequency	24000 Hz	Symbol rate	1000 Hz

Figure 2-10 - Direct/Reflected Energy versus Receiver Depth

### 2.3.3 Channel Response as a Function of Two Parameters

The next type of graph produced by the model is a 3D surface plot of the ratio of direct to reflected energy as a function of two parameters. The program generates up to 100 data points per axis. Figure 2-11 is a graph showing the response when the distance and depth are varied.

This 3D plot is essentially a combination of two previous graphs, figures 2-8 and 2-9. As in figure 2-9, this graph shows that at certain receiver locations the response varies wildly. For example, when the receiver is close to the source and at depths around 5 m the reverberant energy fluctuates by up to 17 dB with a small change in location. However, closer to the boundaries the fluctuations are slower and smaller in magnitude.

The physical explanation is that at certain receiver locations the surface and bottom returns arrive at the receiver at the same time and so interfere with one another. Hence a small change in the location of either the transmitter or receiver will cause a change in the interference pattern. However, at other depths the large returns do not overlap in time. The smaller variations are then due to the interference of the subsequently weaker reflections.

As mentioned earlier, the channel measure of direct/reflected energy does not account for interference between the direct and multipath arrivals. Figure 2-12 is a 3D plot using the second channel measure: the ratio of energy in the first received symbol to the sum of the energy in all subsequent symbol periods. All the model parameters are the same as in figure 2-11.

When there is no overlap between the direct and multipath arrivals then the two channel measures are identical because the first symbol contains energy from only the direct arrival. Thus the data in figures 2-11 and 2-12 are the same when the horizontal distance is less than 15 m. At greater distances and when the receiver is near to either the surface or the bottom, figure 2-12 shows the effect of interference with the direct arrival. The effect is more noticeable near the surface because the reflection loss is much less than at the bottom.
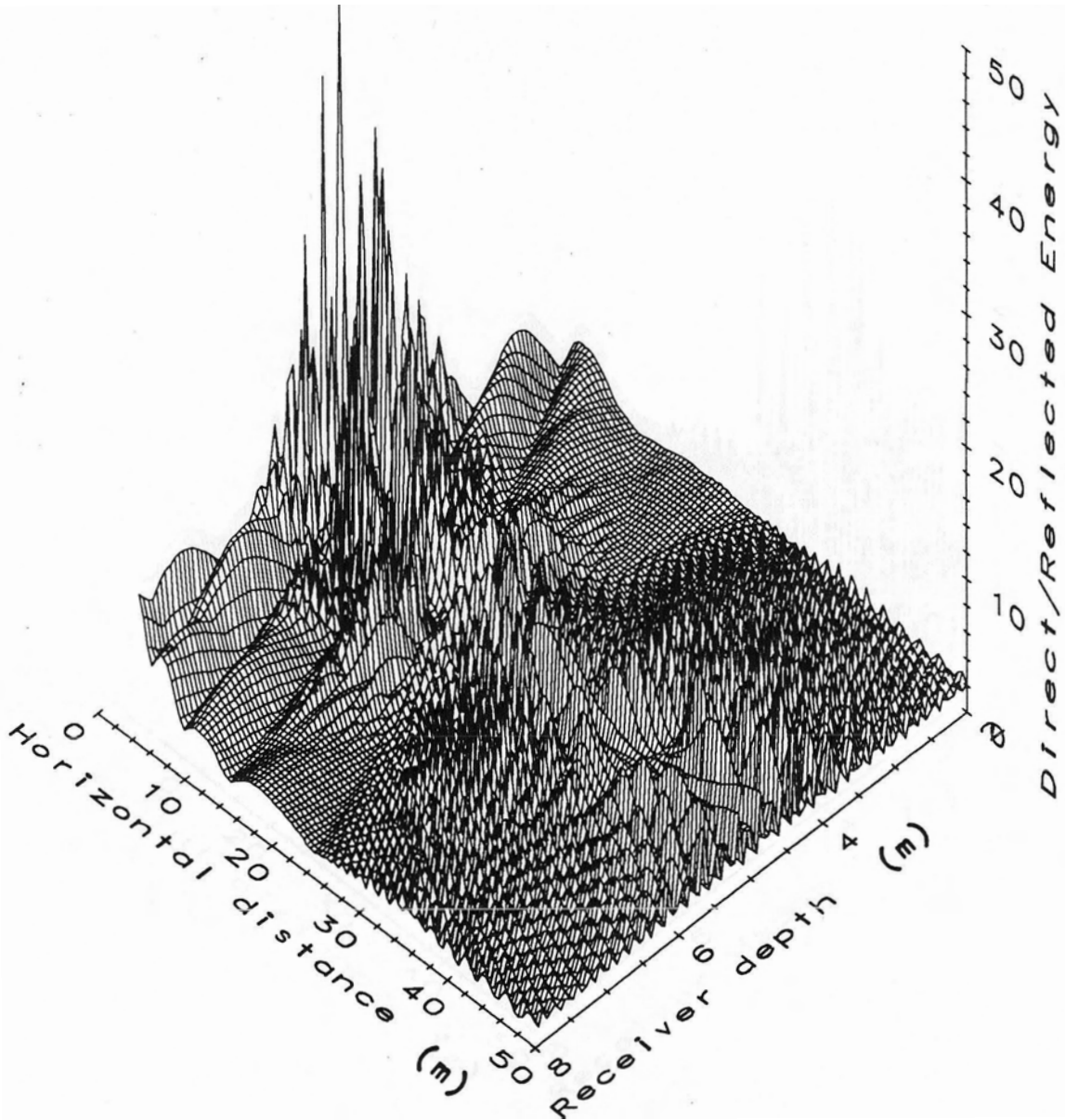
Parameter	Value	Parameter	Value
Water depth	10 m	Propagation speed	1500 m/s
Transmitter depth	5 m	Receiver depth	variable
Horizontal distance	variable	Surface reflection loss	3 dB
Bottom reflection loss	10 dB	Absorption loss	3 dB/km
Carrier frequency	24000 Hz	Symbol rate	1000 Hz

Figure 2-11 - 3D Plot of Direct/Reflected Energy
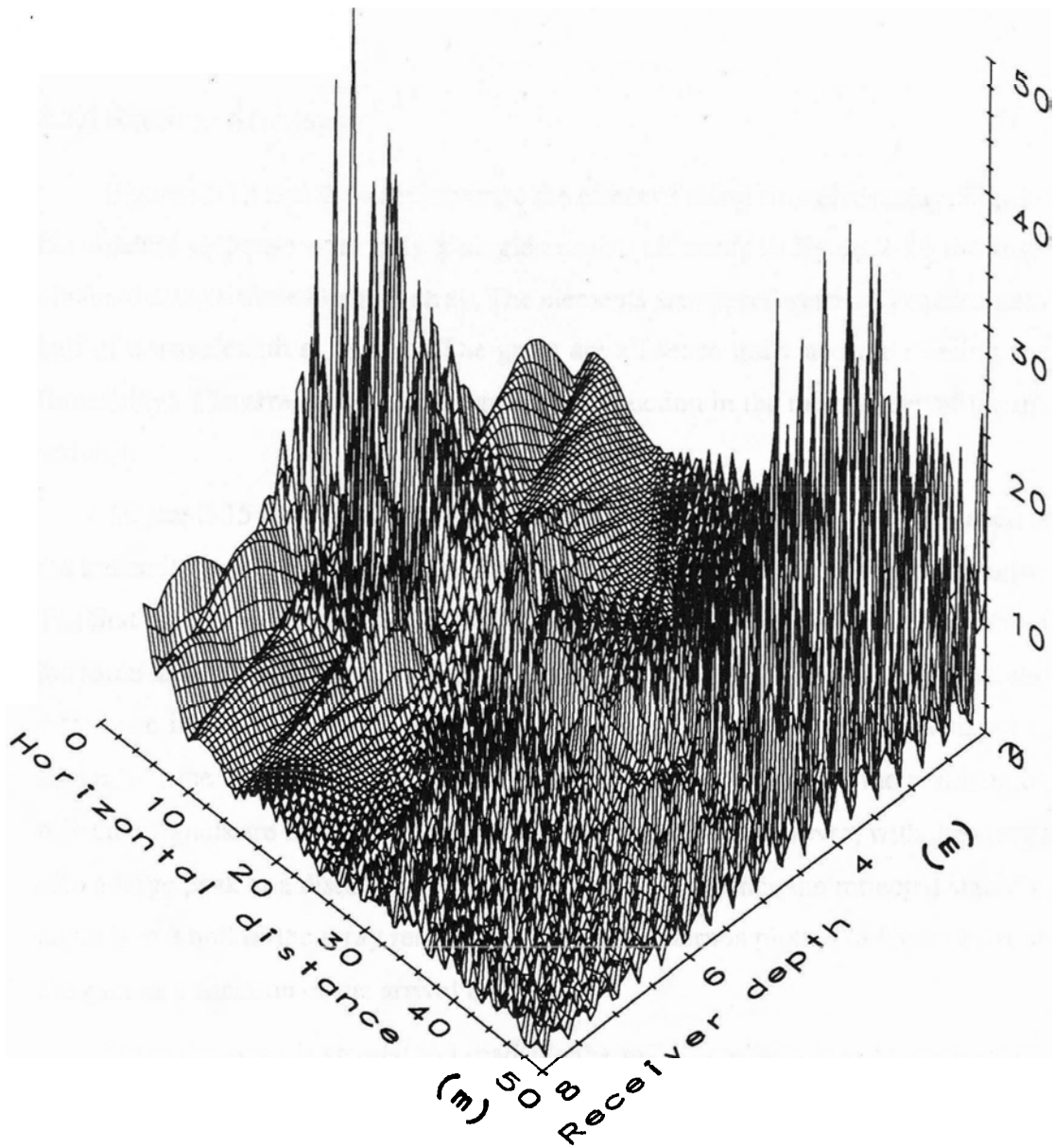
Parameter	Value	Parameter	Value
Water depth	10 m	Propagation speed	1500 m/s
Transmitter depth	5 m	Receiver depth	variable
Horizontal distance	variable	Surface reflection loss	3 dB
Bottom reflection loss	10 dB	Absorption loss	3 dB/km
Carrier frequency	24000 Hz	Symbol rate	1000 Hz

Figure 2-12 - 3D Plot of Energy in First Symbol/Subsequent Symbols

2.3.4 Receiver Arrays

Figures 2-13 and 2-14 demonstrate the effect of using a receiver array. Figure 2-13 is the channel response with only a single receive element; in figure 2-14 the response is obtained using a three element array. The elements are spaced vertically at distances of one half of a wavelength at 24 kHz. The gains are all set to unity and the steering angle is 0 (broadside). The array produces a significant reduction in the magnitudes of the multipath arrivals.

Figure 2-15 is a plot of the response as a function of the horizontal distance between the transmitter and receiver. The parameters are identical to those of the previous two plots. The first line shows the direct/reflected energy with a single element while the second shows the same measure using the 3 element array. The last line, labelled "difference", shows the difference in dB between the direct/reflected energy with the array and without it. As in figure 2-8, the difference is largest at the closest distance because the pathlengths of the reflected signals are much greater than the direct distance. However, with the array there is also a large peak at a distance of about 10 m. At this distance the reflected signal's arrival angle is in a null of the array response. The array pattern is plotted in figure 2-16, showing the gain as a function of the arrival angle.

Since the array is steered to broadside the maximum gain is at an angle of 0°. There are two nulls occurring at roughly ±40°, which corresponds to the arrival angles of the surface and bottom bounces at the peak in figure 2-15.

The next graph, figure 2-17, shows the channel response when the array spacing is increased from half a wavelength (3.125 cm) to a full wavelength (6.25 cm). The most noticeable effect is the appearance of another peak in the response at a distance of 22 m. Again the peak is the result of a null in the array response, as shown in figure 2-18. With the wider spacing there are now two pairs of nulls at ±40° and ±20°.
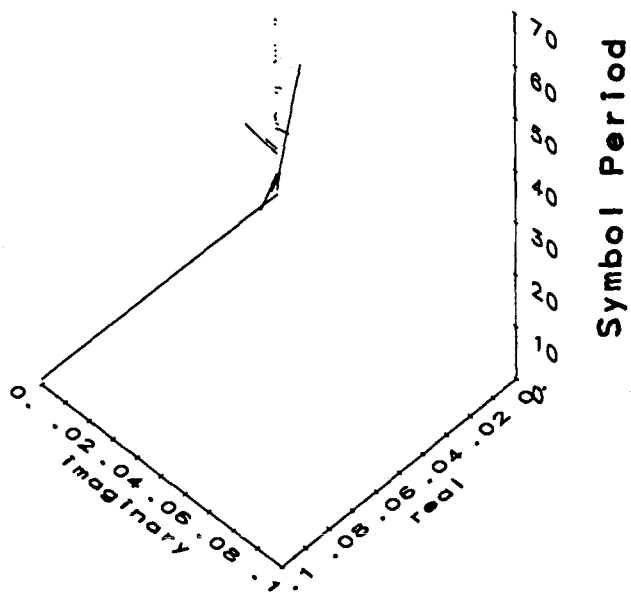
Parameter	Value	Parameter	Value
Water depth	10 m	Propagation speed	1500 m/s
Transmitter depth	4 m	Receiver depth	4 m
Horizontal distance	10 m	Surface reflection loss	3 dB
Bottom reflection loss	10 dB	Absorption loss	3 dB/km
Carrier frequency	24000 Hz	Symbol rate	1000 Hz

Figure 2-13 - Complex Response With a Single Receive Element
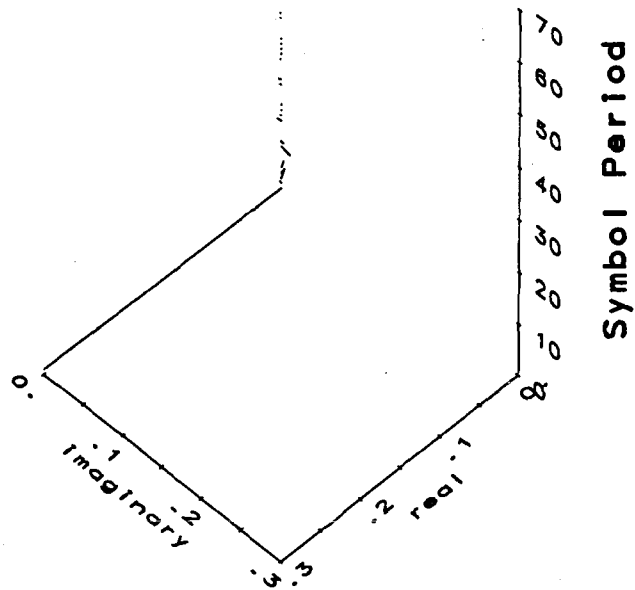
Parameter	Value	Parameter	Value
Water depth	10 m	Propagation speed	1500 m/s
Transmitter depth	4 m	Receiver depth	4 m
Horizontal distance	10 m	Surface reflection loss	3 dB
Bottom reflection loss	10 dB	Absorption loss	3 dB/km
Carrier frequency	24000 Hz	Symbol rate	1000 Hz

Figure 2-14 - Complex Response With a 3 Element Receive Array
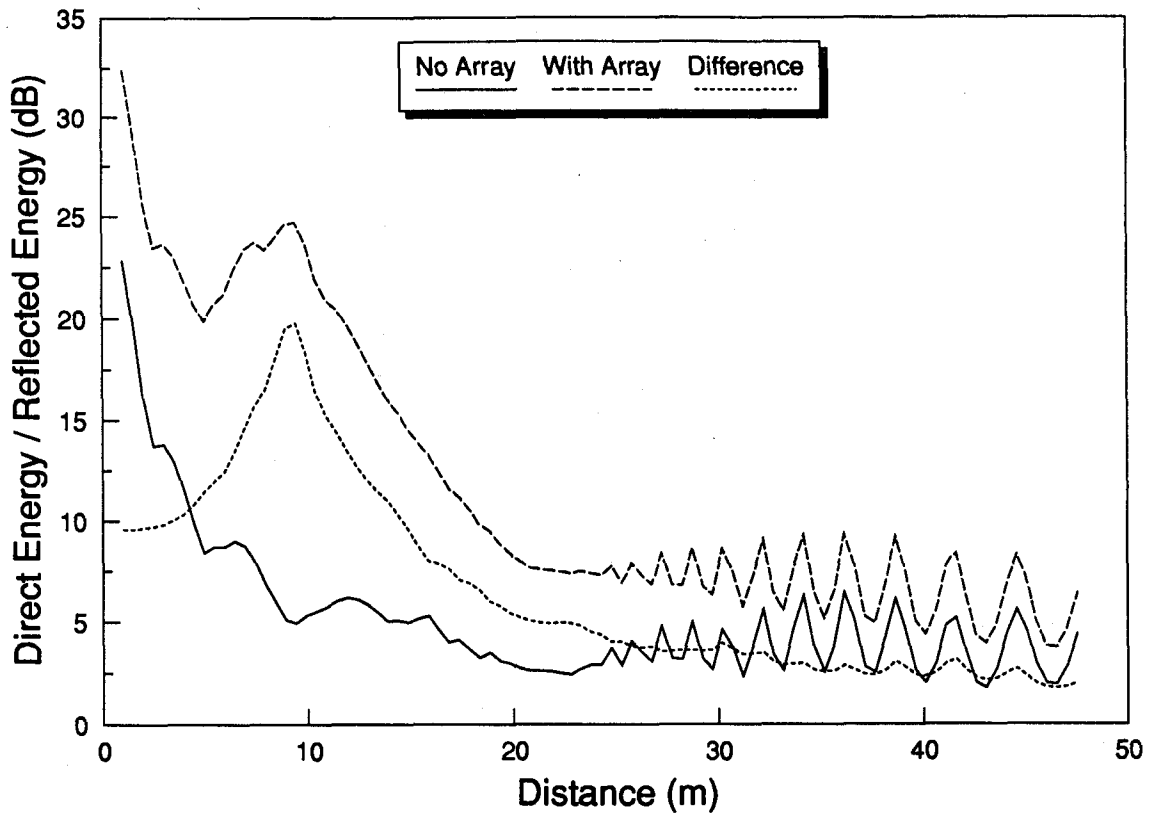
Parameter	Value	Parameter	Value
Water depth	10 m	Propagation speed	1500 m/s
Transmitter depth	4 m	Receiver depth	4 m
Horizontal distance	variable	Surface reflection loss	3 dB
Bottom reflection loss	10 dB	Absorption loss	3 dB/km
Carrier frequency	24000 Hz	Symbol rate	1000 Hz

Figure 2-15 - Direct/Reflected Energy with a Receiver Array

In all of the examples so far the array has been steered precisely in the direction of the transmitter. The next set of data in figure 2-19 shows the response when the receiver moves out of the main lobe of the array pattern. The receiver array has three elements spaced at half wavelengths; figure 2-16 gives the corresponding array pattern.
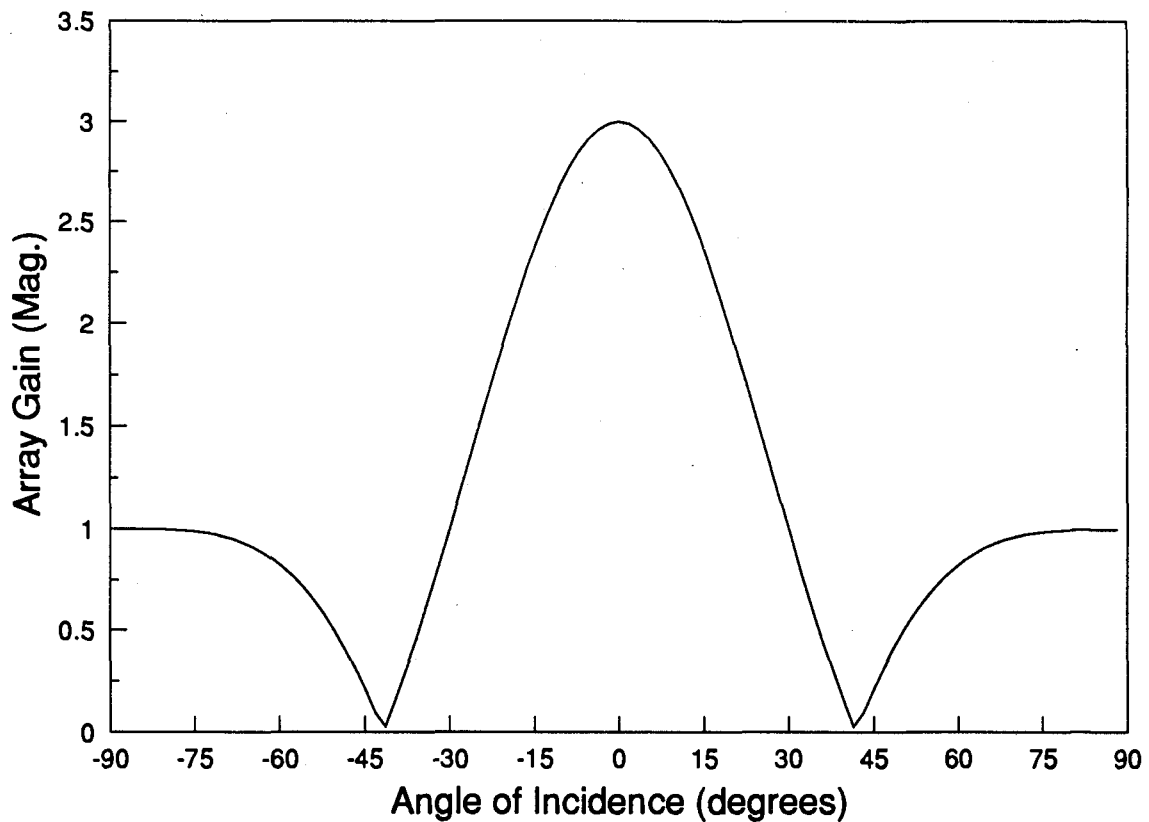
Figure 2-16 - Array Pattern for a 3 Element Array

The graph shows the response as the receiver changes depth from the surface down to the bottom at 100 m. The array is steered broadside; since the transmitter is at a depth of 50 m the receiver will be broadside when it is also at a depth of 50 m. Thus there is a large peak in the response at a depth of 50 m where the gain of the array over a single hydrophone is largest (about 10 dB).

Note that the array only achieves a gain over the single hydrophone in the depth range of 45 m to 55 m, i.e. when the direct arrival is in the main lobe of the array pattern. At the depths of 40 m and 50 m the array does very poorly because the direct arrival is in a null. Above 40 m and below 50 m there is little difference between the array and the single hydrophone system.

This data leads to the conclusion that a fixed array is only useful when the transmitter and receiver are also at fixed locations. When communicating with an ROV, for example, the receiver array must be able to track the direct arrival. For even better performance, one can envision an adaptive system which not only steers the main lobe towards the direct arrival, but also places the multipath returns in nulls of the array pattern.
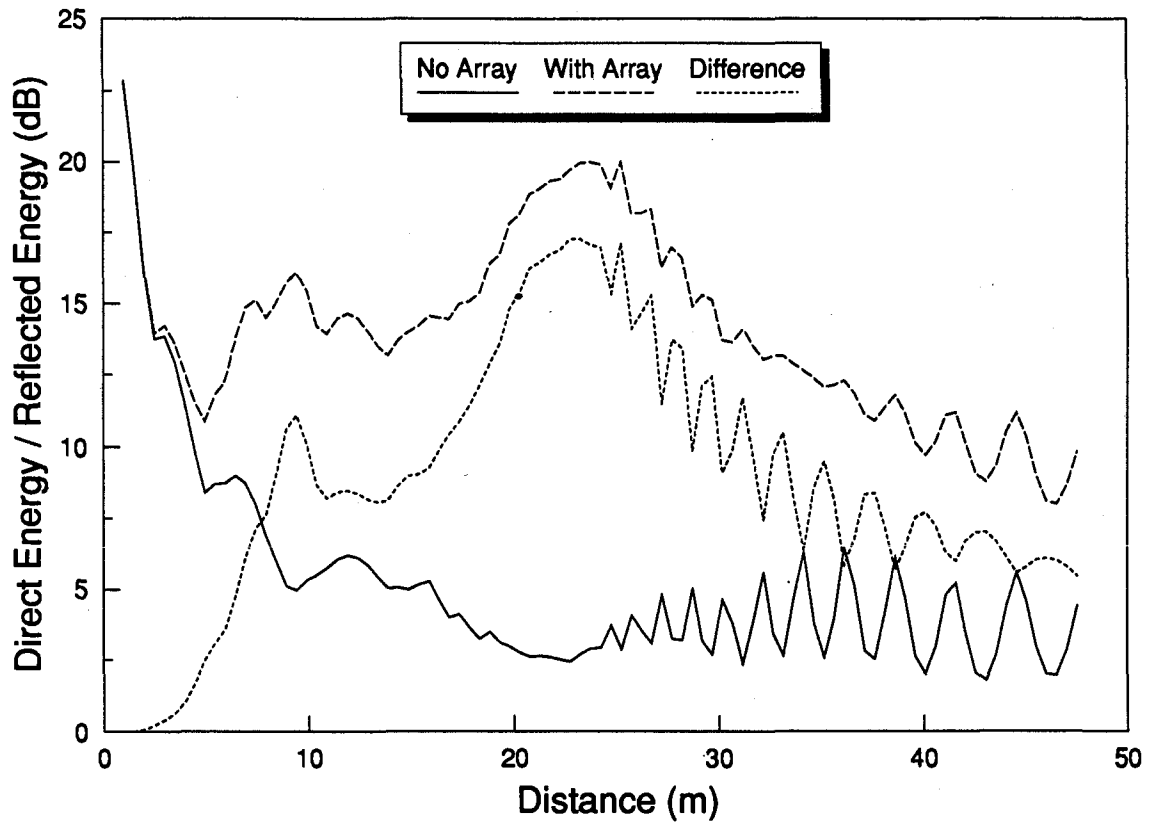
Parameter	Value	Parameter	Value
Water depth	10 m	Propagation speed	1500 m/s
Transmitter depth	4 m	Receiver depth	4 m
Horizontal distance	variable	Surface reflection loss	3 dB
Bottom reflection loss	10 dB	Absorption loss	3 dB/km
Carrier frequency	24000 Hz	Symbol rate	1000 Hz

Figure 2-17 - Channel Response with Wider Spacing of Array Elements

33

Diversity techniques are commonly employed in communications systems to combat fading. Underwater telemetry systems have used both frequency and spatial diversity. The frequency diversity sometimes takes the form of frequency-hopped spread spectrum [7]. Other systems transmit simultaneously over multiple carriers and introduce redundancy through coding [8].
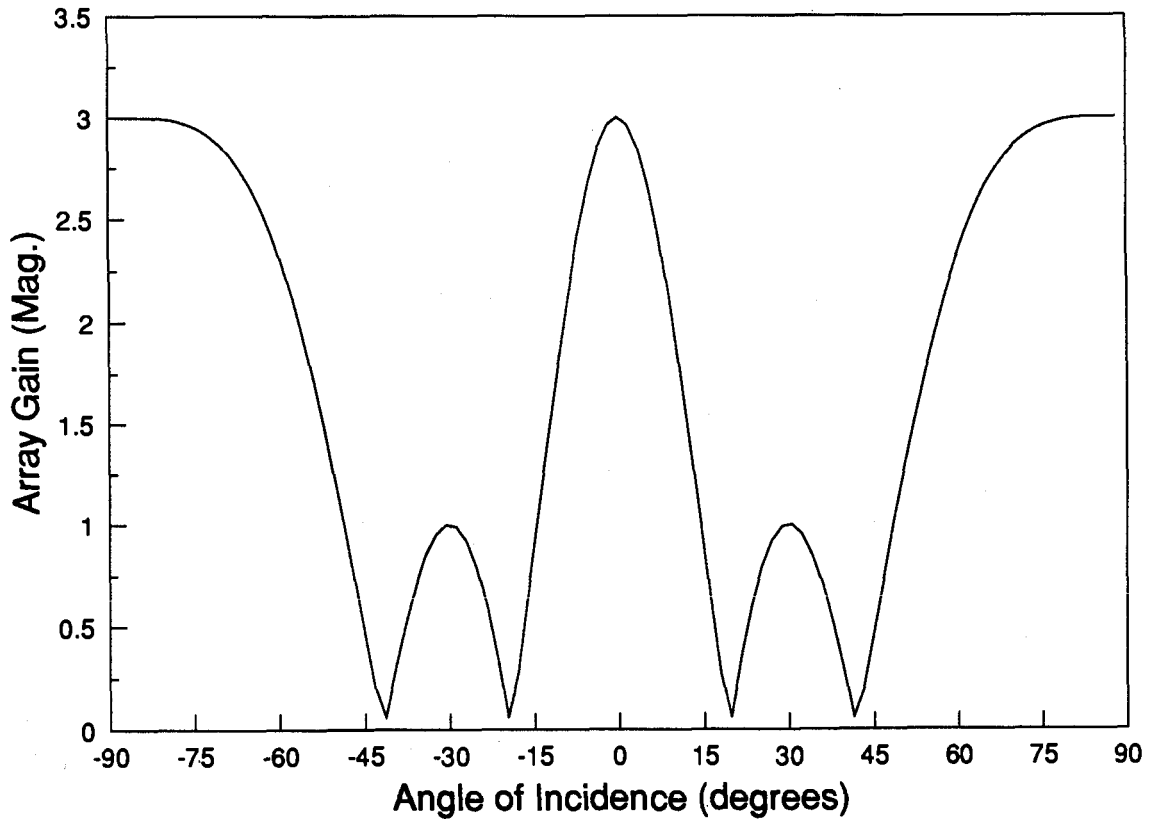
Figure 2-18 - Array Pattern with One Wavelength Spacing

Better reliability can also be obtained with spatial diversity processing. For example, Catipovic et al. [9] use a set of widely spaced hydrophones for diversity in their 10 kbps system. Widely spaced, in this instance, refers to separations of several metres. The large distances are used in order to defeat interference sources such as bubble plumes, which can

34

be up to 10 m wide. The signals are combined with a weighted sum based upon an estimate of each channel's quality. The authors reported substantial improvements in the bit error rate after testing the spatial diversity system in a shallow harbour.
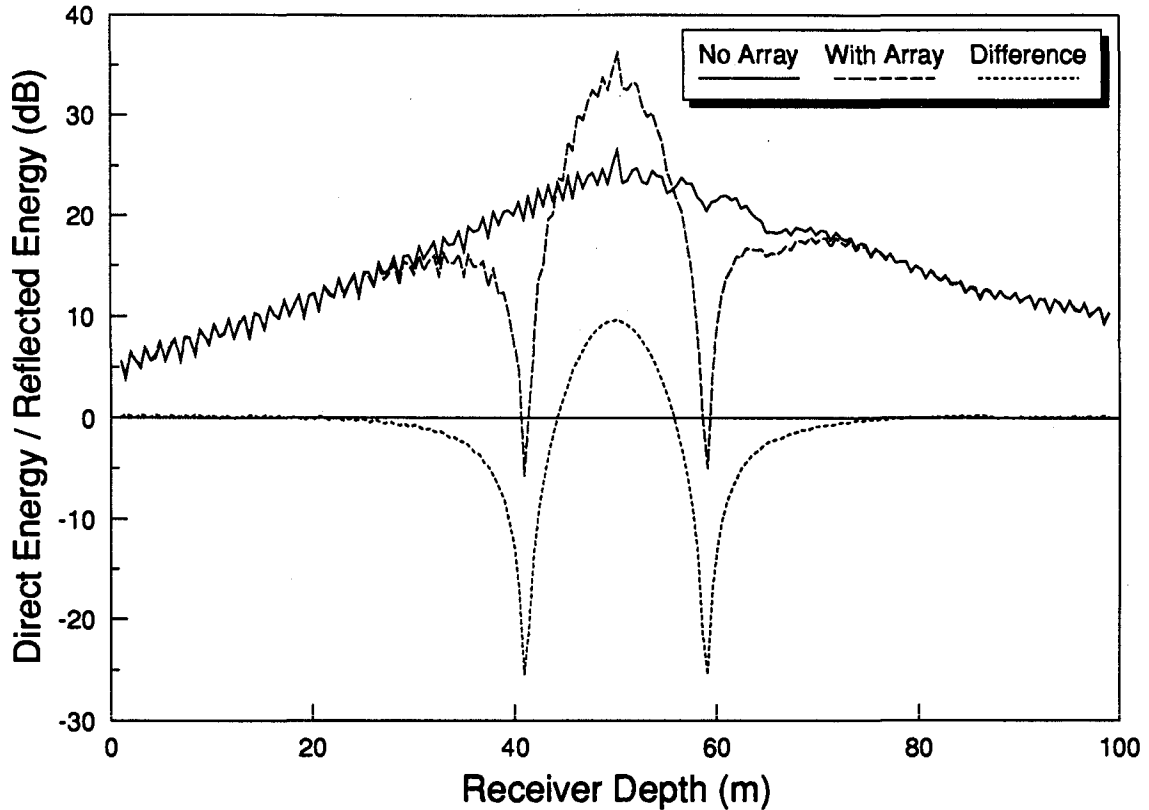
Parameter	Value	Parameter	Value
Water depth	100 m	Propagation speed	1500 m/s
Transmitter depth	50 m	Receiver depth	variable
Horizontal distance	10 m	Surface reflection loss	3 dB
Bottom reflection loss	10 dB	Absorption loss	3 dB/km
Carrier frequency	24000 Hz	Symbol rate	1000 Hz

Figure 2-19 - Response with an Unsteered Receiver Array

A receiver array is often composed of a set of closely spaced ($\lambda/2$) hydrophones which are used for beamforming. However, it is also possible to view the array as a spatial diversity receiver. Horvat et al. [10] have developed a true time-delay beamformer for this purpose.

35

The modelled receiver arrays presented in this section are based upon this technique. One advantage of this time domain implementation is its ability to combine signals from widely spaced elements. Therefore it may be useful not only for conventional beamforming applications, but also for spatial diversity systems. Further research is required to determine the technique's applicability in a communications system.

3 Characterization of Acoustic Transducers

This chapter discusses the characteristics of the transducers used for collecting the experimental data. A thorough investigation of the transducers is important for at least two reasons. First, it is necessary to provide adequate information for other researchers to compare their past or future results with those presented here. Unfortunately, much of the literature dealing with a characterization of the underwater channel gives little or no information about the transducers that were used.

Second, the transducers are important elements in the complete communications system. Our experimental findings indicate that the transducers have a significant effect upon the received signal quality. It is unrealistic to assume that the transducers are well-behaved linear elements. Much of the data presented in this section is referred to in later sections, where an analysis of the observed channel behavior is presented.

This chapter also includes a discussion of the transmit and receive amplifiers. Their frequency response and noise characteristics are detailed, as well as the electrical interfaces to the transducers. The noise data is used later in section 4.3 which analyzes the noise components of the experimental setup.

3.1 Acoustic Projector

The acoustic projector is a hollow, cylindrical piezoelectric element composed of the ceramic material PZT-4, which is encased in a plastic (poly vinyl chloride) shell. Figure 3-1 is a diagram of the projector's construction. The projector was provided by Simrad Mesotech, a local manufacturer of sonar systems.
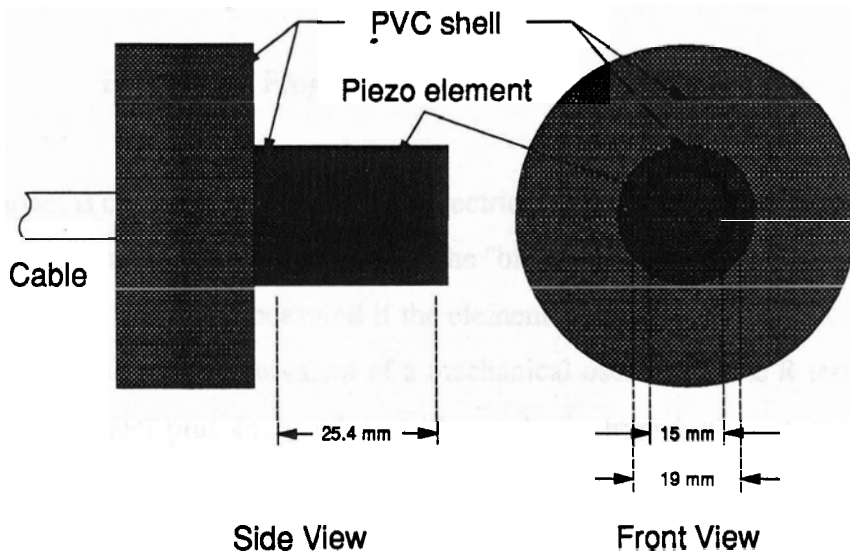
Figure 3-1 - The Acoustic Projector

The projector was designed to have a resonant center frequency at 24 kHz. This value was checked experimentally by measuring the frequency response of the projector. The

38

response was determined by measuring the input admittance of the projector over the relevant frequency range. To see the relation between the input admittance and output response of the projector we must consider an electrical equivalent model as shown in figure 3-2.
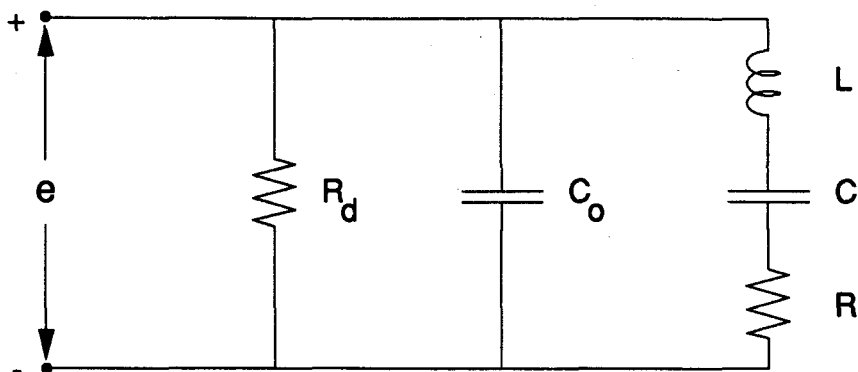
Figure 3-2 - Projector Electrical Equivalent Circuit

This model is commonly used for piezoelectric projectors [22]. The resistive element R_d represents dielectric losses. C_o is known as the "blocked" or "clamped" capacitance; it is the capacitance that would be measured if the element was prevented from vibrating. The LCR branch is the electrical equivalent of a mechanical oscillator. The R term represents the loading of the water plus any mechanical losses in the transducer and its mounting. In most cases the mechanical losses can be assumed negligible [23]. The acoustic power output is then given by

$$P_o = \overline{e^2} |Y|^2 R \qquad (3.1)$$

where e is the input signal voltage, as shown in figure 3-2, and Y is the admittance of the mechanical branch. The input admittance Y_{in} is the sum of the admittance of the three branches of the equivalent circuit. The last term in equation 3.2 below is the admittance of the mechanical branch.

$$Y_{in} = \left(\frac{1}{R_d} + j\omega C_o \right) + \frac{1}{R + j\omega L + \frac{1}{j\omega C}} \qquad (3.2)$$

Thus the frequency response determined by measuring the input admittance is not exactly the projector's output response because of the clamped capacitance and dielectric loss terms. However the dielectric losses are usually comparatively small, with R_d having a value on the order of several mega-ohms. Any mechanical losses will also reduce the acoustic power transmitted into the water.

The input admittance of this projector is also affected by the presence of a series inductor. In practical systems it is usually desirable to transform the input impedance of the projector in order to present a purely resistive load to the output amplifier. The blocked capacitance C_o makes the projector's reactance capacitive at the operating (resonant) frequency. An inductor can be used to tune out the capacitive reactance at the appropriate frequency [24].

Figure 3-3 shows the magnitude and phase of the projector's input admittance over the range of 3 kHz to 35 kHz. The admittance was determined by placing a small valued resistor (30 Ω) in series with the projector; the voltage across the resistor was measured as the frequency of the input signal was swept over the desired range. The admittance is proportional to voltage amplitude across the resistor, as long as the input amplitude remains constant. Some adjustment of the signal generator's amplitude was required as the output sagged near the resonant frequency of the projector. The projector was immersed in the centre of a 4 m by 4 m by 1.5 m deep test tank at a depth of 75 cm.

40
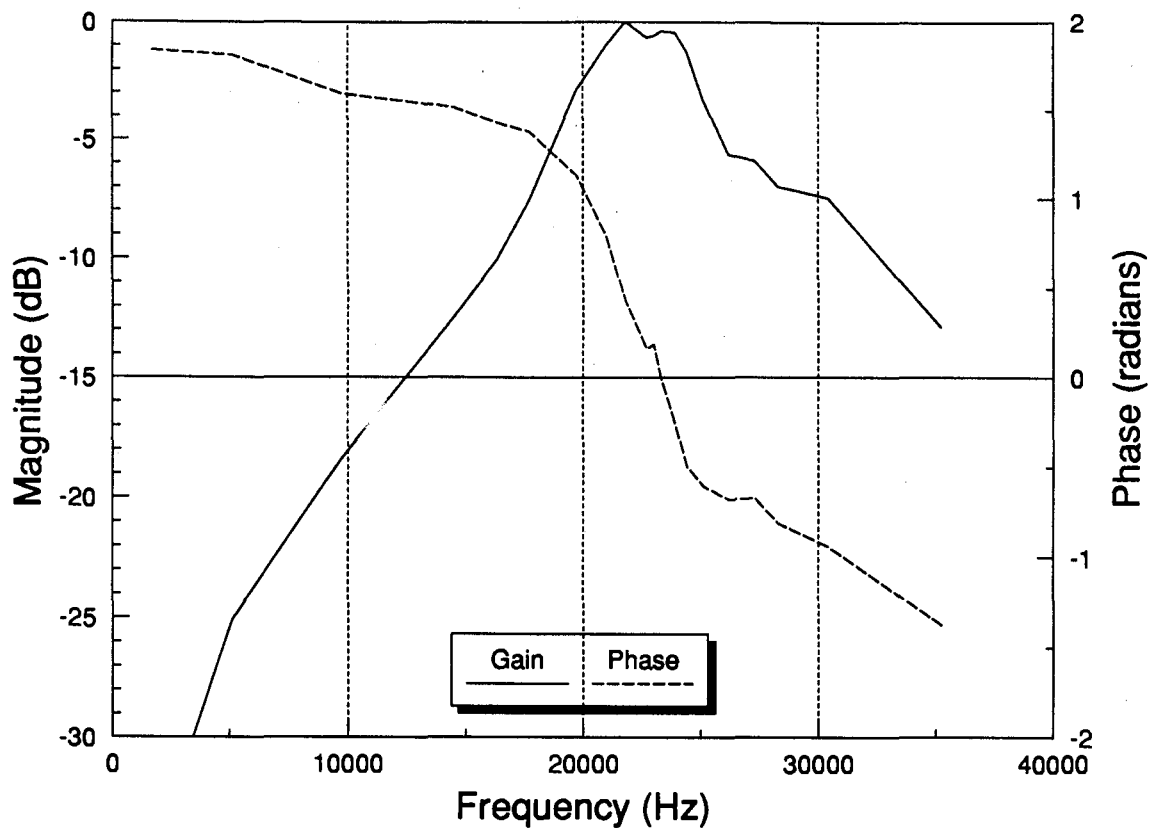
Figure 3-3 - Frequency Response of the Projector

The peak of the response occurs at 22 kHz, but the centre frequency of the response is closer to the predicted value of 24 kHz . The 3 dB bandwidth is about 7 kHz, which corresponds to a Q of 3.1. There are smaller peaks in the admittance at 24 kHz and 27 kHz.

These multiple resonant frequencies correspond to different mechanical resonance points of the cylindrical vibrating element. It can be shown that the resonant frequencies of the various vibratory modes of a cylindrical shell lie within a relatively small frequency range [25]. In practice, it is very difficult to analytically determine the parameters for all the vibratory modes.

A useful format for graphing the admittance data is the circle diagram, which plots the imaginary part of the admittance (susceptance) on the Y axis against the real part (conductance) on the X axis. If the points are measured as the frequency is swept through the region of resonance an approximation to a circle should result, as shown in figure 3-4.
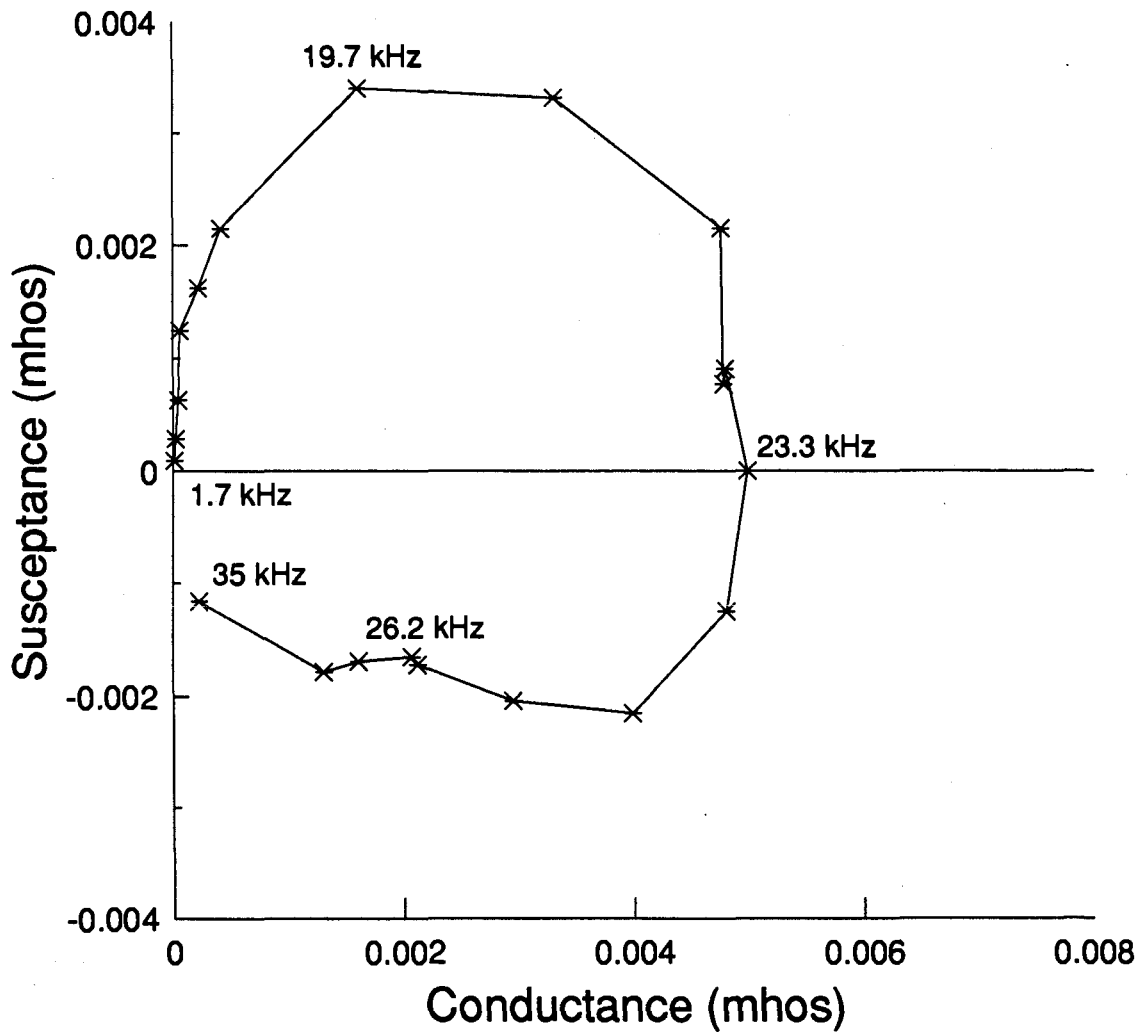
Figure 3-4 - Circle Diagram of the Projector Admittance

The plot starts at the lowest frequency, and moves clockwise as the frequency increases. Each data point is marked with an "x"; a few have been labelled with their corresponding frequency. The resonant frequency appears at the right of the plot. The admittance at resonance can be read from the graph as 0.005 mhos, which corresponds to a resistance of 200 ohms. However, to be more precise the 30 ohm series resistance should be subtracted to arrive at a value of 170 ohms for the impedance of the projector at resonance.

In order to double check the experimentally measured response we can predict the values of the equivalent circuit components based upon the characteristics of the piezoelectric element. Church and Pincock described a procedure for determining these values for a thin wall ceramic cylinder [26]. The data required for the calculations are summarized below in table 3-1.

Parameter	Description
$r1 = 0.007493$ m	Inner radius
$r2 = 0.009525$ m	Outer radius
$l = 0.0254$ m	Length
$\varepsilon = 1250$	Relative dielectric constant
$\rho = 7600$ kg/m^3	Density
$N = 41$ kHz·inch	Frequency constant
$k_{31} = 0.30$	Mechanical coupling coefficient

Table 3-1 - Piezoelectric Dimensions and Constants

The first three values are simply the dimensions of the element. The last four are properties of the piezoelectric material. These values were taken from the paper by Church and Pincock, who refer to the material at "Type-4"; it is also commonly known as PZT-4. A more complete listing of values is given in [27]. The calculated component values and the predicted resonant frequency are listed in table 3-2.

The Q value of the mechanical branch can also be calculated using the above results and the following relation

$$Q = \frac{1}{R} \cdot \sqrt{\frac{L}{C}}$$

(3.3)

The calculated Q value is 3.1, which matches the experimentally measured value. The value calculated for C_o is 7.36 nF, which is reasonably close to the measured value of 8.1 nF. C_o was determined by matching the slope of the projector's admittance curve at low frequencies with a capacitor substitution box [28].

The calculated value for the impedance at resonance is 2.87 kΩ. This differs by more than an order of magnitude from the experimentally measured value of 170 Ω. The discrepancy is caused by the addition of the series inductor. An inductance of about 4.5 mH is required to tune out the blocked capacitance and produce a purely real input impedance at the calculated resonant frequency of 27.4 kHz. The resulting impedance is 211 Ω, which is reasonably close to the experimentally determined value.

The impedance value can also be estimated by measuring the acoustic power radiated by the projector and then calculating the radiation impedance, given the input voltage to the projector. Using the data that will be given in section 4.3.3, a result of 140 Ω is obtained. Thus the two experimentally determined values are also reasonably close.

Parameter	Value
C_o	7.36 nF
L	51.0 mH
C	0.66 nF
R	2.87 kΩ
f_r	27.4 kHz

Table 3-2 - Calculated Projector Parameters

One discrepancy in the calculated values is with the resonant frequency. The calculated frequency is 27.4 kHz but the measured projector response showed a centre frequency at about 24 kHz. According to the projector's manufacturer, such discrepancies between the calculated and measured values for the resonant frequency are not uncommon. Therefore it is important to characterize the transducer's response when using it in a communications system.

3.2 Output Amplifier

The projector is driven by a 120 watt linear power amplifier. The manufacturer specifies the high frequency cutoff as 100 kHz. Measurements verified that the -3 dB point was at 110 kHz, with the rolloff beginning at about 60 kHz. There is also noticeable distortion of the output signal starting at 60 kHz.

The gain of the amplifier is 37 dB at 24 kHz. The maximum input level is 1.6 volts peak to peak, which corresponds to an output of 110 volts peak to peak.

3.3 Hydrophones

The hydrophones are also piezoelectric transducers, supplied by Simrad Mesotech. At the operating frequency of 24 kHz the hydrophones are designed to be omnidirectional and have a flat frequency response across the receive bandwidth.

The sensitivity of the hydrophones was determined by measuring their output levels relative to a calibrated hydrophone. The measured values are listed below in table 3-3, both in absolute units of μV per Pascal and in dB relative to a standard value of 1 volt per μPa.

Hydrophone	Sensitivity	
	$\mu V/Pa$	re $1V/\mu Pa$
1	16.8	-215.5 dB
2	14.7	-216.7 dB
3	15.0	-216.5 dB

Table 3-3 - Measured Hydrophone Sensitivity

It is possible to predict the hydrophone sensitivity given the dimensions and material properties of the piezoelectric element [29]. Equation 3.4 gives the sensitivity of a cylindrical hydrophone vibrating in the radial mode. Equation 3.5 is an expression for calculating the blocked capacitance of the hydrophone, again vibrating in the radial mode.

$$\frac{e}{p} = r_2 \left[\frac{d_{33}}{\epsilon\epsilon_0} \left(\frac{r_2 - r_1}{r_2 + r_1} \right) + \frac{d_{31}}{\epsilon\epsilon_0} \right] \tag{3.4}$$

$$C = \frac{2\pi\varepsilon\varepsilon_0 l}{\ln\left(\frac{r_2}{r_1}\right)}$$

(3.5)

The data required for equations 3.4 and 3.5 are summarized below in table 3-4. The material data was taken from Albers [30].

Parameter	Description
$r1 = 0.009525$ m	Inner radius
$r2 = 0.0127$ m	Outer radius
$l = 0.0127$ m	Length
$\varepsilon = 1300$	Relative dielectric constant
$d_{33} = 285 \times 10^{-12}$ N/C	Parallel piezoelectric strain coefficient
$d_{31} = -122 \times 10^{-12}$ N/C	Orthogonal piezoelectric strain coefficient

Table 3-4 - Hydrophone Dimensions and Constants

The calculated value for the hydrophone sensitivity is -207 dB re 1V/μPa, which is 10 dB off from the measured value of -217 dB. However, when calculating the sensitivity one must take into consideration the loss due to the capacitance of hydrophone cable. Figure 3-5 shows an equivalent circuit for the hydrophone, cable and input stage of the amplifier [31].

For the moment we will disregard the input impedance of the amplifier; it will be dealt with in the next section. The hydrophone signal is attenuated because of the voltage-divider
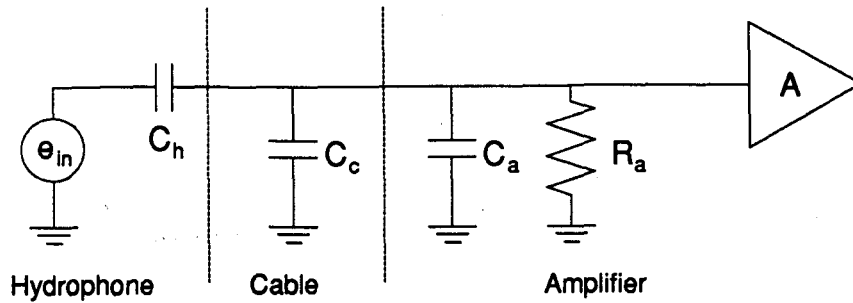
47

Figure 3-5 - Equivalent Circuit of Hydrophone, Cable and Amplifier

formed by the cable capacitance C_c and the hydrophone capacitance C_h. The loss factor is then just the ratio of C_h to the total capacitance (equation 3.6). Thus it is desirable to minimize the length of the hydrophone cables in order to maximize the sensitivity.

$$\frac{e_a}{e_{in}} = \frac{C_h}{C_h + C_c} \tag{3.6}$$

The capacitance of the hydrophones plus the cable was determined experimentally with a low frequency bridge measurement. The measured value was 2.5 nF for each hydrophone plus cable. The 15 metre cable has a rated capacitance of 100 pF per metre. Therefore the cable capacitance C_c is 1.5 nF while the hydrophone capacitance C_h is 1.0 nF. From equation 3.6 the loss due to the cable is then 8.1 dB.

Taking this loss into account lowers the calculated sensitivity from -207 dB re 1V/μPa to -215.1 dB, which differs less than 2 dB from the measured value.

From equation 3.5, the calculated value for the hydrophone's (blocked) capacitance is $C_o = 3.19$ nF. This value is compares to the experimentally determined value of 1.0 nF. Part

48

of this discrepancy may be due to errors in the estimation of the piezoelectric element's dimensions. For small piezo elements a measurement of C_o is probably preferable to a calculated estimate.

3.4 Receive Amplifiers

The signals from the hydrophones are amplified and filtered before being sampled by the A/D converter. Each channel has a front end filter followed by a two stage, fourth order Butterworth bandpass filter. The filters are designed and tuned to have a 4 kHz wide 3 dB bandwidth, centred at 24 kHz. The measured frequency response of the filters is graphed in figure 3-6.

As mentioned earlier, the input impedance of the amplifier will affect the sensitivity of the system. As shown in the equivalent circuit of figure 3-5, the amplifier has an input capacitance C_a and an input resistance R_a. In accordance with equation 3.6, the sensitivity will decrease as C_a increases because the amplifier capacitance adds in parallel with the cable capacitance. The resistive element R_a forms a high pass network with a corner frequency at

$$f_c = \frac{1}{2\pi R_a (C_a + C_h + C_c)}$$
(3.7)

The input capacitance of the JFET amplifier is negligible. The input resistance R_a is determined by our choice of input resistor. Clearly, R_a must be chosen large enough so that the high pass cutoff frequency is well below the signal frequency range. However, while it is desirable to make the resistance large in order to increase the sensitivity, there is a drawback

in that the level of electronic input noise increases with the resistance. Therefore R_a should not be chosen to be some arbitrarily large value. The input resistor was thus chosen to be 100 kΩ, which gives a lower cutoff frequency of 650 Hz.
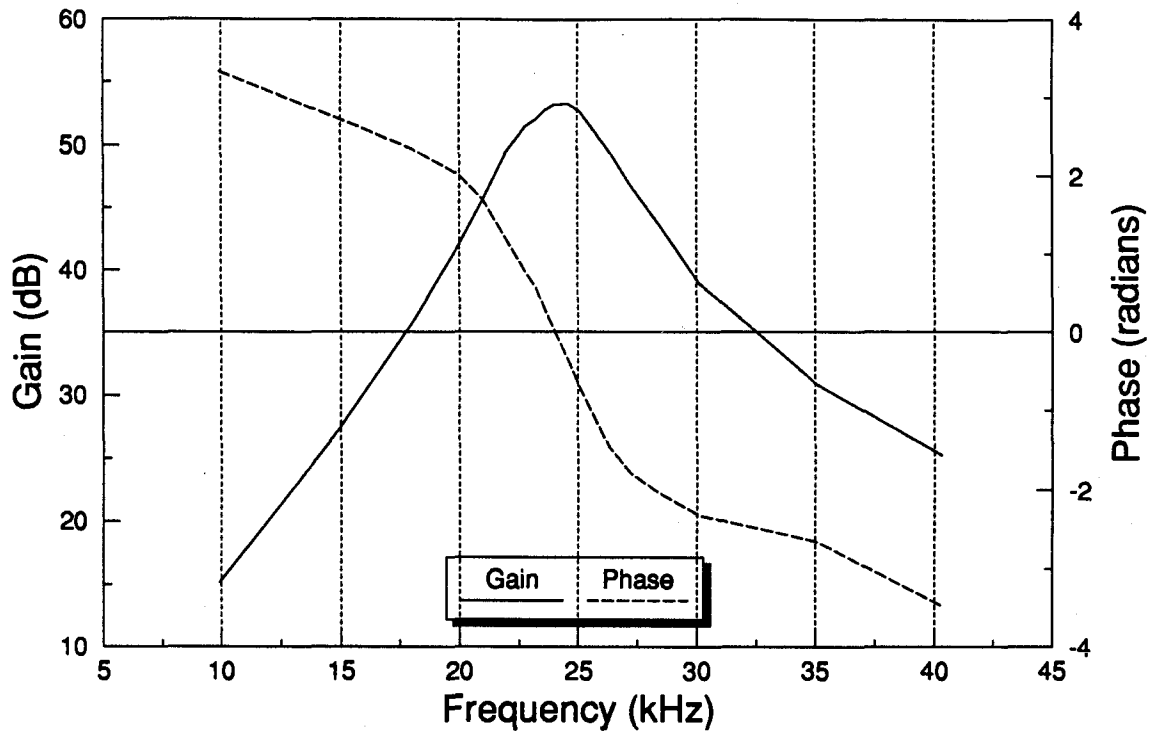
Figure 3-6 - Frequency Response of Receiver Filters

3.5 Amplifier Noise

There are three main components to the electronic noise in the receive amplifier [32]. The first two are the voltage and current noise sources associated with the opamp's internal circuitry. Good voltage and current noise characteristics can be obtained by choosing a low

noise operational amplifier, such as the TL071 used in the testbed receiver. This device has JFET inputs, resulting in a current noise input i_n of only 0.01 $pA/\sqrt{Hz}$. The voltage noise input e_n is rated at 18 $nV/\sqrt{Hz}$.

Note that the noise quantities are quoted in terms of $pA/\sqrt{Hz}$ or $nV/\sqrt{Hz}$. To find the noise level in a given bandwidth B the quantities must be multiplied by $\sqrt{B}$. To find the noise power the quantity must be squared.

The noise due to the current source is determined by the parallel combination of the source impedance Z_s and the amplifier input impedance R_a. The relatively low source impedance of the hydrophones means that the voltage noise will dominate over the current noise, especially with the TL071 opamp used in the receiver. The level of current noise can be calculated as

$$e_i = i_n \left(Z_s \parallel R_a \right) \quad V/\sqrt{Hz} \qquad (3.8)$$

The other noise source is the Johnson (thermal) noise from the circuit resistors. The largest source of Johnson noise is from the input resistor R_a, and can be calculated as follows [33]

$$e_J = \sqrt{(4kTR_a)} \quad V/\sqrt{Hz} \qquad (3.9)$$

where k is Boltzmann's constant and T is the absolute temperature in degrees Kelvin.

The three noise sources are assumed to be uncorrelated, so that their power levels can be summed directly. The total rms noise level in a bandwidth B is then

$$e_T = \sqrt{B(e_n^2 + e_i^2 + e_J^2)} \qquad (3.10)$$

$$= \sqrt{4000[(1.8 \cdot 10^{-8})^2 + (2.6 \cdot 10^{-11})^2 + (4 \cdot 10^{-8})^2]}$$

$$= 2.8\,\mu V$$

Therefore the electronic noise contributed by the first amplifier stage is $2.8\,\mu V$ referred to the input. This figure does not include the noise added by the bandpass filter, which uses two more TL071 opamps. However, their contribution to the total noise figure of the amplifier will be less than the first stage because of its high gain [34]. The first stage has a gain of 200 (46 dB) while the overall gain of the amplifier is 1000 (60 dB).

With a gain of 60 dB the rms noise voltage at the amplifier output would be 2.8 mV. The additional filter stages will add to the total noise level at the output. A measurement of the circuit output gave a noise level of 6 mV rms.

4 The Underwater Testbed

4.1 Testbed Architecture

The primary experimental tool for the research is a custom designed acoustic testbed. The system consists of four AT compatible computers linked by a communications network, as shown in figure 4-1. One acts as the fileserver for the network while a second 80386-based machine acts as the control and data storage node. The other two are compact "little-board-AT" computers which control the transmit and receive circuitry.

The computer network is an ARCNET LAN which supports a data rate of 2.5 Mbps. The network carries the data from the receive node to the control node. The network is also used to exchange command messages between the control, receive and transmit nodes. The data transfer requirements of the network are analyzed in [35].

The transmit circuitry includes a gated sine wave generator with variable pulse length. The sine wave signal is passed through a 120 watt amplifier and fed to an acoustic projector.

The generator also produces a sampling clock and trigger which are synchronized with the carrier signal. The clock and trigger are used by the receiver for synchronous sampling. Instead of sending synchronization messages over the network a separate cable is used to transmit these signals. This arrangement ensures that the stringent sample timing will not be disrupted by network delays.
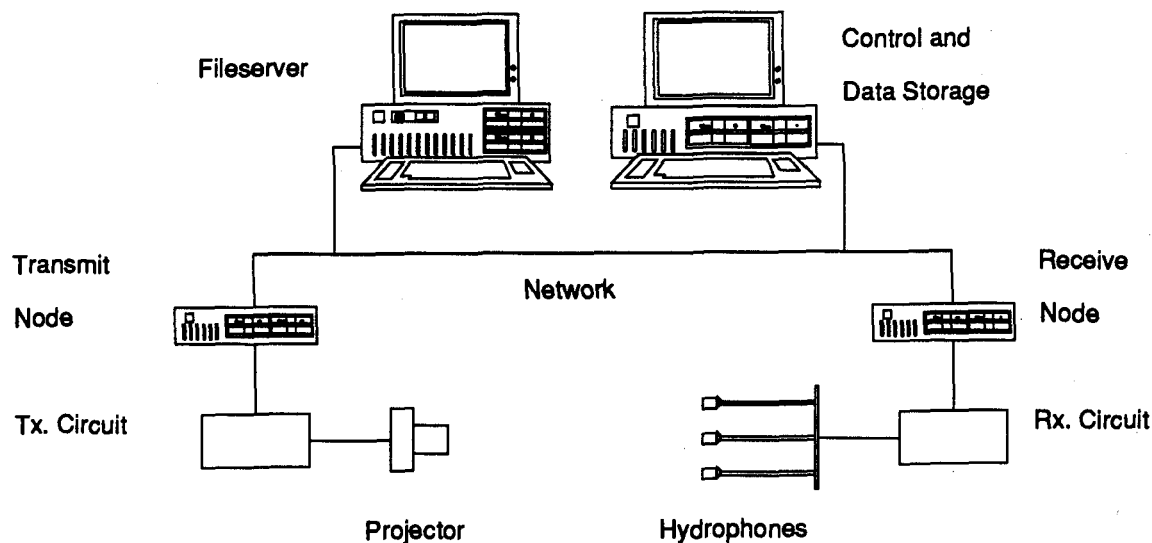
Figure 4-1 - The Acoustic Testbed

The signal is received by three hydrophones and then amplified and filtered by a 4 kHz wide bandpass filter. A 12 bit analog to digital converter then samples one or more of the three channels and transmits the digitized information to the control node. The receiver implements bandpass sampling, which both lowers the required sampling rate and allows the baseband signals to be recovered using purely digital processing. Further details of this technique are given in section 4.4.

4.2 Testbed Software

The control node runs the software which interfaces with the user. This program, called *Surface*, co-ordinates the transmission, reception and storage of the data. The program can also be used to retrieve and view previously saved data files.

Data collection is initiated by the user selecting the appropriate command from the program's main menu. There are several parameters which can be set, including; number of pulses to be sent, pulse repetition rate, length of receive buffer and number of channels to sample. The program can sample up to four A/D channels simultaneously.

Data can be collected in one of two modes: **Run** or **Graphics**. In **Run** mode a fixed number of pulses are sent and the received data is stored in a memory buffer. After all of the data is received it can be saved to a disk file and viewed on the screen.

In **Graphics** mode the data is received and displayed in real time on the screen. The waveforms for each pulse are displayed on top of the previous waveforms, allowing the user to see how the signals change with time. However, only data from the most recently received pulse is kept in memory.

Figure 4-2 depicts a typical screen display from *Surface*, showing the three different display formats for the signal. The top window is the complex baseband signal. The bottom left window is the actual received signal. The bottom right window shows the phase of the signal at each sample point.

The phase plot can be useful for looking at the phase stability or coherence of the signal. However, the format of the phase window in figure 4-2 is not convenient for this purpose because is shows the phase of all 160 sample points simultaneously. It is preferable to plot the phase of a single sample point in the received pulse and then observe how it changes in subsequent pulses. Figure 4-3 shows two examples of this display format.
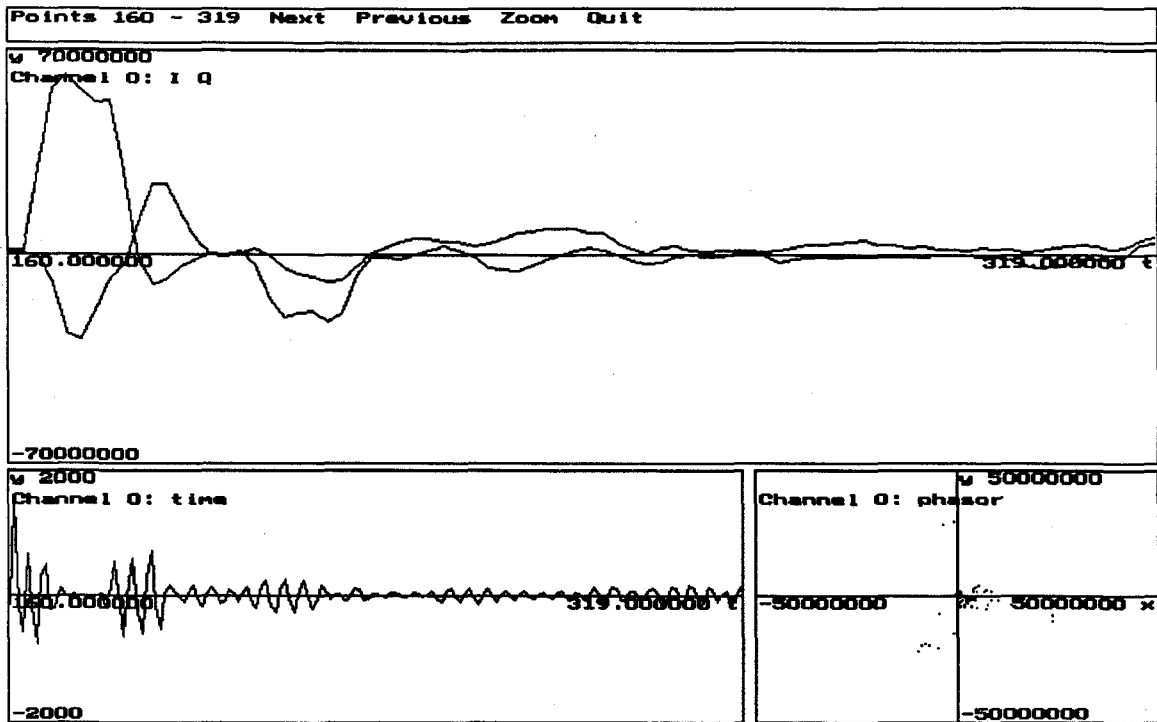
Figure 4-2 - Screen Display from Surface Program

Both plots shows the phase at a point in the middle of a direct arrival, with the transducers placed in an indoor test tank. Figure 4-3(a) shows the stable response which can be obtained when the transducers are motionless and there are no interfering signals. Figure 4-3(b) is an example of a less stable signal. This effect was created artificially by moving the projector vertically over a range of a few centimetres while several pulses were transmitted. The movement of the projector altered the path length between the projector and the hydrophone, and hence changed the phase of the received signal.
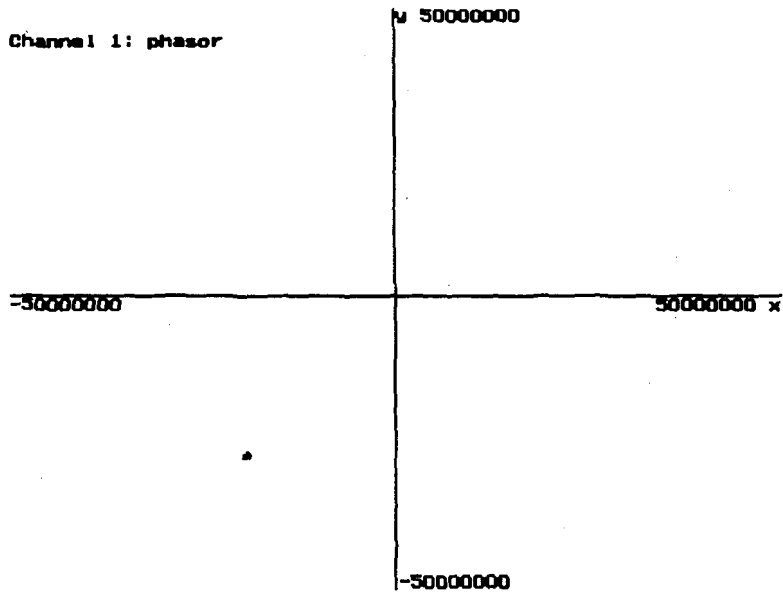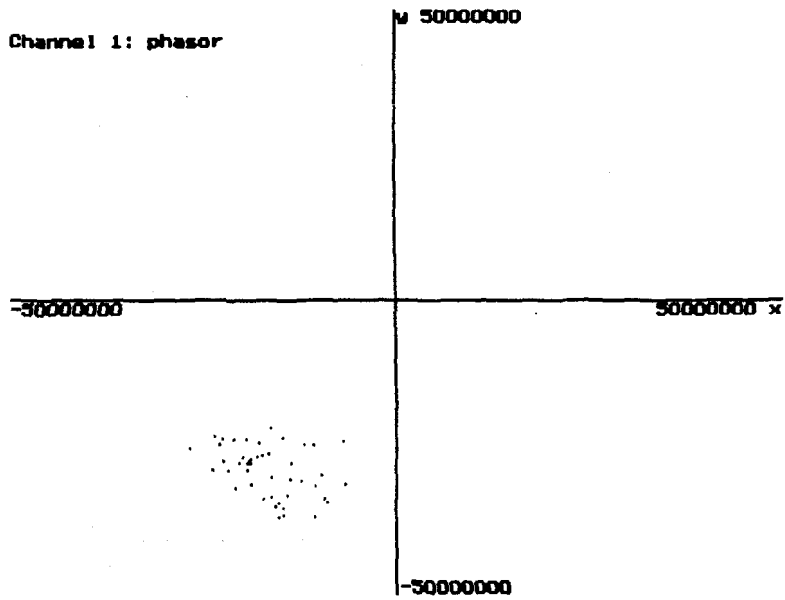
56

Channel 1: phasor

Figure 4-3(a) - Received Signal with Stable Response

Channel 1: phasor

4-3(b) - A Less Stable Received Signal

4.3 System Noise Analysis

It is important to be able to identify the sources of noise in a data gathering system, and to predict the noise and signal levels. For the underwater testbed, the two major sources of noise are ambient noise in the ocean and electronic noise from the receive amplifiers. The amplifier noise was discussed in section 3.5; the underwater ambient noise is dealt with next.

4.3.1 Underwater Ambient Noise

There are many mechanisms which produce underwater noise [36]. Below about 1 kHz shipping noise is the dominant source, while thermal noise becomes the largest source above about 50 kHz. At the operating frequency of 24 kHz the dominant source is wind-related Knudsen noise.

The wind noise is characterized by a set of data known as the Knudsen curves. These curves plot the noise levels as a function of frequency with wind speed as a parameter. The noise levels predicted by the Knudsen curves have been experimentally verified at many locations all over the world. One restriction on their application is that the water must be deep enough so that the surface waves do not break, causing higher noise levels.

The ambient noise level at 24 kHz is thus directly dependent on the prevailing wind speed, or equivalently, on the sea state. The test environment for this work was a marina in Burrard inlet (see section 5.1). The wind speed rarely exceeded a few knots. For the purpose of calculating the noise level we can therefore use the Knudsen curve for sea state 2, which corresponds to a wind speed of about 10 knots and a wave height of 1 to 3 feet.

The noise level L_s is given as 54 dB re 1 μPa/Hz, which is the noise level in a 1 Hz bandwidth relative to the standard level of 1 μPa. The level in a bandwidth β is given by

$$L \quad = \quad 10 \log \beta \quad + \quad L_s \tag{4.1}$$

With a bandwidth of 4 kHz the noise level is 90 dB re 1 μPa. The hydrophones have a sensitivity of -217 dB re 1V/μPa, which results in a noise signal level of only 0.45 μV at the amplifier input. Even at sea state 6 the level increases by only 10 dB, resulting in a signal level of 1.4 μV. However, it seems unlikely that much experimental work will be done with a sea state of 6 when the waves can reach heights of 20 feet!

4.3.2 Measured Noise Levels

As one might expect, the levels of ambient noise picked up by the hydrophones were too small to measure without amplification. Furthermore, a direct measurement would not be very useful because the observed noise level would reflect the amount of noise in the full bandwidth of the hydrophone. Instead the outputs of the receive amplifiers were observed, with the hydrophones in the water at the Burrard Inlet marina.

The calculations given in sections 3.5 and 4.3.1 predict that the output noise should be composed of mostly electronic noise from the amplifier, since the amplifier noise level (without the filters) is 2.8 μV versus 0.45 μV of ambient noise. With the amplifier gain at 60 dB the output noise level should therefore be about 3 mV rms. However, the measured levels were significantly higher at about 50 mV rms. The rms level was estimated by using the "rule of thumb" of dividing the peak to peak amplitude by 6 [37].

After some investigation it was found that the excess noise was due to a small residual signal being output from the transmit signal generator. The circuit uses a linear operational multiplier to gate the carrier with a square wave signal. The low logic level of the digital square wave is not exactly zero volts, resulting in a small leakage signal at the multiplier output. This signal then passes through the output amplifier and appears as noise. This noise source is seen to disappear when the transmitter is disconnected from the amplifier. The measured noise level then becomes 6 mV. This level is greater than the predicted 3 mV, but the discrepancy can be attributed to the noise contribution of the bandpass filter stage.

Although this stray signal is only present when the carrier is turned off, it still interferes with the transmitted pulses because of the multipath propagation. This problem will be eliminated when the transmitter is replaced with a more sophisticated signal generator, which is currently under development.

4.3.3 Measured Signal Levels

We shall consider the signal to noise ratio expected in two cases. The first is with the excess noise from the stray carrier signal and the second is without it. Because the excess noise originates from the projector, its level will vary in proportion to the desired signal as the distance from projector to hydrophone changes. In other words, the SNR should remain constant until the range is large enough that the electronic and ambient noise overtake the excess noise level.

The excess noise level at the amplifier output was measured at 50 mV rms at a range of 2.9 m. The signal level was 3.75 V rms, giving an SNR figure of 37.5 dB. The amplifier gain was set to 600, so the excess noise level was 83 μV referred to the amplifier input while the signal level was 6.25 mV.

Knowing the hydrophone sensitivity, we can convert these levels to the standard source levels expressed in dB relative to a reference level. This reference level is the intensity of a 1 watt source measured at a range of 1 m. Once expressed as dB quantities, the various levels become much easier to work with.

The hydrophone sensitivity is -216 dB re 1V/μPa. The signal level is -44.1 dB re 1V and the excess noise level is -81.6 dB. The intensity level of the signal is then just

$$L = -44.1\, dB - (-216\, dB) \tag{4.2}$$

$$= 171.9\, dB\ re\ 1\mu Pa$$

60

Similarly, the excess noise intensity is equal to 134.4 dB re 1μPa. These intensity levels can be converted to standard source levels by calculating the intensity at a range of 1 m

$$SL = L + 20 \log r \qquad (4.3)$$

where SL is the source level, L is intensity level, and r is the range in m. Since the measurements were taken at a range of 2.9m the source level of the signal is 181.2 dB re μPa @ 1m and the excess noise is 143.6 dB re μPa @ 1m. These source levels can easily be used to calculate the power radiated from the projector, assuming that it is a compact source. The relation between the source level and the power P in watts is

$$SL = 170.77 \, dB + 10 \log P \qquad (4.4)$$

The signal power radiated from the projector is thus 11 watts. The SNR will essentially remain constant at 37.5 dB so long as the excess noise is greater than the electronic noise. The equivalent intensity of the electronic noise would be 104.9 dB re 1μPa, which is 38.7 dB less than the excess noise at a range of 1 m. The two will be equal at a range of 86 m. At ranges greater than 86 m the SNR will be

$$SNR = 181.2 - 104.9 - 20 \log r \quad dB \qquad (4.5)$$

If the excess noise is eliminated, then this equation gives the SNR at any range r.

4.4 Recovering the Complex Baseband Signal

As mentioned earlier, the testbed uses the technique of quadrature bandpass sampling to sample the received signals. This technique offers two advantages over the straightforward Nyquist rate sampling. First, the sampling rate can be reduced significantly, thus allowing a slower and less expensive A/D board to be used. Alternatively, the slower sampling rate enables one to sample more channels simultaneously.

For example, the testbed uses a 100 kHz A/D board. With a 24 kHz carrier and a bandwidth of 4 kHz the Nyquist rate would be a minimum of 52 kHz. Allowing for a guard band would mean that only one channel at a time could be sampled. Using bandpass sampling, the testbed is able to sample 4 channels simultaneously. This feature is important for comparing the signals received at multiple hydrophones. Moreover, it is essential for implementing a digital beamformer.

The second advantage of the quadrature sampling is that the complex baseband signals can be recovered from the sampled data by digital processing. A conventional coherent receiver can recover a complex baseband signal through the use of two balanced mixers and low pass filters. There are several reasons why one might want to replace this conventional approach with a digital demodulator. For example, non-ideal characteristics of analog circuit components can limit system performance considerably.

For this project, we needed to be able to sample the bandpass signal directly and log the data for analysis at a later time. Bandpass sampling provides a simple and accurate way of recovering the desired baseband information. A brief explanation of the sampling requirements is given next. For full details the reader should refer to [38].

4.4.1 Bandpass Sampling

Assume that we have a bandpass signal with a bandwidth ω_{BS} and a center frequency ω_O, as shown in figure 4-4. We define a larger bandwidth ω_B which includes ω_{BS}, such that the highest frequency in the band is ω_H. The reason for using a larger bandwidth is that for bandpass sampling with no spectral overlaps we must have

$$\frac{\omega_H}{\omega_B} = k \qquad\qquad (4.6)$$

where k is an integer. If the signal is sampled at a rate $\omega_S = 2\omega_B$ the resulting folded spectrum is as shown in figure 4-5. Note that there is no overlap of the spectral images. The baseband signal can therefore be recovered without aliasing. Multiplying the sampled signal by $\exp\left\{j\frac{\omega_B}{2}t\right\}$ will shift the spectrum so that the spectral image centered at $\omega = \frac{\omega_B}{2}$ will move to $\omega = 0$, i.e. a complex lowpass representation of the original bandpass signal.

An expression for the required sampling frequency ω_S given ω_B, ω_O and k can be found as follows:

$$\omega_H = \omega_O + \frac{\omega_B}{2} \quad\text{and}\quad \omega_H = k\omega_B \qquad\qquad (4.7)$$

$$\therefore \quad \omega_B = \frac{2\omega_O}{2k-1} \qquad\qquad (4.8)$$

and since $\quad \omega_S = 2\omega_B$

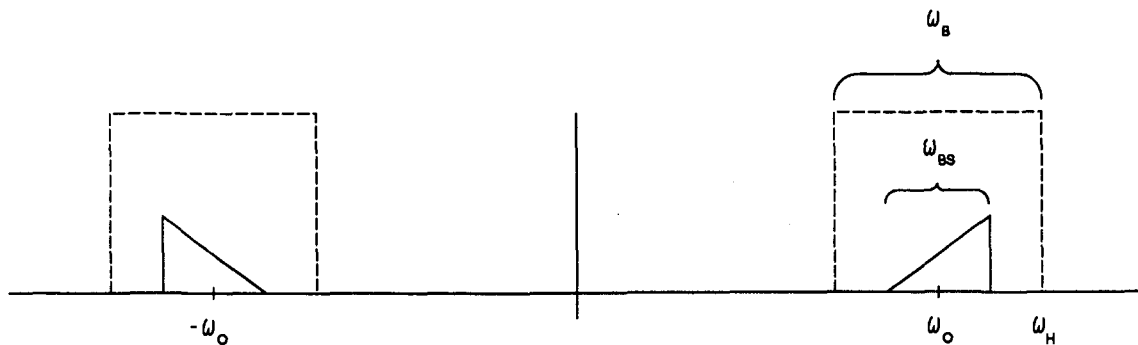$$\omega_S = \frac{4\omega_O}{2k-1} \qquad\qquad (4.9)$$
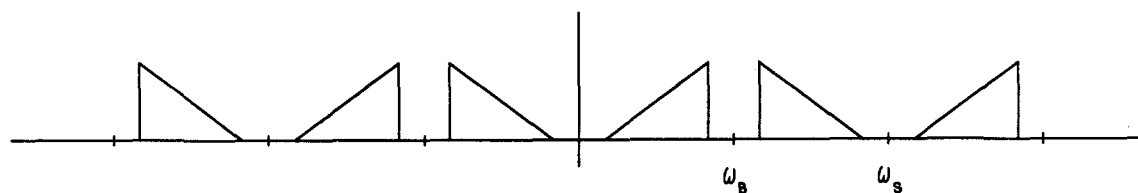
Figure 4-4 - A complex bandpass signal

Figure 4-5 - A bandpass signal after sampling

The testbed sampling frequency is determined by a dip switch in the transmit node signal generator. The sample rate can be set from a maximum of 4/3 to a minimum of 4/15 of the carrier frequency. In other words, the term k in the above equation can be varied from 2 up to 8.

5 Experimental Data

5.1 Test Environment

The experimental work for this thesis was done at three different sites over a period of about six months, starting in September of 1989 when the testbed was first fully functional. The first two sites were located in Burrard Inlet, a large salt water inlet in Vancouver. The third location was an indoor test tank at the facilities of the Underwater Research Lab at Simon Fraser University.

The first sets of data were taken from a barge moored in a marina in Burrard Inlet. The barge was owned by Simrad-Mesotech Ltd., and was used for testing their sonar equipment. The barge was a floating platform roughly 15 m by 5 m, with a small portable office placed in the middle. The average water depth was 12 m, with a tidal fluctuation of about plus or minus 2 m.

The second location is another barge moored close to the first site. Though smaller than the first barge, the second one allows all of the work to be done indoors. The transducers are lowered from holes inside the barge. The main difference is that surface reflections bounce off a water - air boundary at the first site, but off the bottom of the barge at the second.

The experimental setup for the acoustic measurements is illustrated in figure 5-1. The computers and electronics were kept inside the barge while the transducers were lowered into the water. For all of the data presented in this thesis the transducers were oriented vertically, as shown in the diagram.
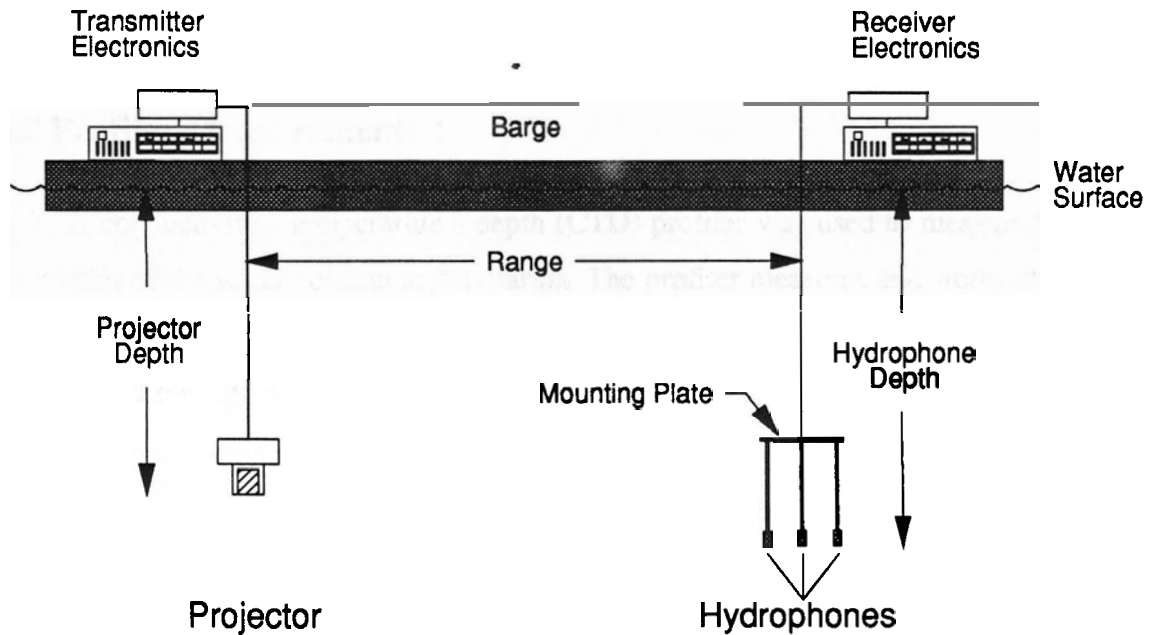

Figure 5-1 - Experimental Setup for Acoustic Measurements

The third location is a test tank, measuring 4 m by 4 m by 1.5 m deep. The tank is located indoors, and is part of the facilities of the Underwater Research Lab at Simon Fraser University. It is filled with fresh water at room temperature.

The tank is useful for testing the operation of the underwater testbed, as well as other underwater equipment. It can also be used for measuring transducer characteristics. The main drawback of the tank versus an open water facility is the reverberation. In order to take meaningful measurements it is usually necessary to use a pulsed signal and look at the initial returns before the onset of reverberation.

The length of time before the first reflected signal is determined by the dimensions of the tank. For this reason a larger tank is preferable over a smaller one. However, one can effectively scale the useful pulse length by operating at a higher frequency. For example, with our tank the maximum delay between a direct arrival and the first reflected signal is 1 ms (1.5 m divided by the sound speed of 1500 m/s). At 24 kHz this corresponds to 24 cycles of the carrier, but at 100 kHz it would be 100 cycles.

5.2 Profiler Measurements

A conductivity - temperature - depth (CTD) profiler was used to measure the characteristics of the water column at the marina. The profiler measures and stores data of the three measurements as it is lowered or raised through the water. The information can later be retrieved through an RS232 communications link.

The data is recorded as depth (in metres), temperature (in degrees Celsius) and salinity (in parts per thousand). These three values can then be used to estimate the sound speed using an equation such as 5.1 below [39]

$$c = 1449 + 4.6T - 0.055T^2 + 0.0003T^3 + (1.39 - 0.012T)(S - 35) + 0.017z \qquad (5.1)$$

where c is the sound speed in m/s, T is the temperature in °C, S is the salinity in p.p.t. and z is the depth in m.

The graphs in figures 5-2, 5-3 and 5-4 show the temperature, salinity and calculated sound speed, respectively, as a function of depth. The measurements were taken from the barge in April 1989. The multiple lines in each graph show different sets of data as the CTD profiler was repeatedly lowered and then raised through the water column.

The sound speed profile in figure 5-4 shows that there is a negative sound speed gradient, meaning that the sound speed decreases with increasing depth. The possible effects of such a gradient are discussed in section 6.2. Comparing figures 5-2 and 5-4, we can see the strong correlation between sound speed and water temperature. This relationship is also evident from equation 5.1.

The graphs also show that there is a slight positive sound speed gradient near the surface. Figure 5-2 shows that there is a layer of cooler water near the surface. Figure 5-3 indicates that there must be a layer of fresh water at the surface because the salinity increases with depth. This cooler fresh water layer could be from spring runoff, rain water, or a combination of the two.

Figure 5-5 shows the sound speed profile for the same location, but recorded six months later, in October. Again there is a negative sound speed gradient, with the largest change occurring between the depths of 2 m and 3 m. The slight positive gradient near the surface is no longer present, perhaps indicating that the fresh water layer had mixed with the water below.

5.3 Direct and Multipath Returns

Figure 5-6 shows some typical data obtained with the testbed. The graphs show the direct arrival and multipath returns at the receiver. The vertical scale running from -2048 to 2048 represents the full range of the 12 bit ADC.
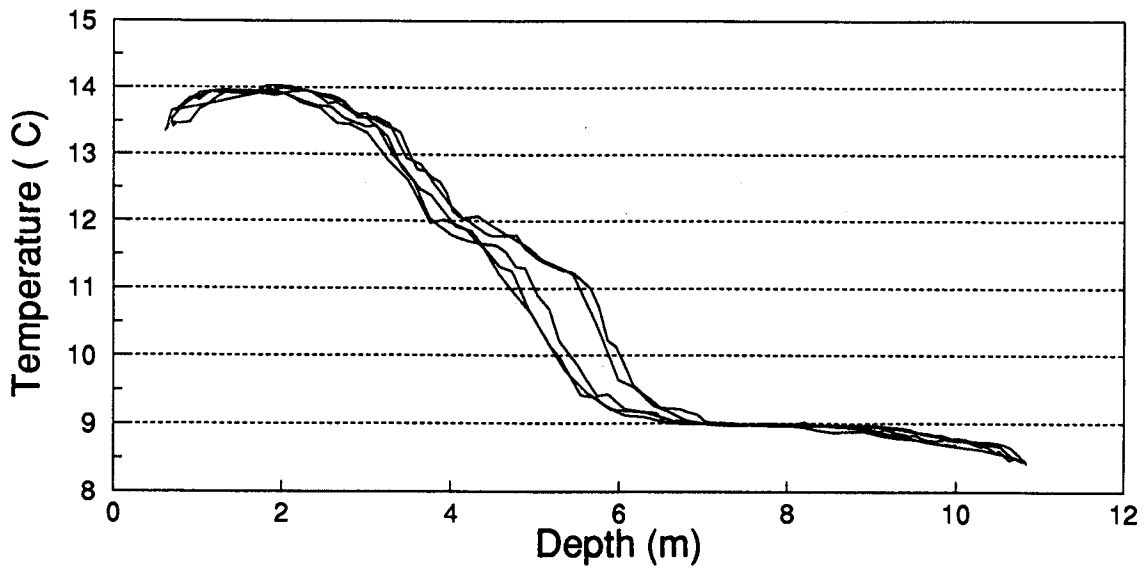
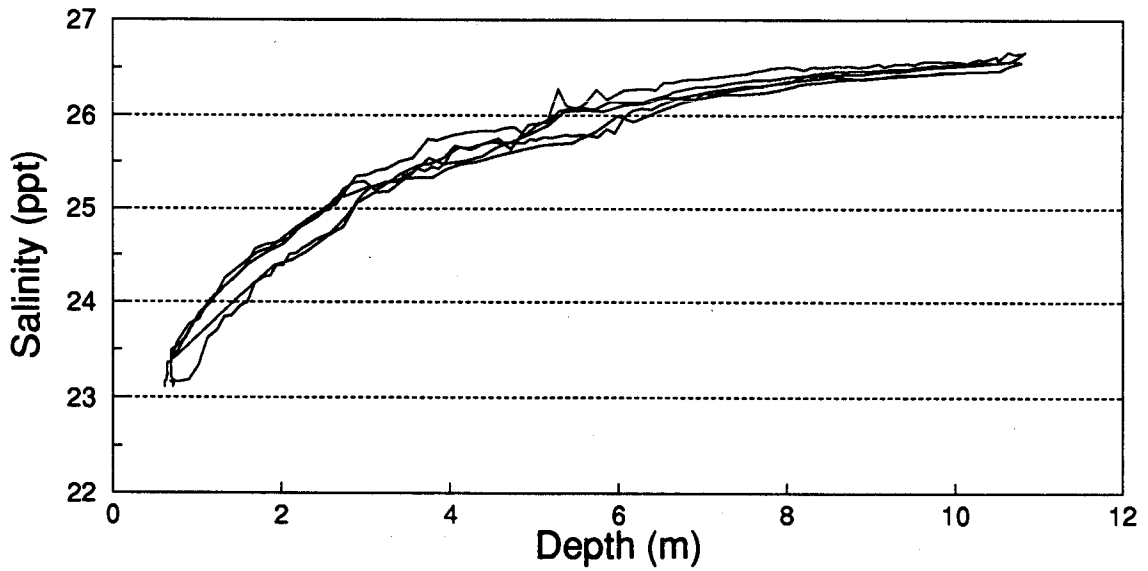Figure 5-2 - Temperature vs. Depth (April 1989)

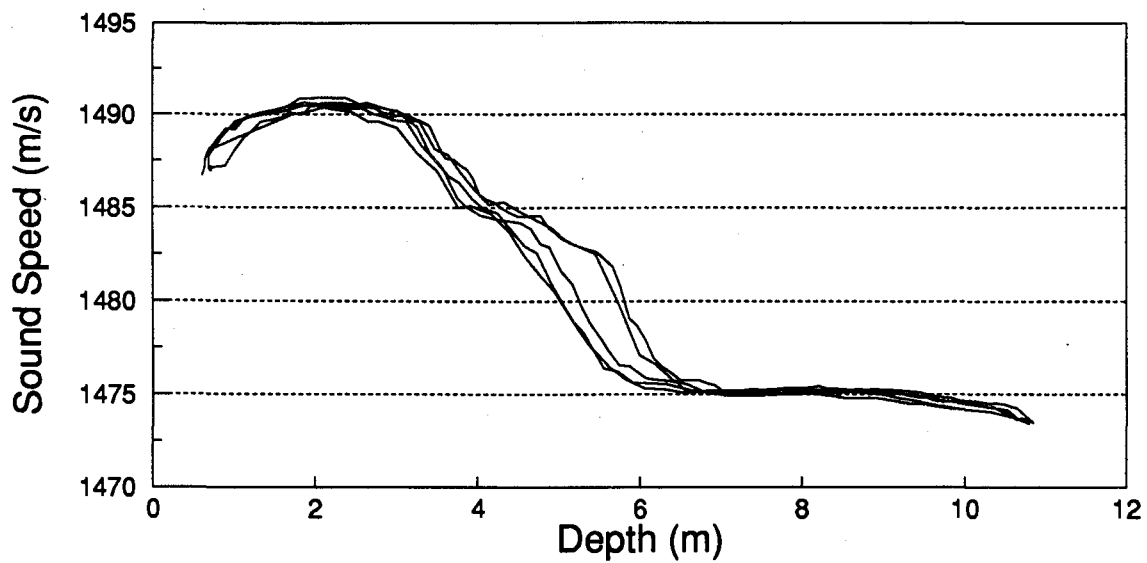Figure 5-3 - Salinity vs. Depth (April 1989)

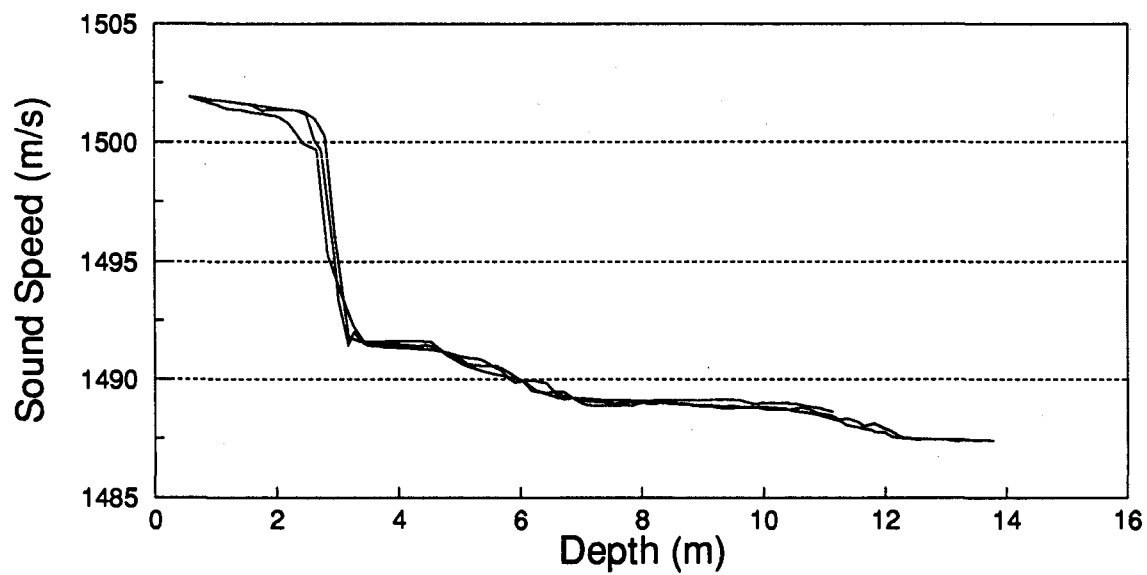Figure 5-4 - Sound Speed vs. Depth (April 1989)

Figure 5-5 - Sound Speed vs. Depth (October 1989)

Note that while these are time domain plots they do not show the actual received waveform, but rather the subsampled version. All of the data presented in this thesis was sampled at a rate of 4/5 of the carrier frequency, which is a sampling rate of 19.2 KHz.

One effect of the subsampling is that the time plots will not necessarily show the full amplitude of the waveforms. The peak values will depend upon the phase of the received signal, which will determine the sample points on the received waveform. However, the recovered baseband signals, discussed in the next section, will show the proper amplitudes of the I and Q channels. Another effect is that the time graphs show fewer carrier cycles per pulse. For example, in figure 5-6(a) the transmitted pulse has a length of 16 cycles of the carrier, while the graph shows only seven.

This data was recorded with the projector and hydrophone separated by 12 m in water that was 12 m deep. In 5-6(a) both transducers were at a depth of 4 m; in figure 5-6(b) they had been lowered to a depth of 5 m. In both cases the first return is the direct pulse. The second return is a surface bounce, followed by other reflections from the barge and the bottom. As expected, figure 5-6(b) shows that the surface return becomes further separated in time from the direct when the transducers are lowered.

One unexpected result is that the surface reflected pulse increased in amplitude while the direct decreased. It is possible that the subsampling can give an incorrect measure of the amplitude, as mentioned earlier. However, the true energy in the signal can be determined from the magnitudes of the I-channel and Q-channel components of the baseband signals. The baseband plots shown in figures 5-7(a) and 5-7(b) show that the energy in the direct signal decreased while the reflected signal increased when the receiver was lowered.

One would expect that the direct arrival would remain constant while the surface bounce would decrease in amplitude as the depth increased. Furthermore, this result was not an isolated example. The effect persisted over several tens of seconds as multiple pulses were transmitted and recorded. Further anomalies in the received data are presented in section 5.4.
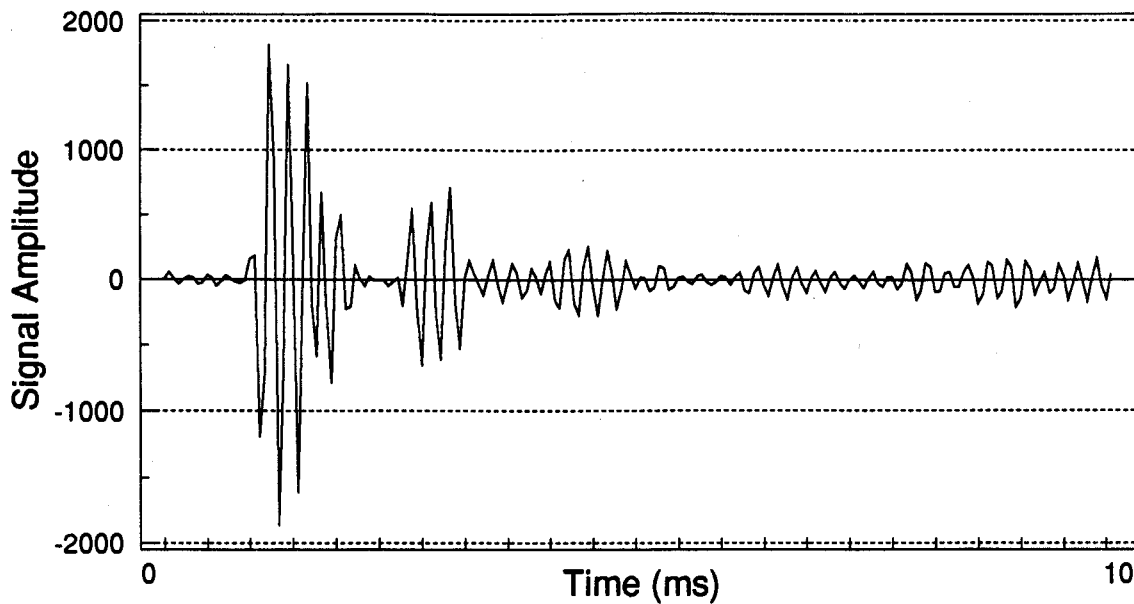
71

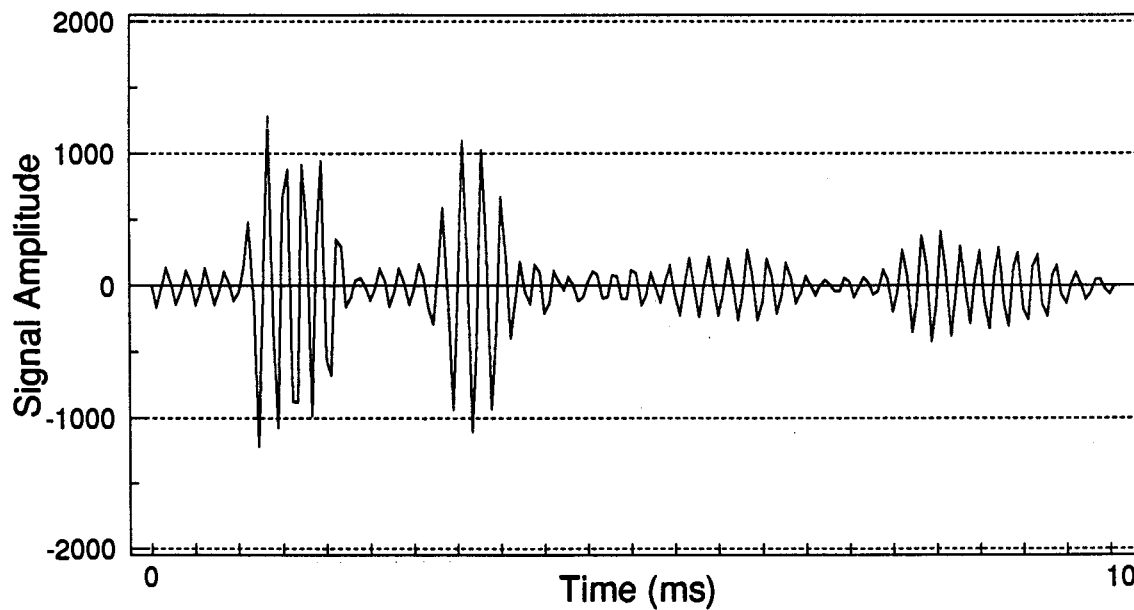Figure 5-6(a) - Received Signal with Tx. and Rx. at 4m Depth

Figure 5-6(b) - Received Signal with Tx. at 4m and Rx. at 5m

The acoustic returns were found to be very stable over periods up to several minutes. The direct returns and the bottom bounces would remain essentially unchanged until one of the transducers was moved. The surface reflections were also surprisingly stable, provided that the water was calm (sea state 0).

5.4 Complex Baseband Response

The signals shown in figure 5-6 are sampled at a rate less than twice the signal frequency. However, by proper selection of the sampling frequency it is possible to ensure that the baseband signals can be recovered without aliasing. Figures 5-7(a) and 5-7(b) show the complex baseband signals corresponding to figures 5-6(a) and 5-6(b) respectively.

Because the transmitted pulse is obtained by gating the carrier, the baseband equivalent is simply a square pulse. The relative magnitudes of the in-phase and quadrature components depend upon the phase of the signal. The direct and surface bounce arrivals are easy to identify. An important feature to note is the pulse shape of the direct arrivals. Ideally they should be square pulses; instead there is a significant amount of distortion.

A set of returns recorded in the indoor test tank is plotted in figure 5-8. The projector and hydrophone were both at a depth of 0.75 m in the 1.5 m deep tank. With a separation of 0.4 m, the surface and bottom reflections arrived 0.87 ms after the direct signal. The pulse length was 32 cycles at 24 kHz, or 1.33 ms. Therefore there was interference in the second half of the direct arrival.

These arrival times are not obvious in the time plot of figure 5-8(a). It actually appears that the direct arrival lasted for about 2 ms and suffered no interference. However, the baseband plot in 5-8(b) reveals the large phase shift at about 0.9 ms, indicating interference. Note that it is difficult to observe the signal distortion seen in the previous data because the reflected signals arrived too soon after the direct.

Figure 5-9 shows the time and baseband signals for another set of returns from the barge. Here the distortion is again visible; it is even more noticeable than in figure 5-6 and is present in both the direct and surface returns. Small transients in the signal due to the band limiting effects of the projector and the receive filters were predicted. However, the level of distortion exhibited here is much greater than expected and could cause serious problems in a communications system.

Subsequent experiments over several days showed that this effect was persistent. Initial attempts to find an obvious source for the distortion were unsuccessful. Furthermore, no references to anything similar could be found in the literature. Part of the problem was that no one had previously presented data on the exact nature of coherently received baseband signals.

However, there is some data on previous work which had similar goals. International Submarine Technology (IST) researched and developed a telemetry system for use with the ARCS (Autonomous Remote Controlled Submersible) vehicle developed by International Submarine Engineering (ISE). This untethered vehicle was designed to operate under Arctic ice. In order to develop the telemetry system, IST conducted some experiments in the Arctic to evaluate the underwater channel [2].

The focus of the work was a study of the multipath structure. Acoustic pulses were transmitted over distances ranging from 30 m up to 4500 m in depths ranging from 10 m to 100 m. The researchers observed consistent multipath returns from both the ice covered surface and the bottom. With the larger separations the first multipath returns interfered with the direct arrivals. However, the paper does not mention any experiments done at closer range to verify that the source of interference was the multipath propagation. In fact, the authors only state that "the geometry of the propagation channel would probably explain the consistent pattern".

It is certain, however, that the interference displayed in figures 5-7 and 5-9 is not due to reflections from the surface or bottom. The receiver and transmitter were close enough so that the direct pulse was separate from the reflections. Therefore, there must be some other mechanism which distorts the signal. The next section describes the investigation of some possible explanations.
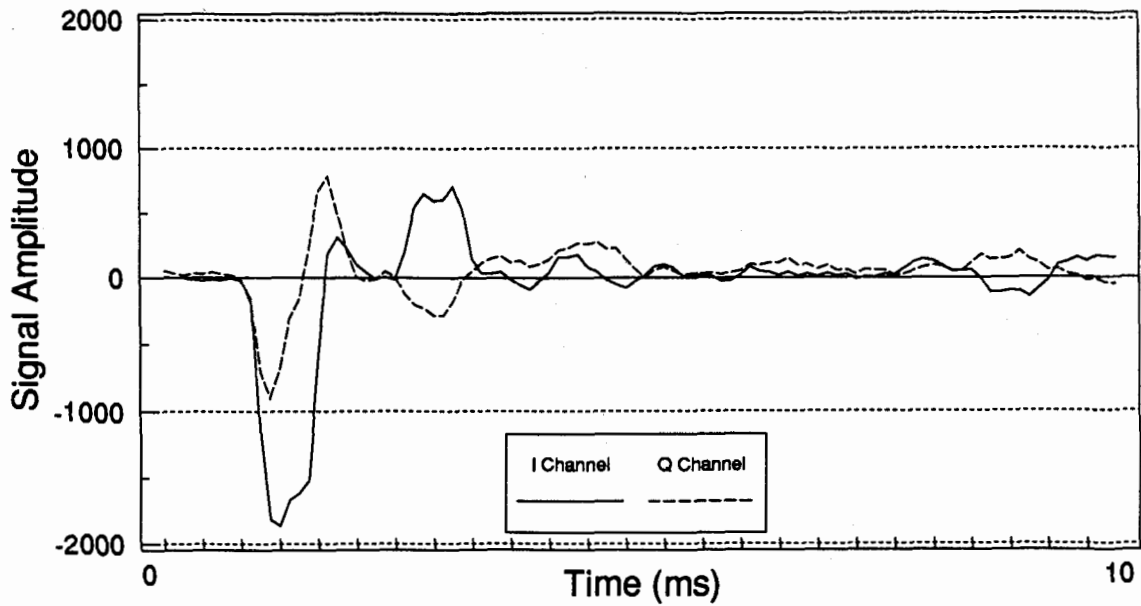
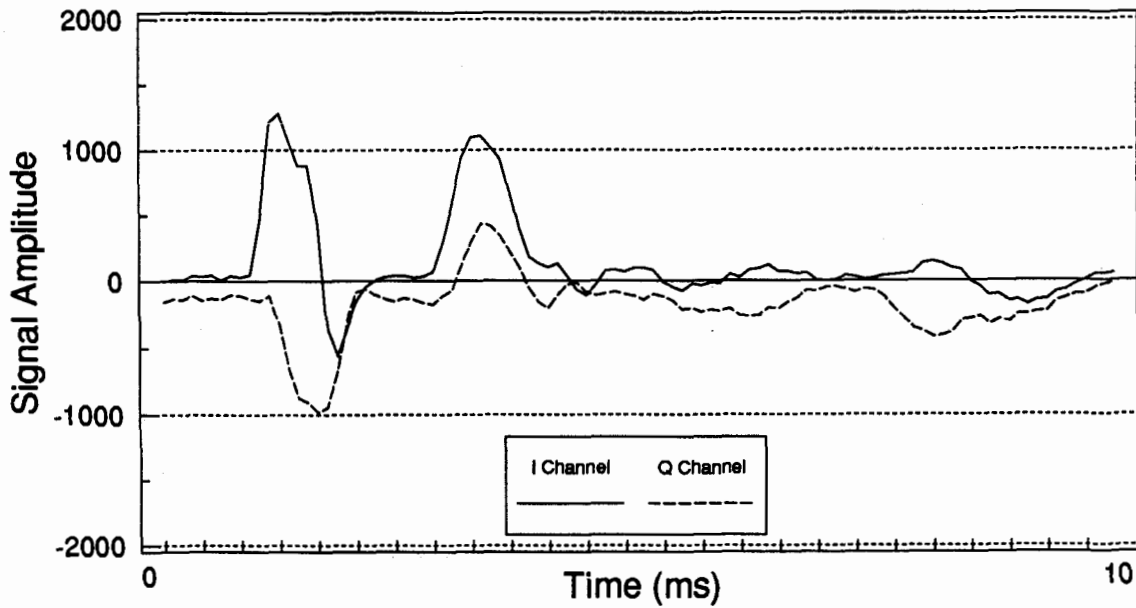Figure 5-7(a) - Received Complex Baseband with Tx. and Rx. at 4m

Figure 5-7(b) - Received Complex Baseband with Tx. at 4m and Rx. at 5m

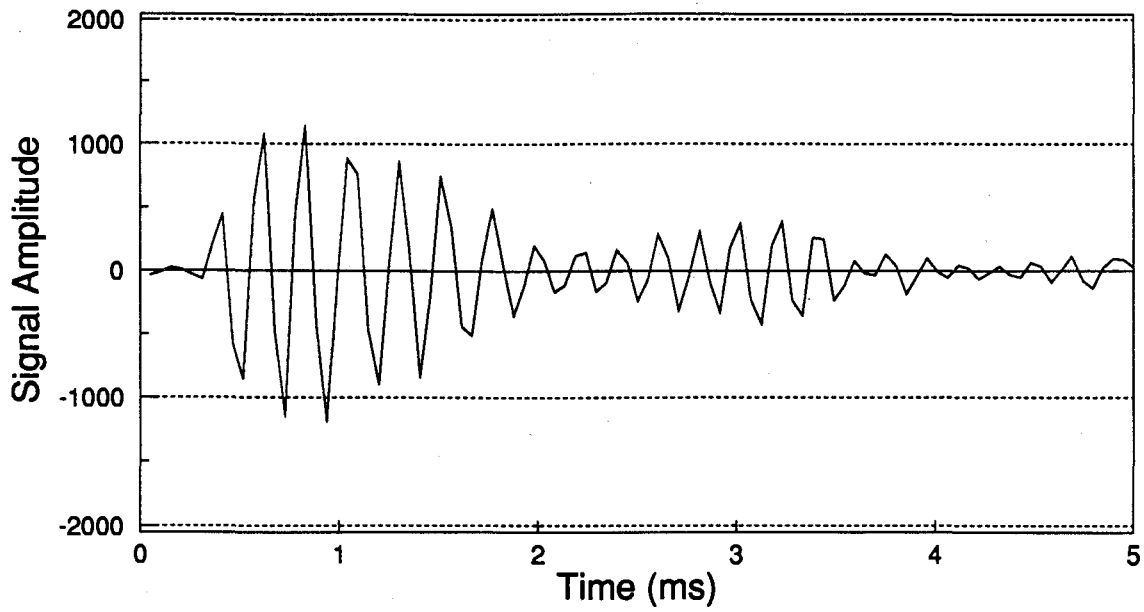76

Figure 5-8(a) - Received Signal in the Test Tank
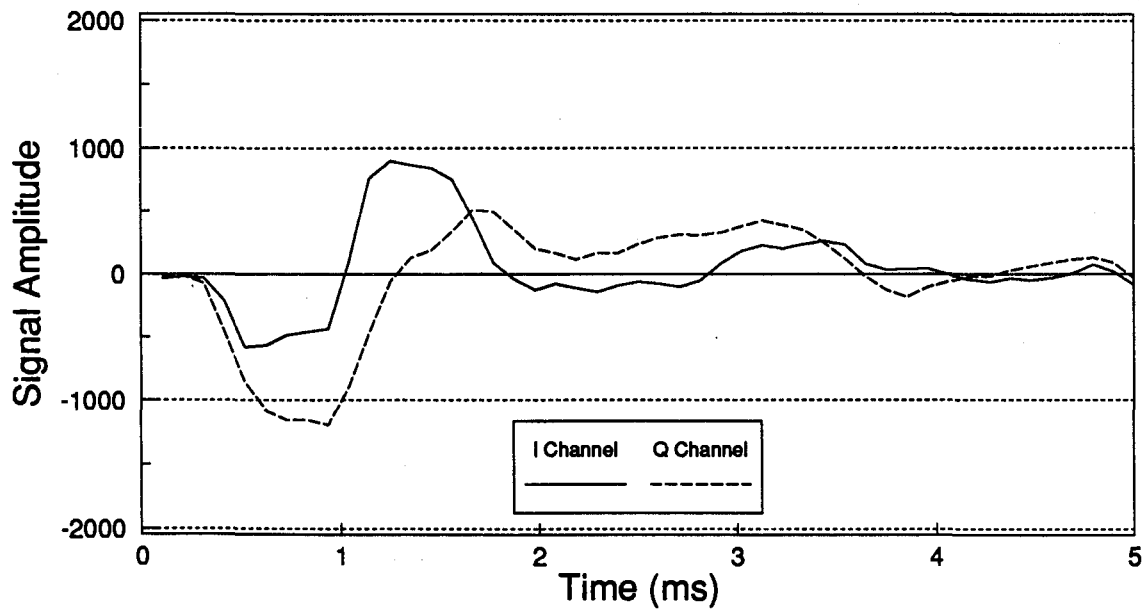

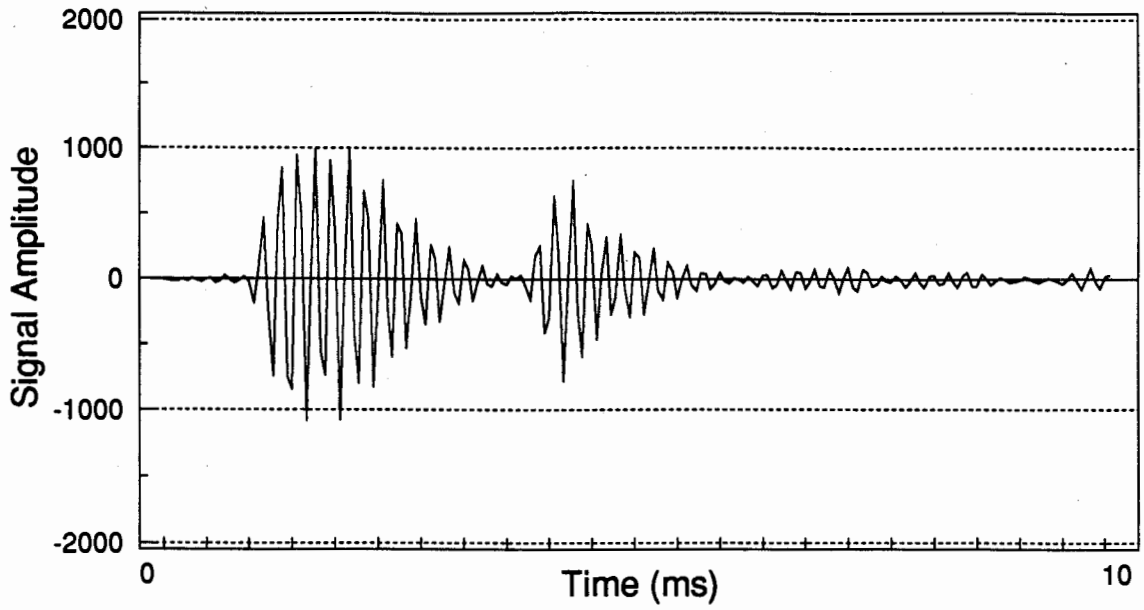Figure 5-8(b) - Received Complex Baseband Signal in the Test Tank
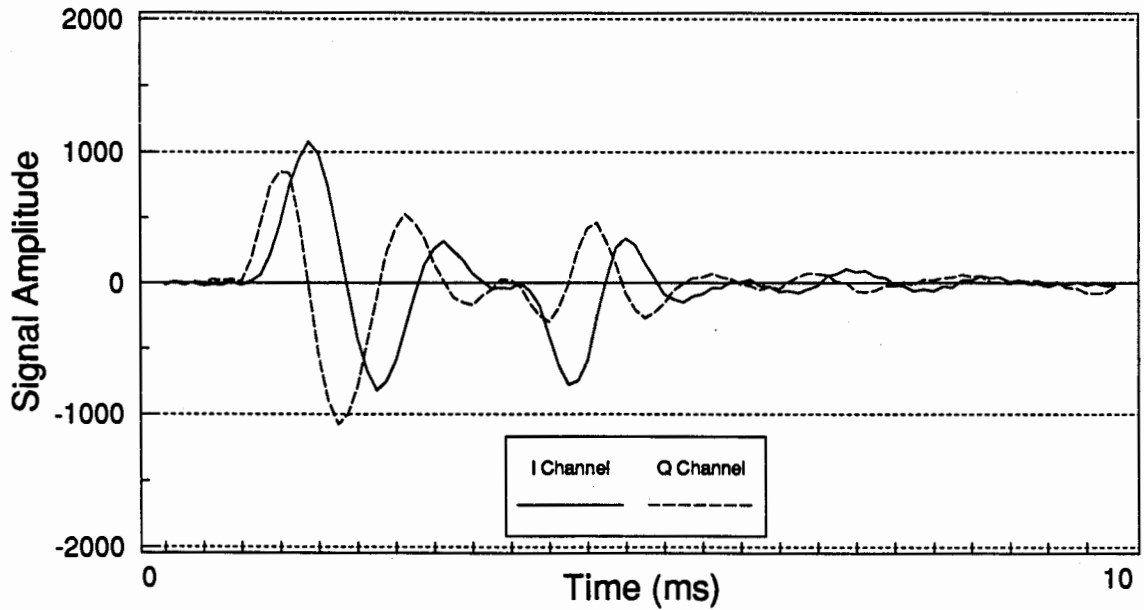
77

Figure 5-9(a) - Received Signal with Large Distortion

Figure 5-9(b) - Complex Baseband Equivalent of Figure 5-9(a)

78

6 Analysis of the Channel Behaviour

6.1 Frequency Offsets

It might seem obvious from figure 5-8(b) that the observed distortion could be explained by a frequency offset somewhere in the system. Specifically, the baseband signal appears to have a sinusoidal component; ideally, the demodulated signal should be square wave in both the I and Q channel. The offset could come from one or more sources, such as a shift in the carrier frequency due to a Doppler shift, or perhaps a change in the oscillator frequency. However, if the oscillator drifts we are guaranteed to have the correct sampling rate since the ADC clock is derived directly from the transmit oscillator.

A Doppler shift would cause the received baseband signal to have a non-zero frequency component. The apparent oscillation frequency of the baseband signal in figure 5-8(b) is about 800 Hz. The relative velocity required to produce a Doppler shift of 800 Hz is 50 m/s! Since both the receiver and transmitter were stationary we can rule out this possibility.

Another source of a frequency offset would be a nonsymmetric frequency response of one of the channel elements. For example, if the center frequency of the projector was not at 24 kHz then the baseband response would have a sinusoidal component. It is possible to investigate the effects of a frequency offset with some straightforward analysis. Employing Laplace transforms, we shall consider the case where the carrier frequency is offset from the resonant frequency of the projector.

Section 3.1 gives the details of the projector response, and figure 3-2 shows the equivalent circuit model. The resonance of the projector can be modelled as a second order LCR system, while the input is a gated sinusoid. The derivation of the time domain response is given in appendix A. The resulting baseband In-phase and Quadrature signals output from the projector are

$$h_I(t) = c_3 + e^{-\zeta \omega_o t}(c_1 \cos \Delta \omega t + c_2 \sin \Delta \omega t) \qquad (6.1)$$

$$h_Q(t) = c_4 + e^{-\zeta \omega_o t}(c_1 \sin \Delta \omega t + c_2 \cos \Delta \omega t) \qquad (6.2)$$

where ω_o is the resonant frequency of the projector, $\Delta \omega$ is the frequency offset between the carrier signal and the resonant frequency, and ζ is the damping factor, equal to $1/2Q$. The definitions of the coefficients c_1 through c_4 are given in the appendix.

The response in both channels is composed of a constant steady state plus an exponentially damped sinusoid. When there is no frequency offset both c_1 and c_3 are zero, meaning that the steady state response would be non-zero only in the Q channel, which is the expected output for a sine wave input.

Figure 6-1 shows the response, calculated using equations 6.1 and 6.2, when $\omega_o = 24\,kHz$, $\Delta \omega = 0$ and $\zeta = 0.025$. The result is a clean signal with a smooth transient. The rise time depends upon the Q of the projector; a smaller Q means a larger damping factor and hence a slower rise time.

We are interested in the effect of a non zero frequency offset on the response. Figure 6-2 shows the resulting signal when there is an offset of 3 kHz, with all other conditions remaining the same. The calculated response is similar to those recorded with the testbed (shown in section 5.4).

However, the response given in equations 6.1 and 6.2 is the output of the projector. If we want to predict the shape of the signal received at the hydrophone then we must take into account the propagation delay from transmitter to receiver. A delay of τ seconds will cause a phase rotation, resulting in the following received baseband signals.

$$I(t) = p_I(t)\cos\alpha\tau \quad - \quad p_Q(t)\sin\alpha\tau \qquad (6.3)$$

$$Q(t) = p_I(t)\sin\alpha\tau \quad + \quad p_Q(t)\cos\alpha\tau \qquad (6.4)$$

Therefore, even when the frequency offset is zero the received signal may have non-zero steady state signals in both the I and Q channels. Figure 6-3 shows the effect of adding a delay corresponding to a phase rotation of $\frac{2}{5}\pi$. All other parameters are the same as in figure 6-2.

Figures 6-2 and 6-3 show that a frequency offset can cause distortion similar to the observed effect. However, those responses were calculated using the values $\Delta\omega = 3\,kHz$ and $Q = 20$. If either the frequency offset or the Q of the projector is decreased then the magnitude of the transient portion is diminished. Figure 6-4 shows the calculated response using the experimentally measured Q value of 3.

It is evident that with a Q value of 3 the projector will not produce a large transient response with a 3 kHz offset. So far we have only considered a nonsymmetric projector response; it is also possible that the receive filters may cause the transient effect. Rather than analytically calculating a new system response that includes the fourth order receive filters, the response was obtained numerically.
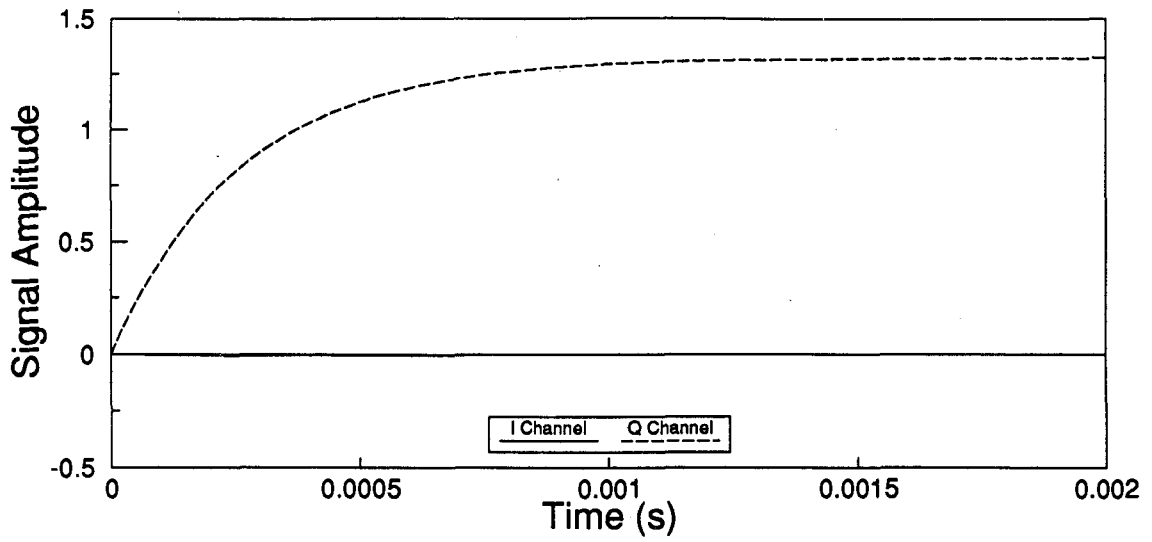
81

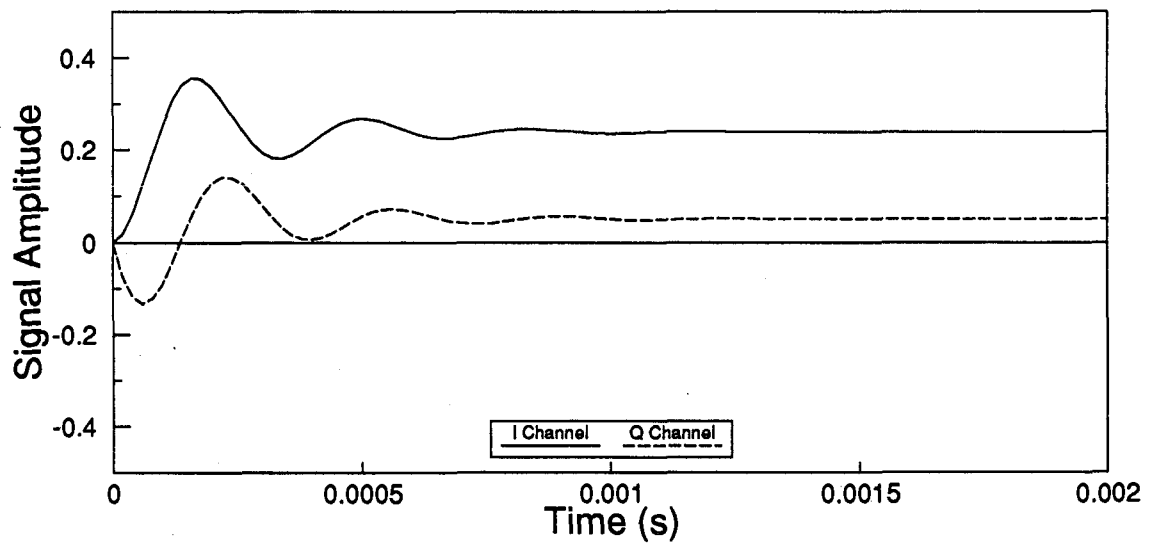Figure 6-1 - Projector Response (no frequency offset)

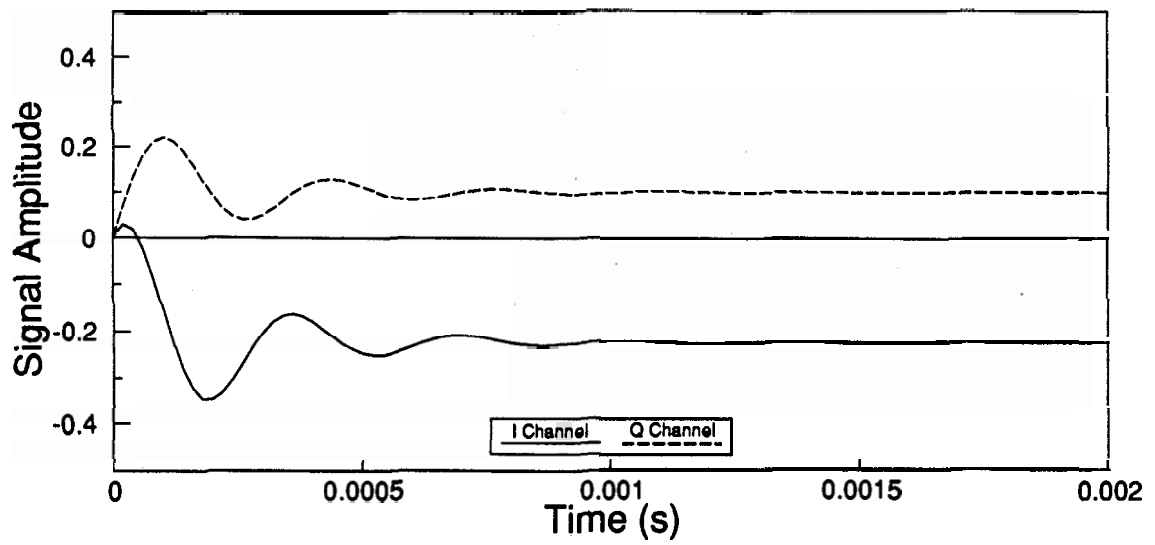Figure 6-2 - Projector Response (3 kHz offset)
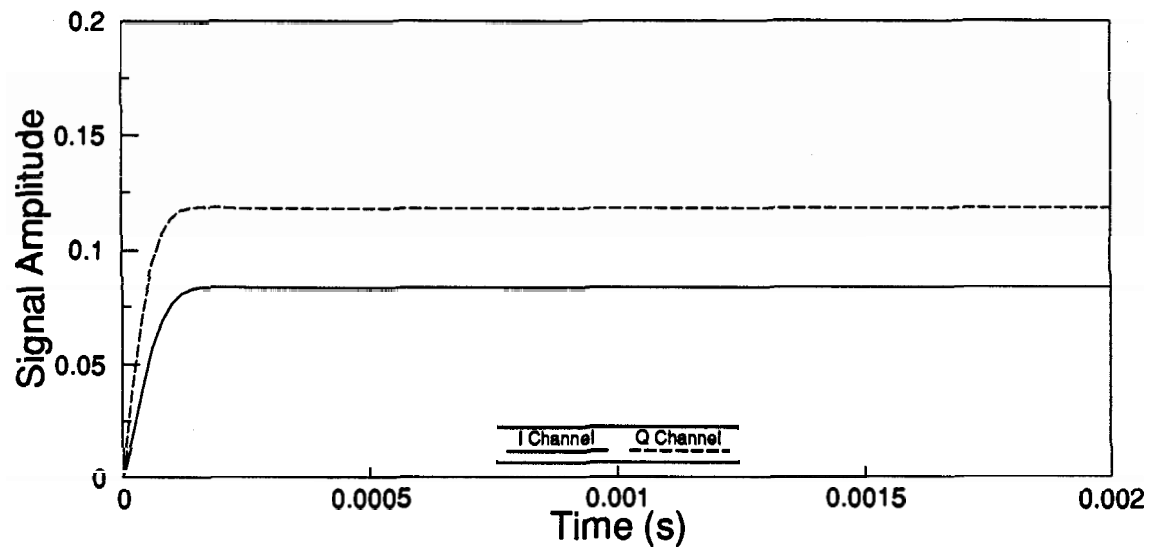
82

Figure 6-3 - Projector Response (with delay)

Figure 6-4 - Projector Response (Q = 3)

83

Using the measured frequency responses of the projector and filters (shown in section 3), the received signal was found using FFT analysis. First the system frequency response was found by multiplying the projector and filter responses. Simple linear interpolation was used to sample the frequency response at 512 points over the range of 12 kHz to 36 kHz. Next the input signal was generated by taking the FFT of a square pulse. The pulse had a length of 1 ms so that the main lobe of the signal was 2 kHz wide.

Figure 6-5 plots the system frequency response and the input signal's FFT. Note that the frequencies are shifted so that the 24 kHz center frequency is now at 0. The inverse FFT of the product gives the baseband response of the system, as plotted in figure 6-6.

The calculated baseband signal indicates that the combined effect of the projector and receive filter is insufficient to cause the observed distortion. The additional effect of shifting the input signal from 24 kHz up to 27 kHz does not produce any significant change from figure 6-6. We can therefore conclude that a frequency offset is not the source of the problem.
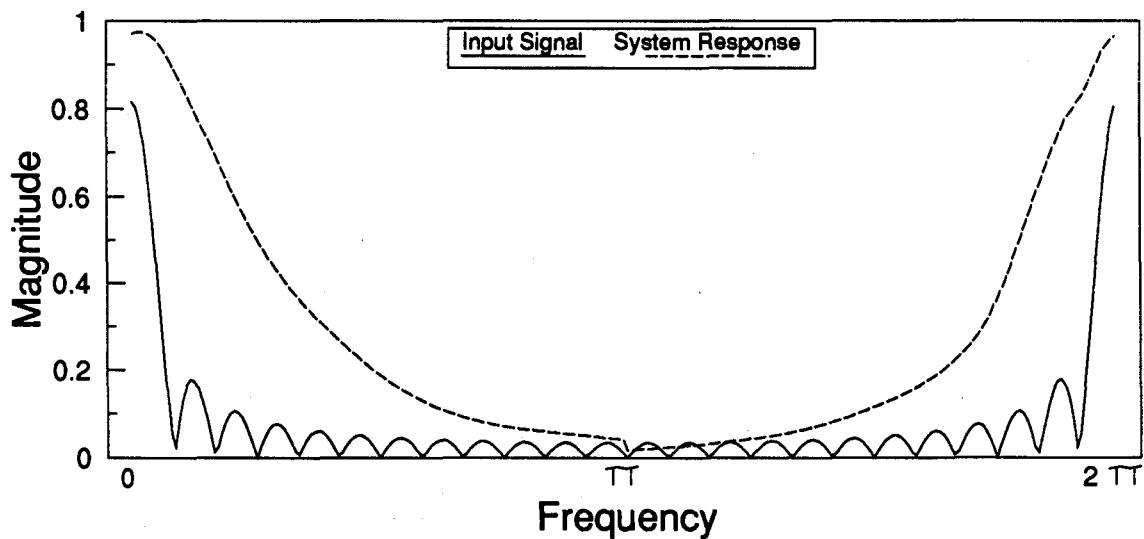

Figure 6-5 - System Frequency Response and Input Signal
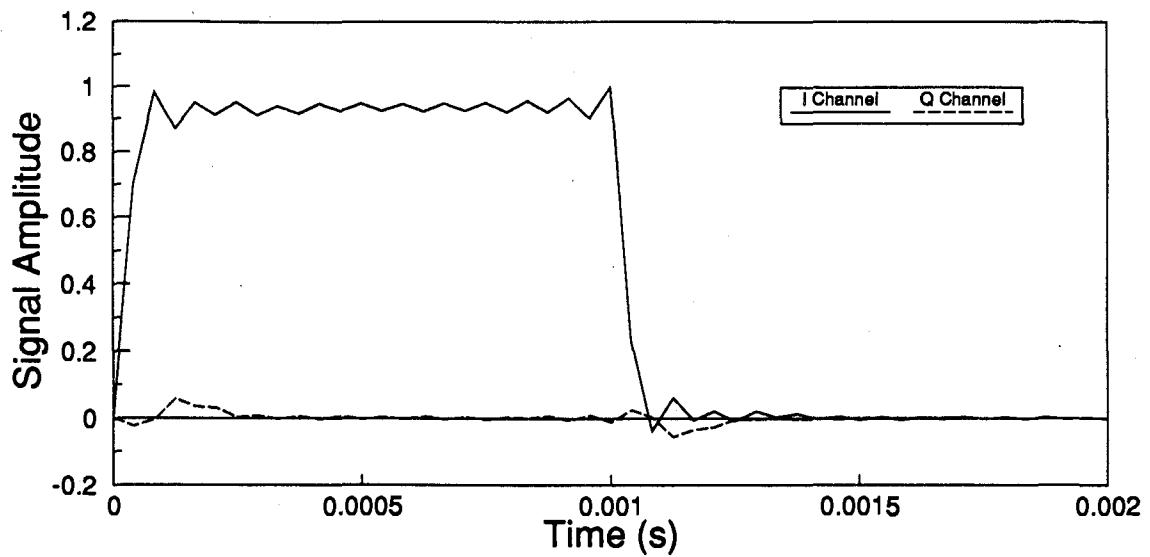
Figure 6-6 - System Baseband Response

6.2 Refraction

Another possibility was that a sound speed gradient was causing refraction of the transmitted signal. If one or more refracted signals arrived at the receiver soon after the direct arrival then they would interfere and perhaps lead to the observed response. The CTD profiles presented in section 5.2 showed that there was a significant sound velocity gradient at a depth of 2 m. A layer of water with either a positive or negative sound gradient will refract an acoustic ray, as explained below.

The effect of a sound speed gradient can easily be derived from a consideration of Snell's law. If a ray passes through a boundary with an initial propagation speed of c_1 and a final speed of c_2, then the final angle θ_2 is related to the incident angle θ_1 by the following relation.

$$\frac{\cos \theta_1}{c_1} = \frac{\cos \theta_2}{c_2} \qquad\qquad (6.5)$$

If we assume that the initial angle θ_1 is zero (a horizontal ray) then Snell's law becomes

$$\cos \theta_2 = \frac{c_2}{c_1} \qquad\qquad (6.6)$$

If this equation is valid then the value of c_2 must be less than or equal to c_1 because $\cos \theta_2$ must be less than or equal to 1. In other words, the ray will always bend towards the direction of decreasing sound speed. If we refer to the measured velocity profile in figure 5-4 or 5-5, any ray which starts below the large negative gradient, and is directed upwards, will tend to bend towards the bottom. Thus it is possible that a ray from the projector may be refracted and arrive at the hydrophone before a surface bounce.

We can determine if the magnitude of the gradient is sufficient to bend a ray back towards the bottom by using a set of equations which describe the path of the ray. A full derivation can be found in [41]. The results are summarized here, with the aid of figure 6-7.
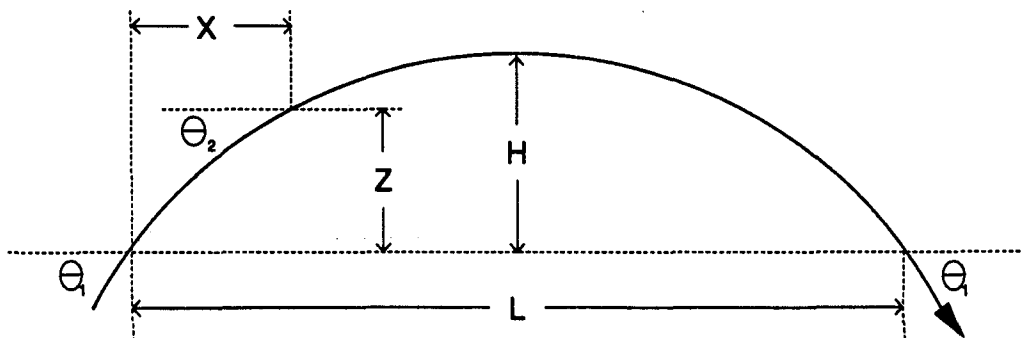

Figure 6-7 - Acoustic Ray Refraction

As shown in the figure, the ray path is a circular arc when the gradient is constant (but not zero). The following equations assume that you are starting with a ray which is at an angle θ_1 with the horizontal, and you wish to calculate the final angle θ_2 after a vertical distance Z is travelled. First we calculate the radius of curvature R

$$R = -\frac{c_1}{g \cos \theta_1}$$ (6.7)

where c_1 is the sound velocity at the initial point and g is the velocity gradient. Referring back to figure 6-7, H is the maximum vertical distance travelled before the ray starts heading towards the bottom. Thus the following equation can be used to determine if the ray would first reflect off the surface or if it would be refracted.

$$H = R(1 - \cos \theta_1)$$ (6.8)

The horizontal distance travelled when the angle reaches the same depth as the initial point is L

$$L = 2R \sin \theta_1$$ (6.9)

However, in any real water column the velocity gradient is not perfectly constant. Instead of performing one set of calculations, it is necessary to divide the water column into layers and repeat the calculation for each layer using the different values for g, the gradient. The following equations are then required

$$\theta_2 = \cos^{-1}\left(\frac{Z}{R} + \cos\theta_1\right)$$ (6.10)

$$X = R\left(\sin\theta_1 - \sin\theta_2\right)$$ (6.11)

The task of calculating the ray path is obviously best suited to a computer. A small ray tracing program was written to test the possibility of refraction causing the observed signal distortion. The program reads in data collected with the CTD profiler in order to calculate the velocity gradient profile of the water column. The user specifies a location for the transmitter and the desired horizontal scale. The program will trace a set of ray paths from the transmitter and graph the results. The user can then determine if any rays will be refracted so that they reach the receiver.

This program was used with the profiler data. Several different transmitter locations were tried. However, in all cases there was only one path that reached the receiver. Although there was a significant amount of refraction, the program showed that the gradient was not large enough to cause the observed effect.

The measured gradient was, nevertheless, large enough to pose problems for longer range communications. Figure 6-8 shows a ray trace plot generated by the program using the profiler data. The depth of the water is 12 m, while the horizontal scale has been compressed to show a range of 500 m. The plot shows the acoustic rays being refracted downward by the gradient. The effect is severe enough that some areas do not receive any direct rays from the source. These regions are known as shadow zones. In order to receive a signal in the shadow zone one must rely on reflections from the surface and bottom.
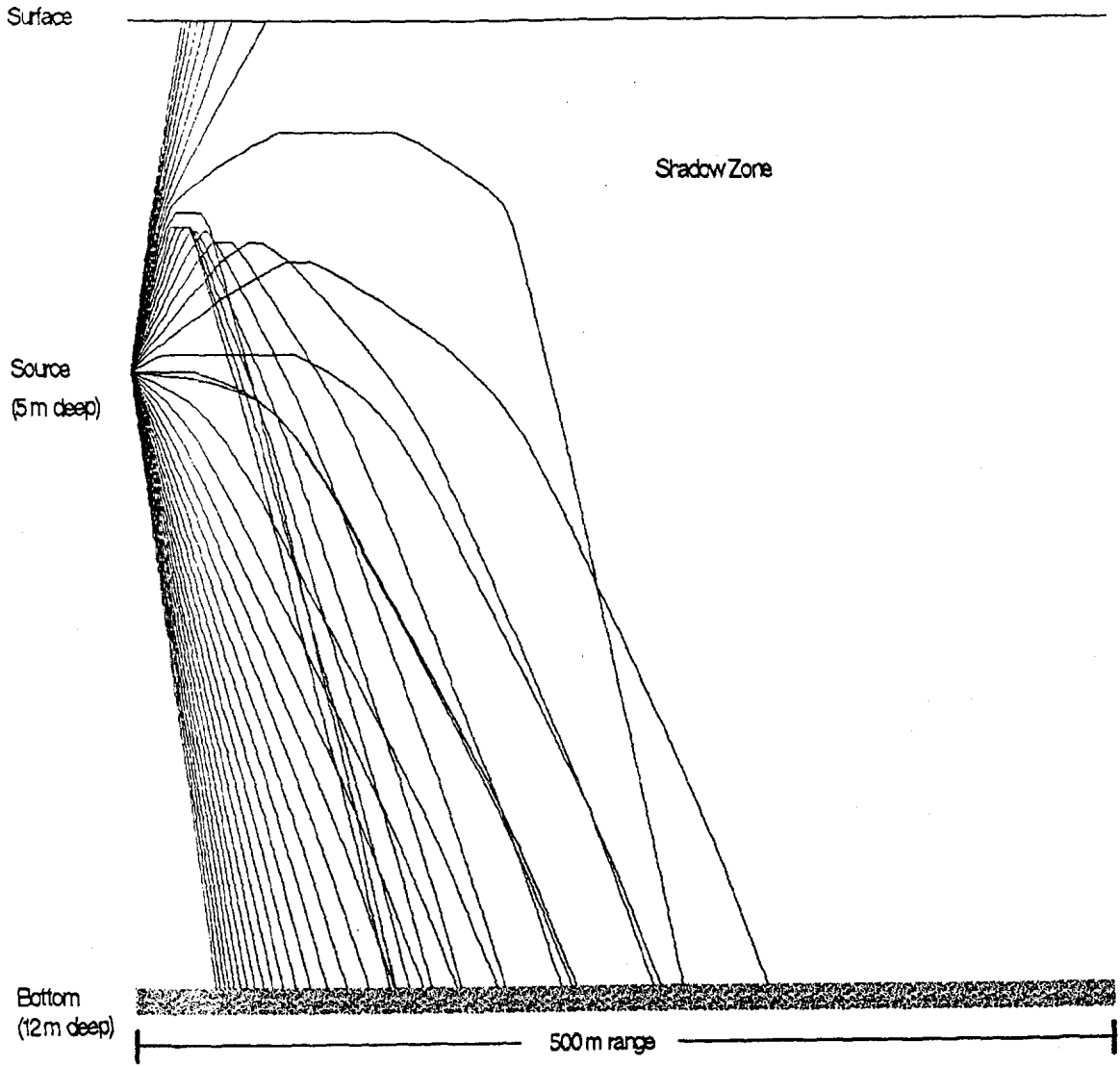
Surface

Shadow Zone

Source
(5 m deep)

Bottom
(12 m deep)

|← —————————————— 500 m range —————————————— →|

Figure 6-8 - Acoustic Ray Trace

6.3 Projector Characteristics

It was suggested by the manufacturer of the projector that some of the effects may be due to anomalies in the behaviour of the projector. It was suggested that inserting closed-cell foam into the center of the cylindrical projector might damp out unwanted vibrations. Experimenting with the foam at various depths did not produce any consistent results.

The same experiment was tried later using a denser cork insert. The effect of the cork was significant. Figure 6-9 shows a direct pulse transmitted with no cork in the projector.

Figure 6-10 shows a direct pulse received with exactly the same setup except that the projector is plugged with a cork. The time plot shows that the signal amplitude more than doubled with the addition of the cork. Furthermore, the shape of the baseband pulse is much cleaner.

We investigated the possibility of cavitation at the projector causing the observed distortion. Cavitation is the formation of bubbles at the surface of the projector when the acoustic power output is too high. Bubbles form because the intensity of the acoustic signal produces an absolute pressure less than or equal to zero atmospheres.

At the water surface the absolute pressure is 1 atmosphere; therefore an acoustic signal with a peak pressure greater than 1 atmosphere will cause cavitation. This signal level corresponds to an intensity of 0.33 W/cm^2. However, the cavitation point tends to increase with the signal frequency. At 30 kHz the cavitation point is about 1 W/cm^2 [42].

The cylindrical projector used in the experiments has a total radiating area of about 180 cm, meaning that the onset of cavitation would occur when the acoustic power exceeded roughly 180 W. The actual acoustic power radiated was determined to be 11 W, indicating that cavitation probably did not occur.
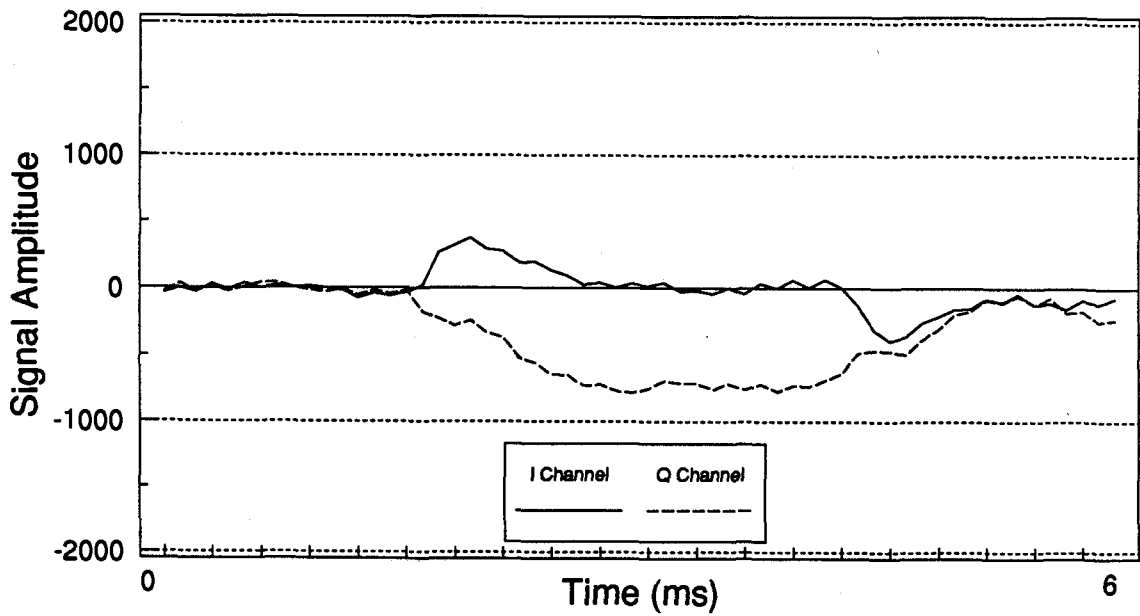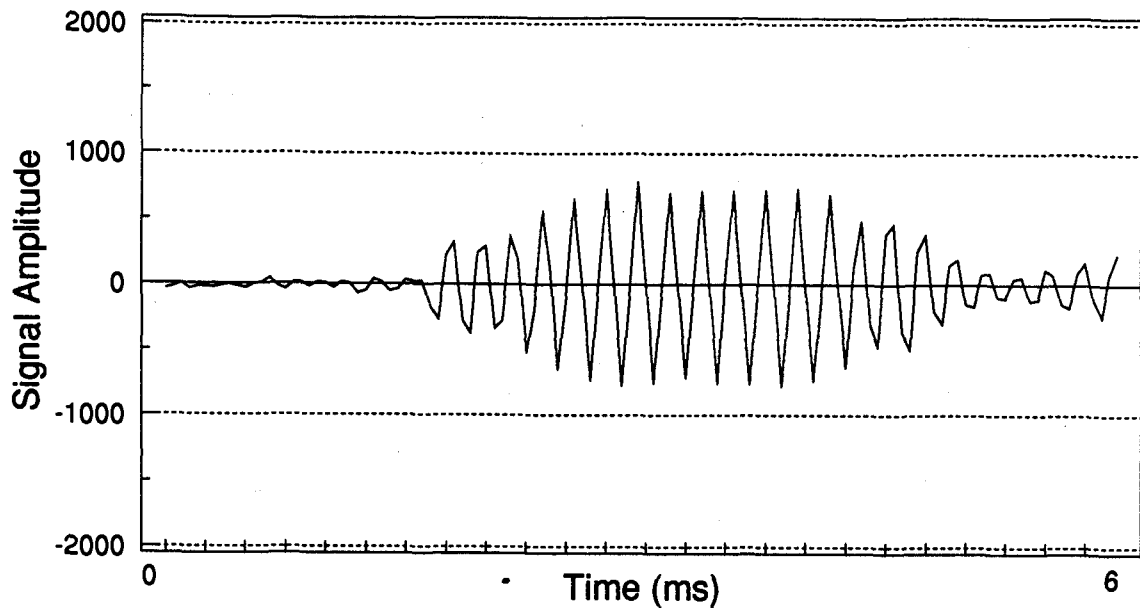
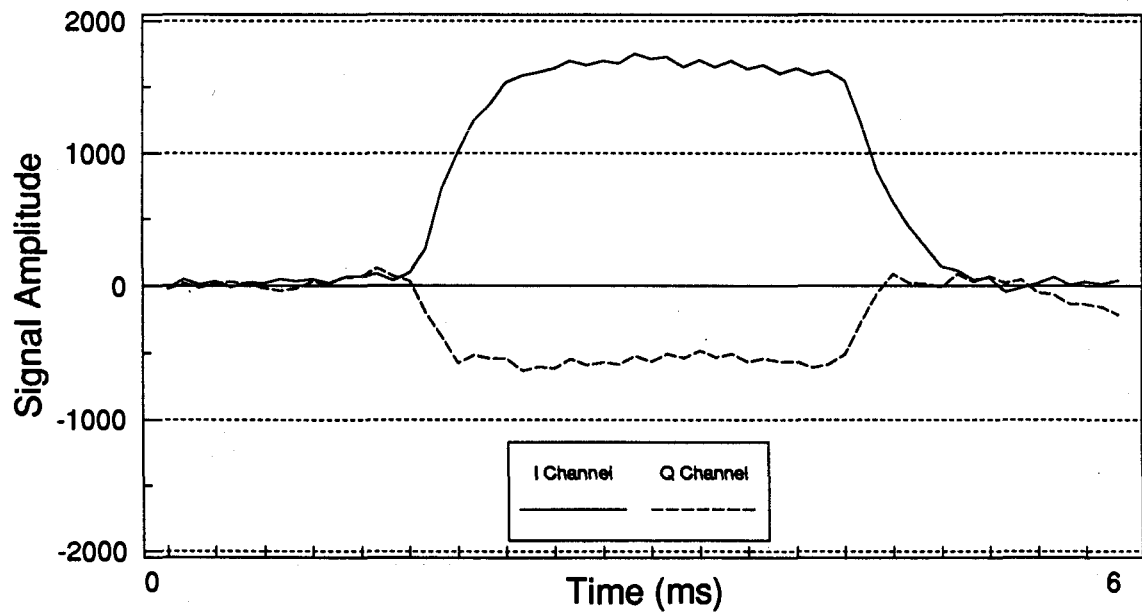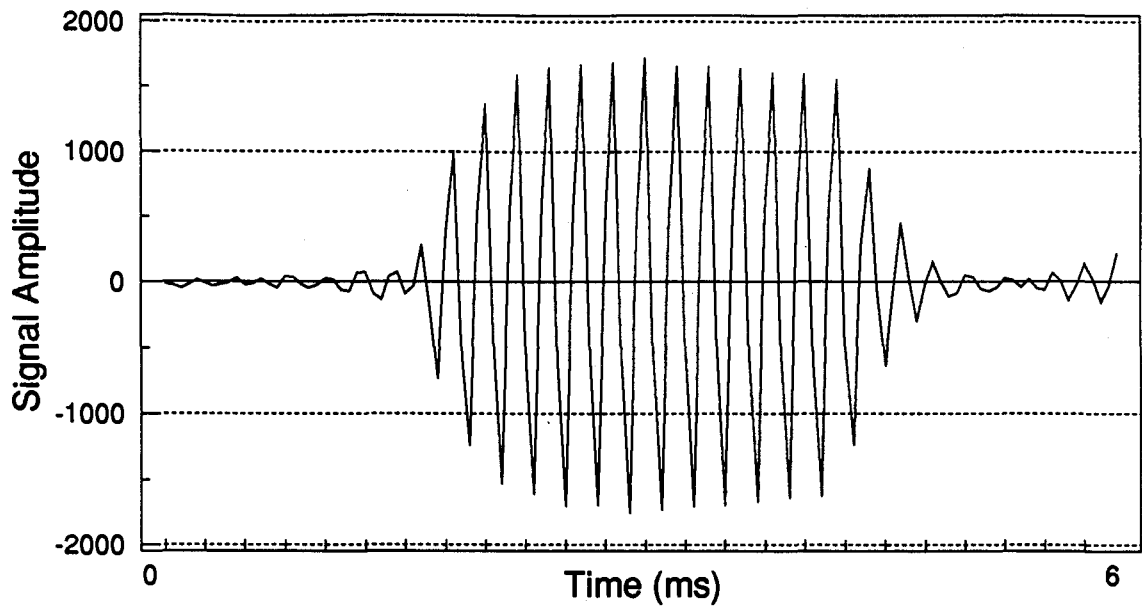Figure 6-9(a) and 6-9(b) - Received Pulse Without Cork Insert

Figure 6-10(a) and 6-10(b) - Received Pulse With Cork Insert

However, the cavitation point can be lowered by the presence of excess amounts of dissolved gases in the water. Furthermore, the acoustic power may not be radiated in a uniform pattern over the area of the projector. Thus cavitation may take place in localized areas of the projector face.

Cavitation can be avoided by either lowering the projector or decreasing the transmitted power. However, decreasing the signal power by 35 dB failed to eliminate the distortion. Furthermore, the distortion was present at all depths, from the surface down to the bottom at about 12 m; although the shape of the received signal did change with depth. At 12 m the absolute pressure is more than double the surface pressure, meaning that the cavitation point is more is four times greater than at the surface. Therefore the maximum acoustic power would be 720 W with our projector.

Another possible cause of the distortion may be related to the shape of the projector. Without the cork the projector has a hollow, water filled centre. The vibration of the piezoelectric element therefore transmits sound into the water from both the inside and outside faces of the cylinder. The geometry of the inside of the cylinder may be such that the acoustic signal from the inside produces the observed interference.

Inserting the cork would therefore eliminate the sound from inside the cylinder. However, inserting the closed-cell foam did not eliminate the distortion. URL is currently constructing a projector using a solid cylindrical piezo element. The behaviour of this projector will be characterized and compared with the hollow cylindrical projector.

The exact cause of the distortion in the projector is still undetermined. URL is currently undertaking further research on transducers in order to better understand and predict their behaviour.

6.4 Close Interference

The addition of the cork insert did not remove the distortion in all cases. It became apparent that an additional mechanism was corrupting the signal. Experimenting with various setups revealed that a backplate used for mounting the hydrophones was reflecting the signal and thereby causing interference. The backplate is a triangular shaped piece of aluminum roughly 5 mm thick. Figure 6-11 shows the returns obtained when the hydrophone was mounted on the backplate; while figure 6-12 shows the effect of removing the plate. The projector was corked in both cases to eliminate the other source of distortion. It should be noted that a DC offset at the input to the ADC causes a ripple in the baseband signal, as can be seen in the I channel of figure 6-12(b).

When the signal distortion was first observed, we originally suspected that the plate might cause interference. However, removing the plate did not eliminate the problem because the projector was still distorting the signal. It was not until we tried adding the cork and removing the backplate simultaneously that both effects became obvious.

The interfering signal reflected from the backplate may add constructively or destructively with the direct signal, depending upon their relative phase. Thus the amplitude of the received pulses can vary unexpectedly as the transducers are moved. This type of behaviour was demonstrated in figure 5-6, where the amplitude of the direct arrival decreased while the surface reflection increased when the transducers were lowered.

Clearly this source of interference is also of concern in a communications system. There are several ways one might eliminate the problem. The first could be as simple as altering the geometry of the mounting. However, if the platform is not stationary it may be difficult to predict all possible arrival angles of the signal. A better alternative might be to reduce the reflections by covering the appropriate surfaces with a sound absorbant material. Finally, the interference could also be reduced by using a directional receiver.
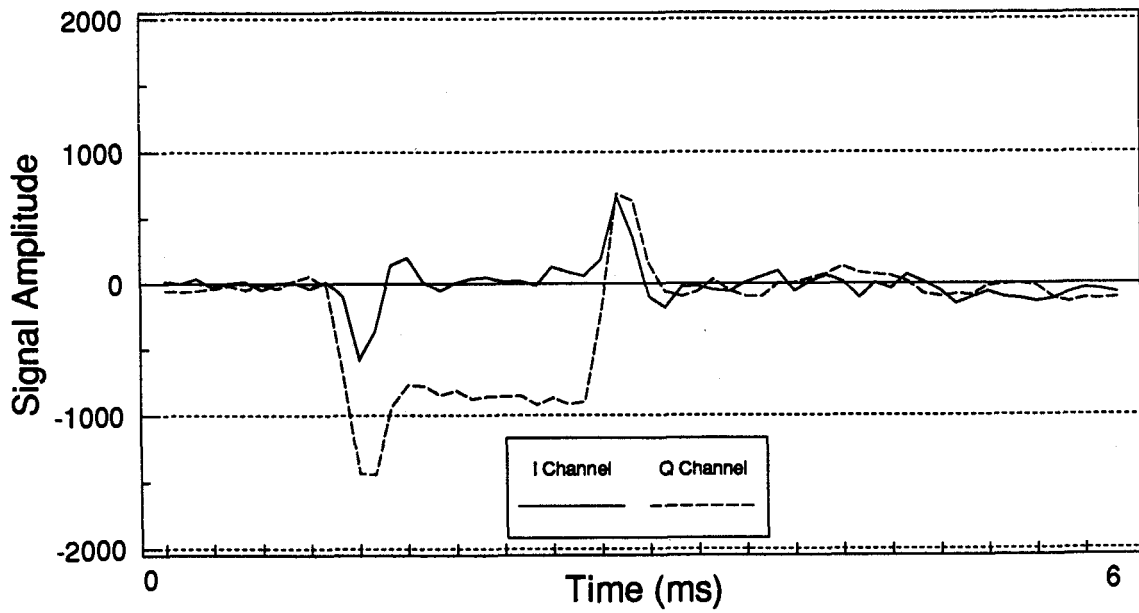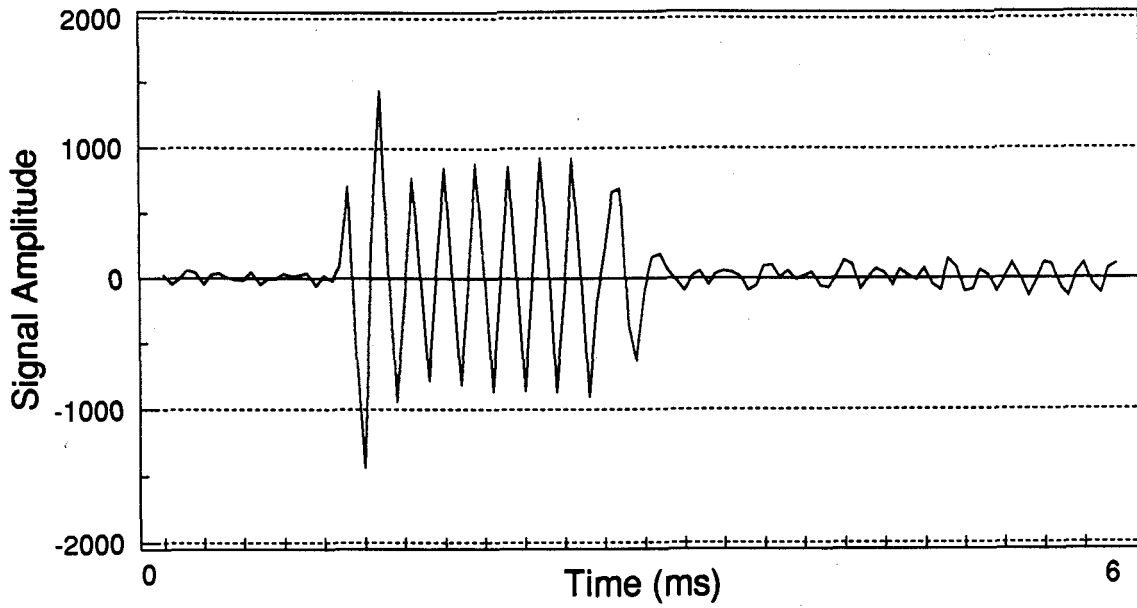
Figure 6-11(a) and 6-11(b) - Effect of Backplate Interference (with cork)
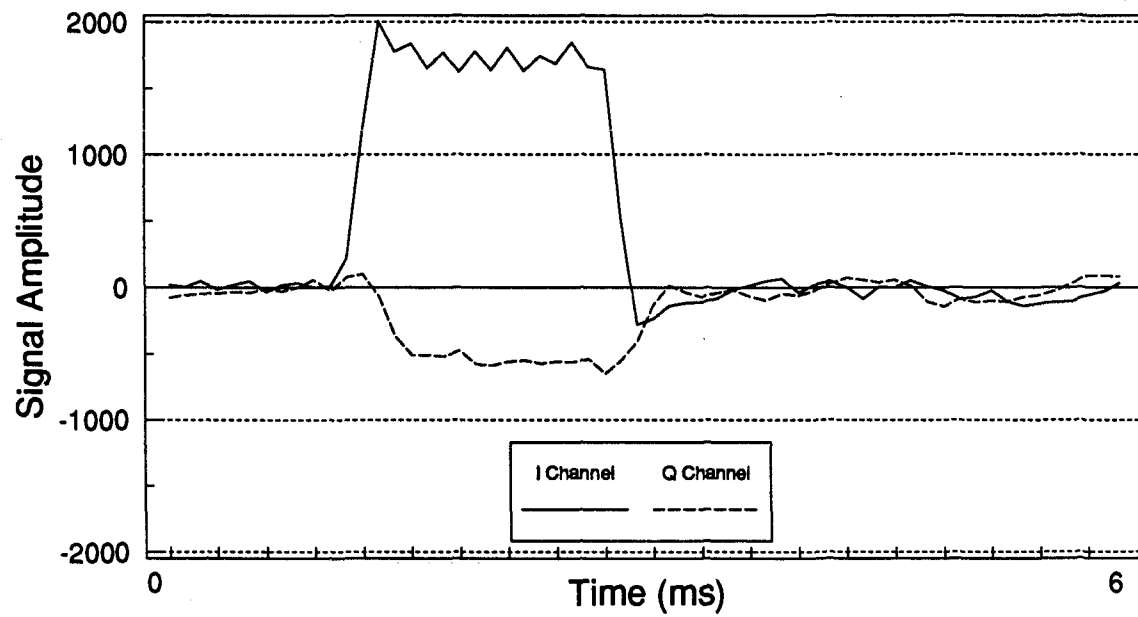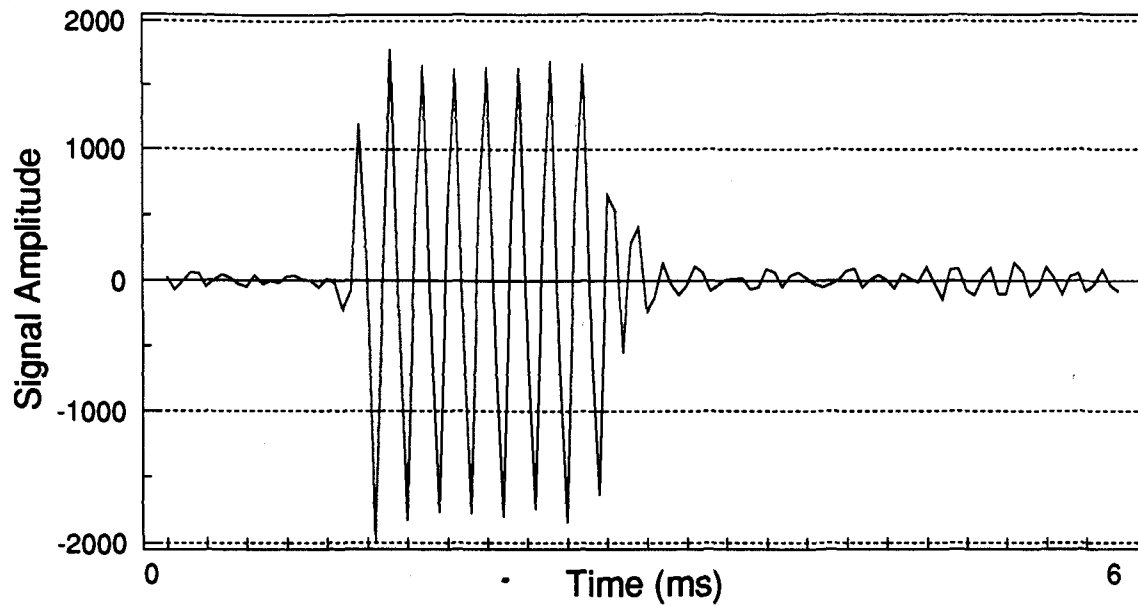
Figure 6-12(a) and 6-12(b) - Hydrophone Without Backplate (with cork)

7 Conclusions

This project was motivated by a perceived deficiency of information regarding certain fundamental aspects of the underwater acoustic communications channel. The goal was to investigate some of these basic channel characteristics and identify potential problem areas for a communications system.

The underwater channel model provides a way to study the effects of multipath interference under different conditions. One important observation concerns the variation of the level of multipath (reverberant) energy. Depending upon the geometry of the channel and the locations of the transmitter and receiver, the multipath energy can fluctuate either very slowly or very rapidly with a small change in receiver or transmitter position.

For example, when the first surface and bottom reflections arrive at the receiver at approximately the same time one can expect large variations in the resulting reverberant

energy as the two signals interfere either constructively or destructively. A change in position on the order of half a wavelength can move the receiver from a point of maximum reverberant energy to a minimum, or vice versa.

The model also showed that an array of hydrophones can reduce the level of multipath interference. However, it is important to keep the array steered towards the direct arrival to avoid placing it in a null. This implies that an array used for communications with an ROV must be steerable and be able to track the source. Even more useful would be the ability to simultaneously steer nulls in the directions of the larger multipath arrivals.

The underwater testbed provides the means to experimentally study the underwater channel. The bandpass sampling technique has proven to be valuable not only because it reduces the required sampling rate but also because it allows the direct recovery of the complex baseband signal. In turn, the complex baseband information has been shown to be important for studying the channel. The complex baseband reveals any sudden changes in phase which indicate interference or distortion in the signal.

The first sets of data showed significant levels of distortion in the received signal. The levels were far in excess of the expected transients due to filtering or other band-limiting effects. Some data seemed to indicate that there may be a frequency offset somewhere in the system which caused the baseband signal to have a nonzero frequency component. Although analysis of all the channel components showed that there was not a significant offset, this problem may be of concern in other systems. It light of this observation, it is especially important to properly characterize the frequency responses of the transducers.

Profiler measurements showed that there was a large sound speed gradient in the water column at the test site. An acoustic ray tracing program determined that the resulting refraction was not adequate to cause the observed interference. Nevertheless, the gradient was large enough to produce shadow zones at ranges of a only few hundred metres. Such gradients are not uncommon near the surface, and may pose serious problems for through-the-water acoustic communications systems.

One cause of the distortion was determined to be the hollow cylindrical projector. The insertion of a cork into the centre of the projector eliminated the source of the problem. The exact reason for the effect is still not known.

The transducer mountings were also found to be problematic. Specifically, a smooth, acoustically reflective backing produced reflections which interfered with the direct signals. Because the close reflections arrived so soon after the direct signal, the interference had the appearance of a normal transient response at the start and end of the pulse. However, when the interference was destructive the steady state portion of the pulse had an amplitude close to zero, indicating something other than a simple bandpass transient response.

There are several aspects of the project which may merit further investigation. The channel model can be used to further study the multipath behaviour. This thesis only examined the response as a function of a few of the many channel parameters. The use of a receiver arrays along with true time delay beamforming, or coherent diversity combining, also holds promise.

The study of transducer behaviour is one area which has often been neglected in the past. Indeed, the construction of acoustic transducers is half-jokingly referred to as a black art in the literature. A more thorough understanding is essential for implementing high performance acoustic systems.

Today there is a wide gap between the promise of high capacity underwater telemetry systems and the reality of current low speed technology. This thesis has laid the groundwork for future research to bridge that gap.

Appendix A - Derivation of the Projector's Transient Response

The s-domain transfer function of the modelled projector response is

$$P(s) = \frac{R}{R + sL + \frac{1}{sC}}$$

(A.1)

This is of course a standard second order system. It can be manipulated into a more recognizable form

$$P(s) = \frac{As}{s^2 + 2\zeta\omega_o s + \omega_o^2}$$

(A.2)

where

$$\omega_o = \text{center frequency} = \frac{1}{\sqrt{LC}}$$

(A.3)

$$\zeta = \text{damping factor} = \frac{R}{2}\sqrt{\frac{C}{L}}$$

(A.4)

and A is the gain of the projector at the center frequency. According to this model the gain would be 1; however, mechanical losses will results in a gain of less than 1. The Q of the system is

$$Q = \frac{1}{2\zeta} = \frac{1}{R}\sqrt{\frac{L}{C}}$$

(A.5)

The input to the system is a gated sinusoid, for which the Laplace transform is

$$\mathcal{L}\{f(t)\} = \frac{\alpha}{s^2 + \alpha^2}$$

(A.6)

where

$$f(t) = \begin{cases} 0 & t < 0 \\ \sin \alpha t & t \geq 0 \end{cases}$$

(A.7)

So the function now becomes

$$H(s) = \frac{A\alpha}{(s^2 + 2\zeta\omega_o s + \omega_o^2)(s^2 + \alpha^2)}$$

(A.8)

By definition the forcing function f(t) is zero for t < 0, hence the inverse Laplace transform will give us the desired transient response to a gated sinusoid starting at time 0. The inverse transform can be found by doing a partial fraction expansion of H(s)

$$H(s) = \frac{as + b}{s^2 + 2\zeta\omega_o s + \omega_o^2} + \frac{cs + d}{s^2 + \alpha^2}$$

(A.9)

where a, b, c and d are the coefficients to be determined. The determination of the coefficients is done by cross multiplying the previous equation and then chosing different values of s to form a set of equations. Chosing values such as 0, and the poles of H(s) simplifies the resulting set of equations by eliminating variables. The resulting coefficient values are

$$a = \frac{-A\alpha(\omega^2 - \alpha^2)}{denominator} \tag{A.10}$$

$$b = \frac{-A\alpha(2\zeta\omega^3)}{denominator} \tag{A.11}$$

$$c = \frac{A\alpha(\omega^2 - \alpha^2)}{denominator} \tag{A.12}$$

$$d = \frac{A\alpha(2\zeta\omega\alpha^2)}{denominator} \tag{A.13}$$

where the common denominator is

$$denominator = (2\zeta\omega\alpha)^2 \quad + \quad (\omega^2 - \alpha^2)^2 \tag{A.14}$$

The form of h(t), the inverse Laplace transform of H(s), will be the sum of an exponentially damped sinusoid with an undamped sinusoid. Written in terms of both sine and cosine components we have

$$h(t) = e^{-\zeta\omega_o t}\left[c_1\cos\left(\omega_o\sqrt{1-\zeta^2}\right)t \quad + \quad c_2\sin\left(\omega_o\sqrt{1-\zeta^2}\right)t\right] \quad + \tag{A.15}$$
$$c_3\cos\alpha t \quad + \quad c_4\sin\alpha t$$

where the new coefficients are given by

$$c_1 = a \tag{A.16}$$

$$c_2 = \frac{b - a(\zeta\omega_o)}{\omega_o\sqrt{1-\zeta^2}} \tag{A.17}$$

$$c_3 = c \tag{A.18}$$

$$c_4 = \frac{d}{\alpha} \tag{A.19}$$

From this expression for h(t) we want to extract the baseband In-phase and Quadrature signals, assuming that the signal is demodulated from a carrier at frequency α. First we need to make the substitution

$$\omega_o\sqrt{1-\zeta^2} \quad \rightarrow \quad \alpha + \Delta\omega \tag{A.20}$$

Now the cos and sin terms can be expanded with a trig identity and we have

$$h(t) = \cos(\alpha t) \cdot \left[c_3 + e^{-\zeta\omega_o t}(c_1\cos\Delta\omega t + c_2\sin\Delta\omega t)\right] \quad + \tag{A.21}$$

$$\sin(\alpha t) \cdot \left[c_4 + e^{-\zeta\omega_o t}(c_1\sin\Delta\omega t + c_2\cos\Delta\omega t)\right]$$

The I and Q baseband signals are then just the coefficients of $\cos\alpha t$ and $\sin\alpha t$ respectively

$$h_I(t) = c_3 + e^{-\zeta\omega_o t}(c_1\cos\Delta\omega t + c_2\sin\Delta\omega t) \tag{A.22}$$

$$h_Q(t) = c_4 + e^{-\zeta\omega_o t}(c_1\sin\Delta\omega t + c_2\cos\Delta\omega t) \tag{A.23}$$

List of References

1. Anderson, V., "Acoustic communication is better than none", *IEEE Spectrum*, vol. 7, pp. 63-68, Oct. 1970.

2. Baggeroer, A., "Acoustic Telemetry-An Overview", *IEEE J. Oceanic Eng.*, vol. OE-9, no. 4, pp. 229-235, Oct. 1984.

3. Jourdain, G., "Characterization of the Underwater Channel - Application to Communication", *Issues in Acoustic Signal/Image Processing and Recognition*", Edited by C. Chen, pp. 197-209, Berlin: Springer-Verlag.

4. Hakizimana, G., Jourdain, G., and Loubet, G., "Communication Through the Underwater Channel - The Multipath Problem and the Coding Approach", in *Proc. IEEE Pacific Rim Conf. on Comm., Comp. And Signal Proc.*, pp. 351-354, Victoria, B.C., Canada, 1987.

5. Andrews, R., And Turner, L., "On the Performance of Underwater Transmission Systems Using Amplitude-Shift-Keying Techniques", *IEEE Trans. on Sonics and Ultrasonics*, vol. SU-23, no. 1, pp. 64-71, Jan. 1976.

6. Birdsall, T., "Acoustic Telemetry for Ocean Acoustic Tomography", *IEEE J. Oceanic Eng.*, vol. OE-9, no. 4, pp. 237-241, Oct. 1984.

7. Datasonics Inc., *Datasonics Model ATM-800 Acoustic Telemetry System*, Data sheet from Datasonics Incorporated, Cataumet, MA.

8. Catipovic, J., Freitag, L., *High Data Rate Acoustic Telemetry for Moving ROVs in a Fading Multipath Shallow Water Environment*, Proceedings of the OES Symposium on Autonomous Underwater Vehicle Technology, pp. 296 - 303, June 1990.

9. Hardy, J. and Collins, J., "Factors Affecting the Design of a High-Performance Underwater Acoustic Telemetry System", in *Proc. IEEE Pacific Rim Conf. on Comm., Comp. And Signal Proc.*, pp. 346-350, Victoria, B.C., Canada, 1987.

10. Shevenell, M., "Acoustic Transmission of Images Using a Microprocessor-Based Video Bandwidth Reduction Technique", *IEEE J. Oceanic Eng.*, vol. OE-9, no. 4, pp. 259-265, Oct. 1984.

11. Urick, R. J., *Sound Propagation in the Sea*, California: Peninsula, pp. 5-1 to 5-17 1982.

12. Bergmann, P. G., and Yaspan, A., *Physics of Sound in the Sea, Part 1 - Transmission*, p. 13, London: Gordon and Breach, 1968.

13. Urick, R. J., *Sound Propagation in the Sea*, California: Peninsula, pp. 5-1 to 5-17 1982.

14. Burdic, W. S., *Underwater Acoustic System Analysis*, p. 131, New Jersey: Prentice Hall, 1984.

15. Urick, R. J., *Sound Propagation in the Sea*, California: Peninsula, pp. 10-1 to 10-18, 1982.

16. Urick, R. J., *Sound Propagation in the Sea*, California: Peninsula, 1982.

17. Bergmann, P. G., and Yaspan, A., *Physics of Sound in the Sea, Part 1 - Transmission*, London: Gordon and Breach, 1968.

18. International Submarine Technology Ltd., *IST Acoustic Telemetry System*, presented at the Offshore Technology Conference, Houston, Texas, May 1983.

19. Fiorillo, M., Irza, J. and Ekhaus, I., *Improved Underwater Communication for AUVs*, Proceedings of the OES Symposium on Autonomous Underwater Vehicle Technology, pp. 296 - 303, June 1990.

20. Catipovic, J., Freitag, L., *High Data Rate Acoustic Telemetry for Moving ROVs in a Fading Multipath Shallow Water Environment*, Proceedings of the OES Symposium on Autonomous Underwater Vehicle Technology, pp. 296 - 303, June 1990.

21. Horvat, C. M., Bird, J. S., and Goulding, M. M., "True Time Delay Bandpass Beamforming", submitted to *IEEE Trans. on Acoustics, Speech and Signal Proc.*, May 1990. Also available from The School of Engineering Science, Simon Fraser University, Burnaby, B.C.

22. Burdic, W. S., *Underwater Acoustic System Analysis*, p. 89, New Jersey: Prentice Hall, 1984.

23. Tucker, D. G., and Gazey, B. K., *Applied Underwater Acoustics*, p. 140, London: Pergamon Press, 1966.

24. Church, D. W., *Transmitter Design for Miniature Ultrasonic Telemeters*, pp. 132 - 135, Ph.D. dissertation, Technical University of Nova Scotia, Canada, 1983.

25. Albers, V. M., *Underwater Acoustics Volume 2*, pp. 310-316, New York: Plenum Press, 1967.

26. Church, D., and Pincock, D. "Predicting the Electrical Equivalent of Piezoceramic Transducers for Small Acoustic Transmitters", *IEEE Trans. on Sonics and Ultrasonics*, vol. SU-32, no. 1, pp. 61-64, Jan. 1985.

27. Albers, V. M., *Underwater Acoustics Handbook - II*, p. 342, Pennsylvania: The Pennsylvania State University Press, 1965.

28. Coates, R. F. W., *Underwater Acoustic Systems*, p. 131, Macmillan: London, 1990.

29. Burdic, W. S., *Underwater Acoustic System Analysis*, pp. 75 - 76, New Jersey: Prentice Hall, 1984.

30. Albers, V. M., *Underwater Acoustics Handbook - II*, p. 342, Pennsylvania: The Pennsylvania State University Press, 1965.

31. Burdic, W. S., *Underwater Acoustic System Analysis*, p. 77, New Jersey: Prentice Hall, 1984.

32. Horowitz, P. and Hill, W., *The Art of Electronics*, p. 286, Cambridge: Cambridge University Press, 1980.

33. Franco, S, *Design with Operational Amplifiers and Analog Integrated Circuits*, pp. 608 - 616, New York: McGraw-Hill, 1988.

34. Hayward, W. H., *Introduction to Radio Frequency Design*, pp. 202 - 210, New Jersey: Prentice-Hall, 1982.

35. Lo, E., Hardy, R. H. S., Anderson, C., And Bird, J. S., "Acoustic Testbed for Underwater Communications: System Modelling and Performance", in *Proc. IEEE Pacific Rim Conf. on Comm., Comp. And Signal Proc.*, pp. 548-552, Victoria, B.C., Canada, 1989.

36. Urick, R. J., *Ambient Noise in the Sea*, Washington, D.C.: Undersea Warfare Technology Office, Naval Systems Command, Department of the Navy, 1984.

37. Franco, S, *Design with Operational Amplifiers and Analog Integrated Circuits*, pp. 608 - 616, New York: McGraw-Hill, 1988.

38. Liu, H., Ghafoor, A., and Stockman, P. H., "A New Quadrature Sampling and Processing Approach", *IEEE Trans. on Aerospace and Elec. Systems*, vol. 25, no. 5, pp. 733-744, Sept. 1989.

39. Burdic, W. S., *Underwater Acoustic System Analysis*, p. 127, New Jersey: Prentice Hall, 1984.

40. International Submarine Technology Ltd., *IST Acoustic Telemetry System*, presented at the Offshore Technology Conference, Houston, Texas, May 1983.

41. Bergmann, P. G., and Yaspan, A., *Physics of Sound in the Sea, Part 1 - Transmission*, London: Gordon and Breach, 1968.

42. Burdic, W. S., *Underwater Acoustic System Analysis*, p. 94, New Jersey: Prentice Hall, 1984.